USE OF THE AMBIGUITY FUNCTION TECHNIQUE FOR TARGET DETECTION IN PHASE CODED CONTINUOUS WAVE RADARS

A THESIS SUBMITTED TO
THE GRADUATE SCHOOL OF NATURAL AND APPLIED SCIENCES
OF
MIDDLE EAST TECHNICAL UNIVERSITY

BY

ERKAN ÇANKAYA

IN PARTIAL FULFILLMENT OF THE REQUIREMENTS
FOR
THE DEGREE OF MASTER OF SCIENCE
IN
ELECTRICAL AND ELECTRONICS ENGINEERING

DECEMBER 2005

Approval of the Graduate School of Natural And Applied Sciences

Prof. Dr. Canan ÖZGEN
Director

I certify that this thesis satisfies all the requirements as a thesis for the degree of Master of Science.

Prof. Dr. İsmet ERKMEN
Head of Department

This is to certify that we have read this thesis and that in our opinion it is fully adequate, in scope and quality, as a thesis for the degree of Master of Science.

Prof. Dr. Gönül TURHAN SAYAN
Supervisor

Examining Committee Members

Prof. Dr. Mustafa KUZUOĞLU	(METU, EE)	
Prof. Dr. Gönül TURHAN SAYAN	(METU, EE)	
Prof. Dr. Kemal LEBLEBICIOĞLU	(METU, EE)	
Prof. Dr. Gülbin DURAL	(METU, EE)	
Caner TEZEL, M.Sc. in EE	(ASELSAN)	

I hereby declare that all information in this document has been obtained and presented in accordance with academic rules and ethical conduct. I also declare that, as required by these rules and conduct, I have fully cited and referenced all material and results that are not original to this work.

Name, Surname: Erkan ÇANKAYA

Signature **:**

ABSTRACT

USE OF THE AMBIGUITY FUNCTION TECHNIQUE
FOR
TARGET DETECTION
IN
PHASE CODED CONTINUOUS WAVE RADARS

ÇANKAYA, Erkan
M.Sc., Department of Electrical and Electronics Engineering
Supervisor: Prof. Dr. Gönül Turhan Sayan

December 2005, 138 pages

The goal of this thesis study is to investigate the Ambiguity Function Technique for target detection in phase-coded continuous wave radar. Also, phase shift keying techniques are examined in detail.

Continuous Wave (CW) Radars, which are also known as Low Probability of Intercept (LPI) radars, emit continuous signals in time which are modulated by either frequency modulation or phase modulation techniques. Modulation of the transmitted radar signal is needed to estimate both the range and the radial velocity of the detected targets. In this thesis, Phase Shift Keying (PSK) techniques such as the Barker codes, Frank codes, P1, P2, P3, P4 codes will be employed for radar signal modulation. The use of Ambiguity Function, which is a non-linear Time-

Frequency Representation (TFR), for target detection will be investigated in phase-coded CW radars for different target scenarios.

Keywords: Radar Target Detection, Phase Coded CW Radar, PSK Techniques, Ambiguity Function.

ÖZ

EVRE KODLAMALI SÜREKLİ DALGALI RADARLARDA HEDEF TESBİTİ İÇİN BELİRSİZLİK FONKSİYONU TEKNİĞİNİN KULLANILMASI.

ÇANKAYA, Erkan
Yüksek Lisans, Elektrik ve Elektronik Mühendisliği Bölümü
Tez Yöneticisi: Prof. Dr. Gönül Turhan Sayan

Eylül 2005, 138 sayfa

Bu tez çalışmasının amacı evre kodlamalı sürekli radarlarda hedef tespiti için belirsizlik fonksiyonu tekniğinin kullanımının ve evre kodlama tekniklerinin ayrıntılarıyla incelenmesidir.

Yakalanma Olasılığı Düşük radarlar olarak da bilinen Sürekli Dalgalı radarlar, sıklığı ya da evresi kiplenmiş zamanda sürekli işaretler yayarlar. Radar hedeflerinin uzaklık ve hız bilgilerinin kestirimi için yayılan radar işaretinin kiplenmesi gereklidir. Bu tezde, Barker kodu, Frank kodu, P1, P2, P3, P4 kodları gibi Evre Kodlama Teknikleri kullanılacaktır. Bu tür evre kodlamalı sürekli dalgalı radar sistemlerinde hedef tesbiti için ise, doğrusal olmayan bir zaman-frekans tekniği olan Belirsizlik Fonksiyonunun kullanımı incelenecektir.

Anahtar Kelimeler: Radarlarla Hedef Tespiti, Evre Kodlamalı Sürekli Dalgalı Radar, PSK teknikleri, Belirsizlik Fonksiyonu.

To My Family

ACKNOWLEDGMENTS

I am in great debt to Prof. Dr. Gönül Turhan Sayan, my research advisor, who labored hard for two years to ensure I would accomplish my research goals.

I would like to thank my parents for their patience and trust throughout my thesis.

I wish to thank to my dear friend and colleague Caner Tezel for his valuable criticism and support.

TABLE OF CONTENTS

LIST OF TABLES

LIST OF FIGURES

CHAPTER I

INTRODUCTION

The word radar is an abbreviation for RAdio Detection And Ranging. In general, radar systems use modulated waveforms and directive antennas to transmit electromagnetic energy into a specific volume in space to search for targets. It consists fundamentally of a transmitter, a receiver, an antenna, and an electronics system to process and record the data. Objects (targets) within a search volume will reflect portions of this energy (radar returns or echoes) back to radar. These echoes are then processed by the radar receiver to extract target information such as range, velocity, angular position, and other target identifying characteristics [1, 2].

The time delay between the transmitted and reflected signals determines the distance (or range) to the target. The speed of a target to be measured using the Doppler effect in radar applications. When a signal from a radar is scattered by a target, its frequency is changed in proportion to the speed of the target. By measuring this change in frequency, a Doppler radar is able to infer the target's radial speed.

Radars can be classified as ground based, airborne, space borne, or ship based radar systems. They can also be classified into numerous categories based on the specific radar characteristics, such as the frequency band, antenna type, and waveforms utilized. Another classification is concerned with the mission and the functionally of the radar. This includes: weather, acquisition and search, tracking, track-while-scan, fire control, early warning, over the horizon, terrain following, and terrain avoidance radars [3].

Radars are most often classified by types of waveforms they use, or by their operating frequency. Considering the waveforms first, radars can be Continuous Wave (CW) or Pulsed Radars (PR).

Most widely used radar type is pulsed radar. Pulsed radars emit a series of quick signals instead of one continuous wave. Short (microsecond) high energy pulses are emitted, waited on for echo and the returning echoes are recorded.

CW radars continuously emit electromagnetic energy. It must therefore receive the returned signal while it is transmitting. It is also necessary to employ two well-isolated antennas, one for transmitting and one for receiving, to help further separate the signal transmitted from the signal reflected. Target radial velocity can be measured by using unmodulated CW radars. On the other hand, target range information can not be extracted without utilizing some form of modulation. Use of unmodulated CW radars is in target velocity search and track, and in missile guidance.

The average power determines the detection characteristics of the radar. The CW radar has a low continuous power compared to the high peak power of the pulse radar but both can give the same detection performance. For high average power, a short pulse (high range resolution) transmitter must have a high peak power [4].

Because of low peak power transmission characteristic CW radars are more difficult to intercept by an unprepared receiver. For this reason, CW waveforms are sometimes referred to as Low Probability of Intercept (LPI) waveforms. The term LPI is that property of a radar that, because of its low power, wide bandwidth, frequency variability, or other design attributes, makes it difficult for it to be detected by means of a passive intercept receiver.

LPI modulation techniques include frequency modulation such as FMCW and frequency shift keying. Also used are phase modulation such as the polyphase codes Frank, P1, P2, P3, P4, and polytime codes T1, T2, T3, and T4, there are several trade-offs in the design of LPI emitters. The major question is how to get a 100 percent duty factor and still get the desired range and velocity performance needed to perform the mission.

In this thesis, the phase modulated radars that include polyphase modulation (Polyphase Shift Keying, PSK) have been mainly investigated. Details are given in Chapter 3.

The ambiguity function is a major tool for studying and analyzing radar signals. The ambiguity function $|\chi(\tau,\nu)|$ describes that two-dimensional (delay τ and Doppler ν) response [5].

The radar's auto ambiguity function represents the output of the matched filter, and the cross auto ambiguity function describes the interference caused by range and Doppler of a target when compared to radar. Ambiguity analysis is important to understand the properties of the CW waveform and its effect on measurement accuracy, target resolution, ambiguities in range, and radial velocity, and its response to clutter. The ambiguity function and its details are given in Chapter 2 which presents important properties of the ambiguity function.

In FMCW radars, the received signal and the transmitted signal are multiplied by a mixer. The mixer output is passed through a low-pass filter to remove signal components centered about twice the carrier frequency. FFT processing is applied to output of low-pass filter then beat frequencies are obtained. Finally, range and velocity profile of a target can be computed from beat frequencies. Mixer-low pass filter implementation and Fast Fourier Transform processing is a conventional method for target detection in FMCW radars. Details of this conventional method are explained in literature.

On the other hand, there is no conventional method for target detection in phase-coded radars in literature. In this thesis, use of Ambiguity Function technique for target detection in phase-coded radars is discussed as an original problem, and the Ambiguity Function has been used as major tool for investigating different phase coding techniques. It is also used to determine the range and the Doppler information of the specific targets. Details of this technique are given in Chapter 4.

CHAPTER II

RADAR AMBIGUITY FUNCTION ANALYSIS

2.1 Introduction

Radar ambiguity function, first introduced by Woodward in 1953 [6], is a basic mathematical tool for signal design and analysis. It can be used for characterizing radar performance in target resolution and clutter rejection. The periodic autocorrelation function (PACF) is introduced, and it is shown that CW signals can have a perfect PACF with zero side lobes. The periodic ambiguity function (PAF) is also introduced, to analyze the response of a matched filter that uses N copies of the reference (transmitted) function to cross correlate the return CW signal and perform target detection.

Basically, the radar ambiguity function represents the output of the matched filter, and it describes the interference caused by range or Doppler of a target when compared to a reference target equal Radar Cross Section (RCS). The ambiguity function evaluated at $(\tau,\nu)=(0,0)$ is equal to the matched filter output that is matched perfectly to the signal reflected from the target of interest. In other words, returns from the nominal target are located at the origin of the ambiguity function. Thus, the ambiguity function at nonzero τ and ν represents returns from some range and Doppler different from those for the nominal target.

The ambiguity function is normally used by radar designers as a means of studying different waveforms. It can provide insight about how different waveforms may be suitable for the various radar applications. It is also used to determine the range and

Doppler resolutions for a specific radar waveform. The three-dimensional plot of the ambiguity function versus frequency and time delay is called the radar ambiguity diagram. The auto ambiguity function is defined as

$$\left|\chi(\tau,\nu)\right| = \left|\int_{-\infty}^{\infty} u(t)u^{*}(t+\tau)\exp(j2\pi\nu t)\,dt\right| \tag{2.1}$$

where u is the complex envelope of the signal. A positive ν implies a target moving toward to radar. Positive τ implies a target farther from the radar than the reference position.

Consequently, ambiguity analysis is important to understand the properties of the CW waveform and its effect on measurement accuracy, target resolution ambiguities in range, and radial velocity, and its response to clutter. In this thesis, the periodic autocorrelation function (PACF) is introduced, and it is shown that CW signals can have a perfect PACF with zero side lobes. The periodic ambiguity function is also introduced, to analyze the response of a matched receiver that uses N copies of the reference (transmitted) function to cross correlate the return CW signal and perform target detection. The PAF is similar to the ambiguity function often used to represent the magnitude of the matched receiver output for a coherent pulse train. The cut of the PAF at zero Doppler ($\nu = 0$) is the PACF, and cuts of the PAF along zero delay ($\tau = 0$) yield the response of the correlation receiver at a given Doppler shift.

In ambiguity analysis, the receiver is considered matched to a target signal at a given delay and transmitted frequency. The maximum of the ambiguity function occurs at origin$(\tau = 0, \nu = 0)$, and $\left|\chi(0,0)\right|$ is the output if the target appears at the delay and Doppler shift for which the filter was matched. The delay-Doppler response of the matched filter output is important for understanding the properties of the radar waveform. Ideally, the ambiguity diagram would consist of a diagonal ridge centered at the origin, and zero elsewhere. However, it is impossible to obtain.

A narrowband signal can be written in the following form:

$$s(t) = g(t)\cos(w_c t + \phi(t)) \tag{2.2}$$

Or, in terms of in-phase (I) and quadrature (Q) components

$$s(t) = g_I(t)\cos(w_c t) - g_Q(t)\sin(w_c t) \tag{2.3}$$

where

$g(t)$ is the natural envelope of $s(t)$ and $\phi(t)$ is the instantaneous phase, $g_I(t)$ and $g_Q(t)$ are the in-phase and quadrature components, respectively, given by

$$g_I(t) = g(t)\cos(\phi(t)) \tag{2.4}$$

$$g_Q(t) = g(t)\sin(\phi(t)) \tag{2.5}$$

Define the complex envelope of the signal as

$$u(t) = g_I(t) + jg_Q(t) \tag{2.6}$$

Thus the narrowband signal can be expressed as a complex signal (also called analytic signal)

$$s(t) = \mathrm{Re}\left\{u(t)\exp(jw_c t)\right\} \tag{2.7}$$

It is sufficient to deal with the complex envelope of a signal (to within a phase shift and constant factor).

2.2 Main Properties of the Ambiguity Function

The main properties of the ambiguity function are listed below. Note that, the first two properties assume that the energy E of $u(t)$ is normalized to unity [7, 8].

1) The maximum value for the ambiguity function occurs at $(\tau,\nu) = (0,0)$ and is equal to 1 (where it is normalized to unity by normalizing the signal energy).

$$\left|\chi(\tau,\nu)\right| \le \left|\chi(0,0)\right| = 1 \tag{2.8}$$

2) The ambiguity function is symmetric with respect to origin,

$$\left|\chi(-\tau,-\nu)\right| = \left|\chi(\tau,\nu)\right| \tag{2.9}$$

This property suggests that it is sufficient to study and plot only two adjacent quadrants of the AF. The remaining two can be deduced from the symmetry property.

3) The total volume under the ambiguity function is constant, if we assume that the energy of $u(t)$ is normalized to unity, volume is 1.

$$\int_{-\infty}^{\infty}\int_{-\infty}^{\infty} \left|\chi(\tau,\nu)\right|^2 d\tau d\nu = 1 \tag{2.10}$$

Properties 1 and 3 imply that if we attempt to squeeze the ambiguity function to a narrow peak at the origin, the peak cannot exceed a value of 1, and the volume squeezed out of that peak must reappear somewhere else.

4) If a given complex envelope $u(t)$ has an ambiguity function $\left|\chi(\tau,\nu)\right|$ that is,

$$u(t) \Leftrightarrow \left|\chi(\tau,\nu)\right| \tag{2.11}$$

then adding linear frequency modulation (LFM), which is equivalent to a quadratic-phase modulation, implies that

$$u(t)\exp(j\pi kt^2) \Leftrightarrow \left|\chi(\tau,\nu-k\tau)\right| \tag{2.12}$$

2.3 Cuts of the Ambiguity Function along Delay and Doppler Axes

If we set the Doppler shift to zero ($\nu = 0$) i.e. cut along the delay axis, the ambiguity function becomes the autocorrelation function of the complex envelope $u(t)$

$$\left|\chi(\tau,0)\right| = \left|\int_{-\infty}^{\infty} u(t)u^{*}(t+\tau)dt\right| = \left|R(\tau)\right| \tag{2.13}$$

where $R(\tau)$ is the autocorrelation function (ACF) of $u(t)$. We got that the zero-Doppler cut of the AF, known as the range window for a matched-filter receiver, is the ACF. On the other hand, the ACF equals the inverse Fourier transform of the power spectral density.

The second interesting cut is along the Doppler frequency axis. Setting $\tau = 0$, the ambiguity function becomes the Fourier transform of the magnitude squared of the complex envelope $u(t)$. In other words, this cut is indifferent to any phase or frequency modulation in $u(t)$; it is a function of the amplitude.

$$\left|\chi(\tau,v)\right| = \left|\int_{-\infty}^{\infty} \left|u(t)\right|^{2} \exp(j2\pi\nu t)\,dt\right| \tag{2.14}$$

The volume distribution of the ambiguity function (squared) in range and in Doppler is constrained by two more refined relationships [5]:

$$\int_{-\infty}^{\infty} \left|\chi(\tau,v)\right|^{2} d\tau = \int_{-\infty}^{\infty} \left|\chi(\tau,0)\right|^{2} \exp(j2\pi\nu t)\,d\tau \tag{2.15}$$

$$\int_{-\infty}^{\infty} \left|\chi(\tau,\nu)\right|^{2} d\nu = \int_{-\infty}^{\infty} \left|\chi(0,\nu)\right|^{2} \exp(j2\pi\nu\tau)d\nu \tag{2.16}$$

Two properties at above demonstrate that if the main peak is squeezed along the delay axis, the volume must spread out in the Doppler domain, and when it is squeezed along the Doppler axis, the volume must spread in delay. Thus, close

target separability in one parameter is gained at the expense of spreading volume over a large interval of the other parameter.

2.4 Periodic Autocorrelation Function

CW waveforms can be called as LPI signals due to their low power characteristics. They are modulated by a periodic function, such as a phase code sequence or linear frequency ramp. CW waveforms can yield a perfect PACF when they are periodically modulated, this is their major advantage. As an example, if we consider a phase-coded CW signal with N_C phase codes each with subcode duration t_b second. The transmitted CW signal has a code period $T = N_c t_b$ s and a periodic complex envelope $u(t)$ given as

$$u(t) = u(t + nT) \tag{2.17}$$

for $n = 0, \pm 1, \pm 2, \pm 3, \pm 4.....$ The values of the PACF as a function of the delay τ (which are multiples of t_b) are given by

$$R(r \cdot t_b) = \frac{1}{N_c} \sum_{n=1}^{N_c} u(n) u^*(n + \tau) \tag{2.18}$$

and ideally we would like a perfect PACF or

$$R(t_b) = \begin{cases} 1, & r = 0 (\text{mod}\, N_c) \\ 0, & r \neq 0 (\text{mod}\, N_c) \end{cases} \tag{2.19}$$

The perfect PACF is obtained only for continuous signal. Finite duration signals, such as a pulse train, cannot achieve this ideal auto correlation since as the first sample (or last sample) enters (or leaves) the correlator, there is no sample that can cancel the product to yield a zero output.

2.5 Periodic Ambiguity Function

The periodic ambiguity function (PAF) describes the response of a correlation receiver to a CW signal modulated by a periodic waveform with period T, when the reference signal is constructed from an integral number N of periods of the transmitted signal. Thus, the reference signal is of duration NT. The response is a function of both delay and Doppler shift. The PAF is a two-dimensional generalization of the periodic autocorrelation function, by including the effect of Doppler shift. A major difference between the periodic autocorrelation and periodic ambiguity function is the significance of the number of periods N. In the autocorrelation case, the response of N periods differs from the response of a single period, only by the factor N. When Doppler is present, and has to be resolved, the ability to resolve it is a function of the duration of the reference signal, and the effect of N on the response is more significant and complicated. However, the effect of N is independent of the modulation waveform and of the delay [9].

When the reference signal is of duration NT, the response of the correlation receiver is the PAF for N periods, which, after normalization, is defined by

$$\left|\chi_{NT}(\tau,\nu)\right| = \left|\frac{1}{NT}\int_{0}^{NT} u(t)u^{*}(t+\tau)\exp(j2\pi\nu t)\,dt\right| \quad (2.20)$$

where τ is assumed to be a constant, and the delay rate of change is represented by the Doppler shift ν. The PAF for N periods is related to the single – period ambiguity function by a universal relationship

$$\left|\chi_{NT}(\tau,\nu)\right| = \left|\chi_{T}(\tau,\nu)\right|\left|\frac{\sin(N\pi\nu T)}{N\sin(\pi\nu T)}\right| \quad (2.21)$$

where

$$\left|\chi_{T}(\tau,\upsilon)\right| = \frac{1}{T}\left|\int_{0}^{T} u(t)u^{*}(t+\tau)\exp(j2\pi\nu t)dt\right| \quad (2.22)$$

is the single period ambiguity function. The single period ambiguity function is multiplied by a universal function of N and T that is independent of the complex envelope of the signal and does not change with τ. The PAF shows the effect of using a reference receiver consisting of N code periods. From eqn. (2.21) it can be easily seen that for large number of code periods N, the PAF is increasingly attenuated for all values of ν except at multiplies of $1/T$. It also has main lobes at $\nu T = 0, \pm 1, \pm 2, \ldots.$ Equation (2.21) also reveals that the PAF has relatively strong Doppler side lobes.

Equation (2.21) suggests that it is sufficient to calculate the single-period PAF (2.22) and then multiply it by the function $\left|(\sin N\pi\nu T)/(N \sin \pi\nu T)\right|$ to get the N-period PAF. The multiplying function is a function of the Doppler shift only. For $N = 8$ universal function is plotted in Fig. 2.1.

Figure 2.1 demonstrates the main reason for using a coherent train of N pulses with a repetition interval T. Note that the Doppler resolution improves dramatically and becomes $1/NT$: namely, the inverse of the coherently processed time duration, and it is practically independent of the original pulse waveform. The penalty is recurrent lobes at Doppler intervals of $1/T$: namely, the inverse of the pulse repetition time. Because the function plotted in Fig. 2.1 multiplies an ambiguity function, which is two-dimensional, it may help to point out that what multiplies the ambiguity function is an extension of Fig. 2.1 to all delays, as demonstrated in Fig. 2.2.

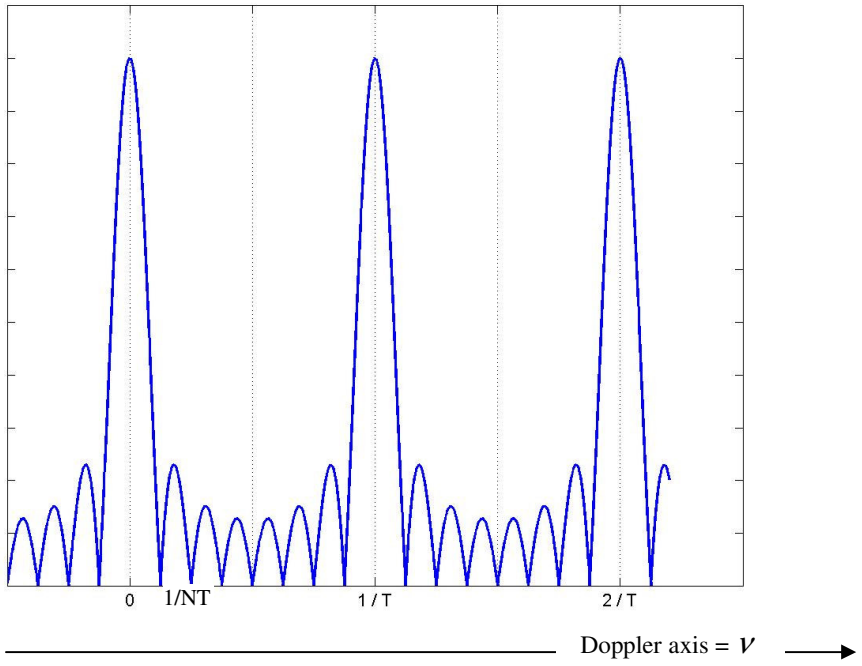

Figure 2.1: Function $\left|(\sin N\pi\nu T)/(N\sin\pi\nu T)\right|$ ($N=8$)

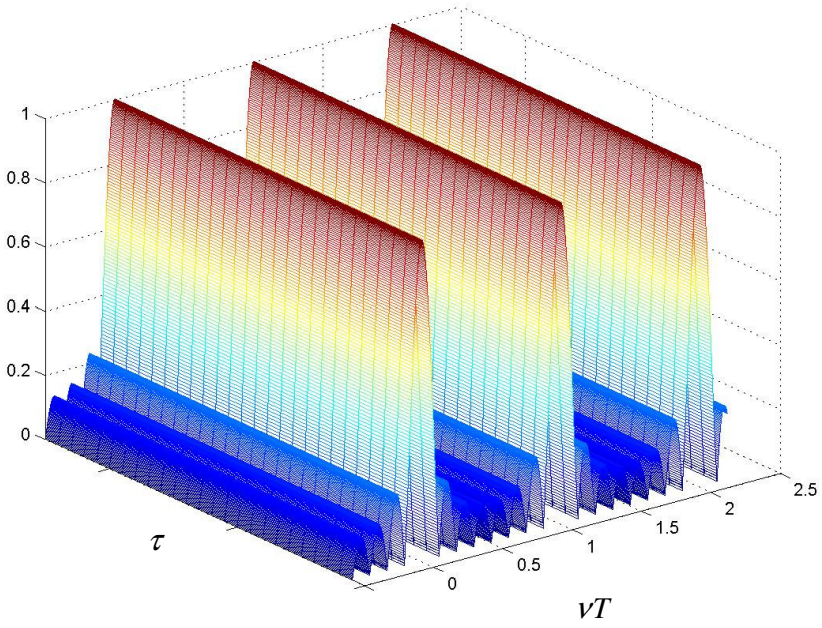

Figure 2.2: Extension of $\left|(\sin N\pi\nu T)/(N\sin\pi\nu T)\right|$ to all delays ($N=8$)

Note that for a large N, the PAF is compressed to zero all ν, except near $\nu = n/T$, $n = 0, \pm 1, \pm 2, \ldots$. For infinitely large N, the PAF of a sequence exhibiting perfect periodic autocorrelation will strongly resemble the ambiguity function of a coherent pulse train.

Now that we have the tool to analyze periodic signals, we apply it to a special family of CW signals, which yield perfect periodic autocorrelation, and find if and how this perfect response deteriorates due to Doppler shift.

Periodic Ambiguity Function of the 16-element Frank phase-coded CW signal with $N = 1$ period is given in Figure 2.1, and also Periodic Ambiguity Function of the 16-element Frank phase coded CW signal with $N = 16$ periods is given in Figure 2.2. The main difference between Figs. 2.3 and 2.4 is the improved Doppler resolution when $N = 16$.

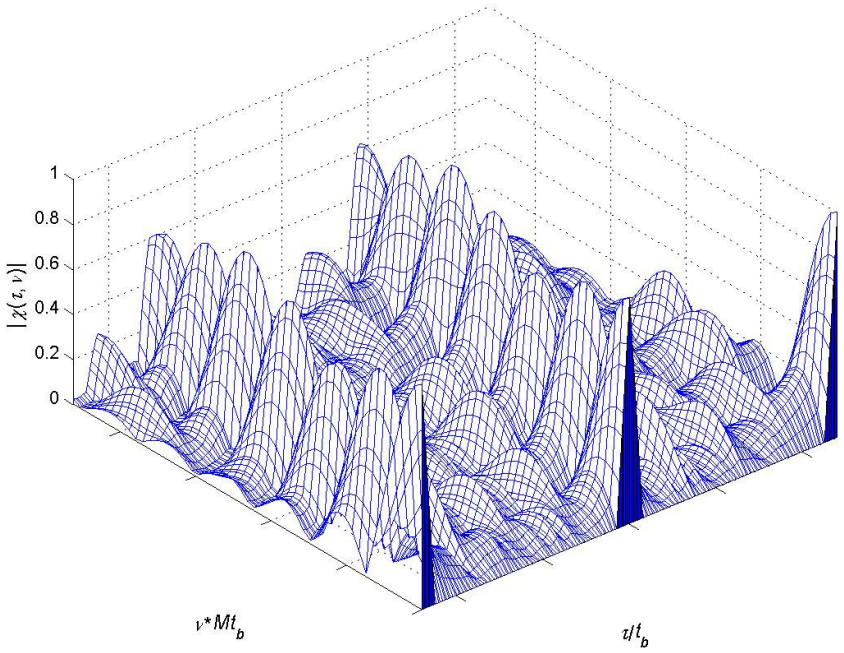

Figure 2.3: PAF of the 16-element Frank phase-coded CW signal with $N = 1$ period.

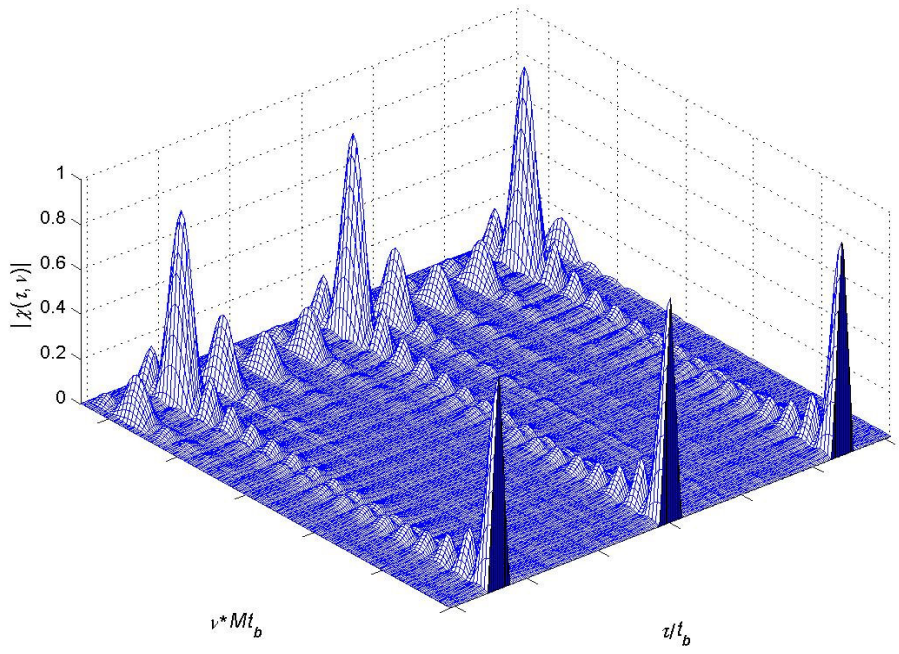

Figure 2.4: PAF of the 16-element Frank phase-coded CW signal with $N = 16$ periods.

2.5.1 Periodicity of the PAF

The cut along the delay axis is the periodic autocorrelation of the signal $u(t)$:

$$\begin{aligned} \left|\chi_{NT}(\tau,0)\right| &= \frac{1}{NT}\left|\int_0^{NT} u(t)\; u^*(t+\tau)\,dt\right| \\ &= \frac{1}{T}\left|\int_0^{T} u(t)\; u^*(t+\tau)dt\right| \end{aligned} \tag{2.23}$$

The cut along the Doppler axis (zero delay) is

$$\chi_{NT}(0,\nu) = \frac{1}{NT}\int_0^{NT} |u(t)|^2\, e^{j2\pi\nu t}\,dt \tag{2.24}$$

For phase-modulated CW signals

$$\left|\chi_{NT}(0,\nu)\right| = \left|\frac{\sin(\pi\nu NT)}{\pi\nu NT}\right| \tag{2.25}$$

for $\nu = 0$

$$\left|\chi_{NT}(0,0)\right| = 1 \tag{2.26}$$

For any integer n, the periodicity on the delay axis is

$$\left|\chi_{NT}(nT,\nu)\right| = \left|\chi_{NT}(0,\nu)\right| \tag{2.27}$$

For the ν axis, for $m = 0, \pm 1, \pm 2, \ldots$

$$\left|\chi_{NT}\left(\tau, m/T\right)\right| = \left|\chi_{NT}(\tau + nT, m/T)\right| \tag{2.28}$$

The symmetry cuts are a function of the three parameters: the code period T, the number of phase codes N_c, and the number of code periods used in the correlation receiver N.

2.5.2 Peak and Integrated Side Lobe Levels

The time side lobe levels in the autocorrelation function (ACF) help quantify the LPI waveform in its ability to detect targets without interfering side lobe targets. That is, if the ACF has high side lobes, a second nearby target might be able to hide in a side lobe and go undetected. To quantify the LPI waveform characteristics, the peak side lobe level (PSL) of the ACF can be defined as

$$PSL = 10\log_{10}\left[\frac{\text{Max side lobe power}}{(\text{Peak response})^2}\right] = 10\log_{10}\left[\frac{\max R^2(k)}{R^2(0)}\right] \tag{2.29}$$

where k is the index for the points in the ACF, $R(k)$ is ACF for all of the output range side lobes except that at $k = 0$, and $R(0)$ is the peak of the ACF at $k = 0$.

The integrated side lobe level is

$$ISL = 10\log_{10}\left[\frac{\text{Total power in side lobes}}{(\text{Peak response})^2}\right] = 10\log\sum_{k=-M}^{M}\frac{R^2(k)}{R^2(0)} \tag{2.30}$$

and is a measure of the total power in the side lobes as compared with the compressed peak. The PSL is a useful measure when a single point target response is of concern. Values for the PSL depend on the number of subcodes in the code sequences N_c as well as the number of code periods N within the receiver. The ISL is considered a more useful measure than the PSL when distributed targets are often concern.

2.6 Doppler Sidelobe Reduction Using Weight Windows

In a finite-length signal the weight window could have been split between the transmitter and receiver. In a continuous periodic signal only the finite reference signal can be modified by a weight function $w(t)$. That converts the receiver from a matched receiver to a mismatched receiver (with a corresponding degradation in SNR and decrease in Doppler resolution) [10]. The analysis of the effect of a weight window on the delay – Doppler response was introduced at 1995 by Getz and Levanon. The reference signal $u^*(t)$ is divided into a product of three functions: $r(t)$ [periodic with the same period as $u(t)$], $w(t)$ (an aperiodic weight function), and $p(t)$ (a rectangular window of duration NT),

$$p(t) = \begin{cases} 1, & 0 \le t \le NT \\ 0, & \text{elsewhere} \end{cases} \tag{2.31}$$

The delay-Doppler response of the mismatched receiver becomes

$$\left|\psi(\tau,\nu)\right| = \left|\int_{-\infty}^{\infty} u(t-\tau)r(t)p(t)w(t)\exp(j2\pi\nu t)dt\right| \tag{2.32}$$

Since (2.32) is the Fourier transform of two products (except for the missing negative sign in the exponential), it can be described by the convolution (denoted $\otimes$) of two Fourier transforms,

$$\left|\Psi(\tau,\nu)\right| = \left|\int_{-\infty}^{\infty} u(t-\tau)r(t)\exp(j2\pi\nu t)dt\right| \otimes \left|\int_{-\infty}^{\infty} p(t)w(t)\exp(j2\pi\nu t)dt\right| \tag{2.33}$$

With the first transform, since both $u(t)$ and $r(t)$ are infinitely long and periodic with period T, the Fourier transform of their product (for any τ) can be shown to be a series of delta functions at $\nu = 0, \pm 1, \pm 2, \ldots$:

$$\int_{-\infty}^{\infty} u(t-\tau)r(t)\exp(j2\pi\nu t)dt = \sum_{-\infty}^{\infty} \delta\left(\nu - \frac{n}{T}\right) g_n(\tau) \tag{2.34}$$

where

$$g_n(\tau) = \frac{1}{T}\int_0^T u(t-\tau)r(t)\exp(j2\pi n\frac{t}{T})dt \tag{2.35}$$

The second integral in (2.33) is the Fourier transform of the product of the rectangular window and the weight function:

$$W(\nu) = \int_{-\infty}^{\infty} p(t)w(t)\exp(j2\pi\nu t)dt = \int_0^{NT} w(t)\exp(j2\pi\nu t)dt \tag{2.36}$$

Finally, the delay Doppler response of the weighted correlation receiver is obtained from the convolution between (2.34) and (2.36), yielding

$$\left|\Psi(\tau,\nu)\right| = \sum_{n=-\infty}^{\infty} g_n(\tau)W(\nu - \frac{n}{T}) \tag{2.37}$$

The significance of this equation is that at any give coordinate (τ,ν), the delay-Doppler receiver response is determined by contributions from $g_n(\tau)$ and the weight function. The set of functions $g_n(\tau)$ is determined by (2.35) and depend on the transmitted signal modulation that is used.

Three important amplitude weighting windows have been described in [6] and can be defined by selecting the parameter c in the following expression

$$p(t)w(t) = \frac{1}{NT}\left(1 - \frac{1-c}{c}\cos\frac{2\pi t}{NT}\right) \tag{2.38}$$

where $0 \le t \le NT$ and zero elsewhere. For uniform, Hann, and Hamming weight windows, c is selected as $c = 1,\ 0.5,$ and 0.53836 respectively. Using (2.36) to transform $p(t)w(t)$ yields

$$W(\nu) = \frac{\sin(\pi\nu NT)}{\pi\nu NT}\left(1 + \frac{(1-c)(\nu NT)^2}{c\left[1-(\nu NT)^2\right]}\right)\exp(j\pi\nu NT) \tag{2.39}$$

With the exponent indicating that the weight function is not centered at $t = 0$. Still to be determined is the modulation function $g_n(\tau)$. Note that a smooth weight, covering N periods of the signal, affects only the Doppler behavior. It has no influence on the PACF (the zero Doppler cut of the PAF).

2.7 Ambiguity Function Computation in Phase Coded - Radars

Transmitted signal is given as:

$$s(t) = x(t) = A\exp\{j(2\pi f_c t + \phi(t))\} \tag{2.40}$$

and received signal is given as:

$$s_r(t) = y(t) = B\exp\{j[2\pi(f_c + f_d)(t - t_d) + \phi(t - td)]\} \tag{2.41}$$

where

f_d: Doppler shift frequency

t_d: range delay

$\phi(t)$: real phase modulation

And auto-ambiguity function can be defined as below [7];

$$\chi_u(\tau,\nu) = \int_t u(t+\frac{\tau}{2})u^*(t-\frac{\tau}{2})\exp(j2\pi\nu t)dt \tag{2.42}$$

Assuming transmitted and received signals are defined as (2.40) and (2.41)

$$\chi_x(\tau,\nu) = \int_t x(t+\frac{\tau}{2})x^*(t-\frac{\tau}{2})\exp(j2\pi\nu t)dt \tag{2.43}$$

$$= AB\int_t \exp\left\{ j\left[2\pi f_c(t+\frac{\tau}{2}) + \phi(t+\frac{\tau}{2}) \right]\right\} \cdot \exp\left\{ -j\left[2\pi f_c(t-\frac{\tau}{2}) + \phi(t-\frac{\tau}{2}) \right]\right\} \times \exp(j2\pi\nu t)\cdot dt \tag{2.44}$$

$$= AB\exp(j2\pi f_c\tau)\int_t \exp(j.\phi(t+\frac{\tau}{2}))\cdot\exp(-j.\phi(t-\frac{\tau}{2}))\times\exp(j2\pi\nu t)dt$$

$$= AB\exp(j2\pi f_c\tau)\int_t \exp\left\{ j\left[\phi\left(t+\frac{\tau}{2}\right) - \phi\left(t-\frac{\tau}{2}\right)\right]\right\}\times\exp(j2\pi\nu t)dt$$

$$= AB\exp(j2\pi f_c\tau)\int_t \exp\left\{ j\phi(t+\frac{\tau}{2})\right\}\cdot\left[\exp\left\{ j\phi\left(t-\frac{\tau}{2}\right)\right\}\right]^*\times\exp(j2\pi\nu t)dt$$

$$\text{let } u(t) = \exp(j\phi(t))$$

$$= AB\exp\left(j2\pi f_c t\right)\int_t u(t+\frac{\tau}{2})u^*\left(t-\frac{\tau}{2}\right)\times\exp(j2\pi f_c t) \tag{2.45}$$

$$\chi_x(\tau,\nu) = \exp(j2\pi f_c\tau)\chi_u(\tau,\nu) \tag{2.46}$$

$$\left|\chi_x(\tau,\nu)\right| = \left|\chi_u(\tau,\nu)\right| \tag{2.47}$$

As a result of eqn. (2.47) in computing the ambiguity surface $\left|\chi_x(\tau,\nu)\right|^2$ or simply $\left|\chi_x(\tau,\nu)\right|$, we can directly use the complex envelope $u(t) = \exp\{j\phi(t)\}$ instead of $x(t)$. That is, for ambiguity diagram calculation using base-band signal is adequate. There is no necessity of using transmitted or received signal with its carrier frequency.

Cross-ambiguity function can be defined as below [11];

$$\chi_{u,w}(\tau,\nu) = \int_t u(t+\frac{\tau}{2})w^*(t-\frac{\tau}{2})\exp(j2\pi\nu t)dt \tag{2.48}$$

Assuming transmitted and received signals are defined as (2.40) and (2.41)

$$\begin{aligned}\chi_{xy}(\tau,\nu) &= AB\int_t x(t+\frac{\tau}{2})\,y(t-\frac{\tau}{2})\exp(j2\pi\nu t)dt \\ &= AB\int_t \exp\left\{j\left[2\pi f_c\left(t+\frac{\tau}{2}\right)+\phi\left(t+\frac{\tau}{2}\right)\right]\right\} \\ &\quad\cdot\exp\left\{j\left[2\pi\left(f_c+f_d\right)\left(t-\frac{\tau}{2}-t_d\right)+\phi\left(t-\frac{\tau}{2}-t_d\right)\right]\right\}\times\exp\{j2\pi\nu t\}dt\end{aligned} \tag{2.49}$$

$$\begin{aligned}\chi_{xy}(\tau,\nu) &= AB\exp\{j2\pi f_c(\tau-t_d)\} \\ &\quad\cdot\int_t \exp\left\{j\phi\left(t+\frac{\tau}{2}\right)\right\}\exp\left\{-j\phi\left(t-\frac{\tau}{2}-t_d\right)\right\} \\ &\quad\cdot\exp\left\{-j2\pi f_d(t-t_d-\frac{\tau}{2})\right\}\times\exp(j2\pi\nu t)dt\end{aligned} \tag{2.50}$$

At eqn. (2.50) let

$$u(t+\frac{\tau}{2}) = \exp\left\{j\phi\left(t+\frac{\tau}{2}\right)\right\} \tag{2.51}$$

and then

$$\left[u(t-t_d-\frac{\tau}{2})\exp\left\{j2\pi f_d\left(t-t_d-\frac{\tau}{2}\right)\right\}\right]^* = \exp\left\{-\phi(t-td-\frac{\tau}{2})\right\}\exp\left\{-j2\pi f_d(t-t_d-\frac{\tau}{2})\right\} \tag{2.52}$$

Finally;

$$\chi_{xy}(\tau,\nu)=\exp\left\{j2\pi f_d(\tau-t_d)\right\}\chi_{u(t)u(t-t_d)\exp(j2\pi f_d(t-t_d))}(\tau,\nu) \tag{2.53}$$

$$\left|\chi_{xy}(\tau,\nu)\right|=\left|\chi_{u(t)u(t-t_d)\exp\left\{j2\pi f_d(t-t_d)\right\}}(\tau,\nu)\right| \tag{2.54}$$

From eqn. (2.54) we can see easily see that, instead of computing absolute ambiguity function for original transmitted and received signals, we can use the absolute value of ambiguity function computed between the phase functions. So, we do not have to use carrier frequency for computing absolute value of the ambiguity function [12].

Auto-ambiguity function for $u(t)=\exp\left\{j\phi(t)\right\}$ for a polyphase code;

$$\chi_u(\tau,\nu)=\int_t u\left(t+\frac{\tau}{2}\right)u^*\left(t-\frac{\tau}{2}\right)\exp\left\{-j2\pi\nu t\right\}dt \tag{2.55}$$

where

$$u(t)=\exp\left\{j\phi(t)\right\}=\cos\phi(t)+j\sin\phi(t) = \mathrm{Re}\left\{u(t)\right\}+j\,\mathrm{Im}\left\{u(t)\right\} \tag{2.56}$$

$$\chi_u(\tau,\nu)=\int_t\left[\cos\phi\left(t+\frac{\tau}{2}\right)+j\sin\phi\left(t+\frac{\tau}{2}\right)\right]\left[\cos\phi\left(t-\frac{\tau}{2}\right)-j\sin\phi\left(t-\frac{\tau}{2}\right)\right] \times\exp\left(j2\pi\nu\tau\right)dt \tag{2.57}$$

$$\chi_u(\tau,\nu)=\left[\chi_{\mathrm{Re}(u)}(\tau,\nu)+\chi_{\mathrm{Im}(u)}(\tau,\nu)\right]+j\left[\chi_{\mathrm{Im}(u)\mathrm{Re}(u)}(\tau,\nu)-\chi_{\mathrm{Re}(u)\mathrm{Im}(u)}(\tau,\nu)\right]$$

(2.58)

Special Case: For binary-phase codes $u(t)=\exp\{j\phi(t)\}=\cos\phi(t)$,

$\mathrm{Re}\{u(t)\}=u(t),\ \ \mathrm{Im}\{u(t)\}=0$.

$$\Rightarrow \chi_{\mathrm{Im}(u)}=0,\ \ \chi_{\mathrm{Im}(u)\mathrm{Re}(u)}=0,\ \ \chi_{\mathrm{Re}(u)\mathrm{Im}(u)}=0$$

$$\Rightarrow \chi_u(\tau,\nu)=\chi_{\mathrm{Re}\{u\}}(\tau,\nu)=\chi_{\cos\phi(t)}(\tau,\nu) \tag{2.59}$$

Cross-ambiguity function for $u(t)=\exp\{j\phi(t)\}$ for a polyphase code;

Let,

$$w(t)=u(t-t_d)\exp\{j2\pi f_d(t-t_d)\} \tag{2.60}$$

$$\chi_{u,w}(\tau,\nu)=\int_t u(t+\frac{\tau}{2})w^*(t-\frac{\tau}{2})\exp(j2\pi\nu t)dt \tag{2.61}$$

$$\begin{aligned}\chi_{u,w}(\tau,\nu)=\int_t\left[\cos\phi\left(t+\frac{\tau}{2}\right)+j\sin\phi\left(t+\frac{\tau}{2}\right)\right]\left\{\cos\phi\left(t-t_d-\frac{\tau}{2}\right)+2\pi f_d\left(t-t_d-\frac{\tau}{2}\right)\right.\\ \left.-j\sin\phi\left(t-t_d-\frac{\tau}{2}\right)+2\pi f_d\left(t-t_d-\frac{\tau}{2}\right)\right\}\\ \times\exp(j2\pi\nu t)dt\end{aligned} \tag{2.62}$$

$$\begin{aligned}\chi_{u,w}(\tau,\nu)=&\left[\chi_{\mathrm{Re}(u),\mathrm{Re}(w)}+\chi_{\mathrm{Im}(u),\mathrm{Im}(w)}\right]+\\ &j\left[\chi_{\mathrm{Im}(u),\mathrm{Re}(w)}-\chi_{\mathrm{Re}(u),\mathrm{Im}(w)}\right]\end{aligned} \tag{2.63}$$

Special Case: For binary-phase codes $u(t) = \exp\{j\phi(t)\} = \cos\phi(t)$,

$\mathrm{Re}\{u(t)\} = u(t), \;\; \mathrm{Im}\{u(t)\} = 0$.

$$\Rightarrow \chi_{\mathrm{Im}(u)} = 0, \;\; \chi_{\mathrm{Im}(u)\mathrm{Re}(u)} = 0, \;\; \chi_{\mathrm{Re}(u)\mathrm{Im}(u)} = 0$$

$$\chi_{u,w}(\tau,\nu) = \left[\chi_{\mathrm{Re}(u),\mathrm{Re}(w)}\right] - j\left[\chi_{\mathrm{Re}(u),\mathrm{Im}(w)}\right] \tag{2.64}$$

CHAPTER III

PHASE CODING CW RADARS

3.1 Introduction

This chapter is about the phase shift keying (PSK) techniques which are useful for LPI radar waveform design. First, Barker binary PSK is discussed, since it is the first PSK technique to be investigated and is still widely used today. This is followed by discussion of polyphase shift keying techniques. These techniques contain Frank code, P1, P2, P3, and P4 codes. All of these polyphase codes are useful for LPI CW radars due to its broadband characteristics. For each code that mentioned above, the phase characteristics are examined.

While Linear FMCW has established itself as one of the most popular LPI waveforms, PSK CW waveforms have recently been a topic of active investigation, due to the their wide bandwidth and inherently low Periodic Ambiguity Function (PAF) sidelobe levels achievable. For the LPI radar, it is important to have a low sidelobe level to avoid the sidelobes of large targets from masking the main peak of smaller targets. The choice of PSK code affects the radar performance and the implementation [4].

Barker code has high sidelobes and poor Doppler tolerance. Doppler tolerance is measured by how well the code compresses in the matched receiver when the received signal is Doppler shifted with respect to the reference code. In polyphase codes, phase shift value can take many values within on subcode duration. And also code period is extremely long for polyphase codes. These codes have lower sidelobes and better Doppler resolution than Binary phase codes (BPSK-Barker

codes). For this reason many LPI radar designers select polyphase coding techniques for their implementation.

Using PSK techniques high range resolution radar waveform can be obtained. PSK signals are also suitable for new digital signal processing hardware.

For PSK radars the transmitted complex signal can be written as

$$s(t) = A\exp\{j(2\pi f_c t + \phi_k)\} \tag{3.1}$$

where ϕ_k is the phase modulation function that is shifted in time, according to the type of PSK code being used, and fc is the angular frequency of the carrier. The inphase (I) and the quadrature (Q) representation of the complex signal from the transmitter can be represented as

$$I = A\cos(2\pi f_c t + \phi_k) \tag{3.2}$$

and

$$Q = A\sin(2\pi f_c t + \phi_k) \tag{3.3}$$

During a code period, phase of the CW signal is shifted N_c times, every subcode period with phase ϕ_k, according to specific code sequence. The code period T is defined as;

$$T = N_c t_b \text{ second} \tag{3.4}$$

where tb is subcode period.

The transmitted signal can be expressed as

$$u_T = \sum_{k=1}^{N_c} u_k \left[t - (k-1)t_b \right] \tag{3.5}$$

for $0 \le t \le T$ and zero elsewhere.

The complex envelope u_k is

$$u_k = e^{j\phi_k} \tag{3.6}$$

For $0 \le t \le t_b$ and zero otherwise. The range resolution of the phase coding CW radar is

$$\Delta R = \frac{ct_b}{2} \tag{3.7}$$

and the unambiguous range is

$$R_u = \frac{cT}{2} = \frac{cN_c t_b}{2} \tag{3.8}$$

If cpp is the number of cycles of the carrier frequency per subcode, the bandwidth of the transmitted signal is

$$B = \frac{f_c}{cpp} = \frac{1}{tb} \text{ Hz} \tag{3.9}$$

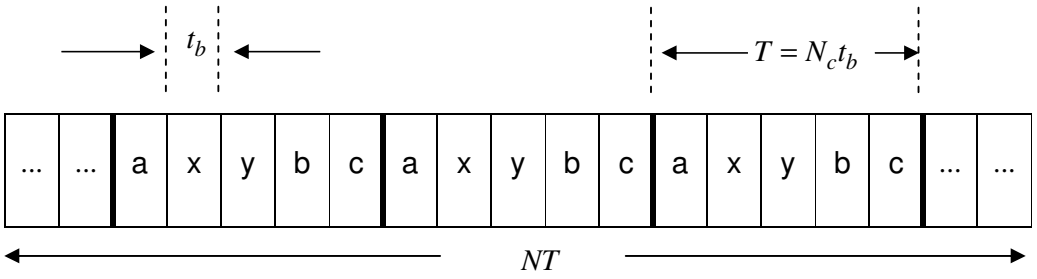

Figure 3.1: Representation of Phase coding CW radar transmitted waveform.

The received waveform from the target is digitized and correlated in the receiver using a matched (unweighted) or mismatched (weighted) filter that contains a cascade of N sets of Nc reference coefficients. The results from each correlation are combined to concentrate the target's energy and produce a compressed pulse having a time resolution equal to the subcode duration t_b and a height of N_c. For this

reason, the number of phase code elements N_c is also called the compression ratio. Recall that the PAF describes the range-Doppler performance of this type of receiver, and depends on the number of reference sets used [4].

3.2 Binary Phase Codes

In biphase (binary) phase codes, code period T is divided into N_c subcodes. Duration of the each subcode is represented as t_b and equal to T/N_c. Then, the phase of each subpulse is randomly chosen as 0 or π radians relative to some CW reference signal. It is customary to characterize a subpulse that has 0 phase (amplitude of +1 Volt) as either "1" or "+." Alternatively, a subpulse with a phase equal to π (amplitude of -1 Volt) is characterized by either "0" or "-."the compression ratio associated with binary phase codes is equal to N_c, and the peak value is N_c times larger than that of the long pulse. The goodness of a compressed binary phase code waveform depends heavily on the random sequence of the phase for the individual subpulses.

Probably the most famous family of phase codes is named Barker, after its inventor (Barker, 1953) [5, 13]. Originally, the Barker codes were designed as the sets of N_c binary phases yielding a peak to peak sidelobe ratio of N_c. The binary Barker sequences are finite length, discrete time complex sequences with constant magnitude, and a phase of either $\phi_k = 0$ or $\phi_k = \pi$ [14].

Consequently, a binary Barker sequence has elements $\{-1,+1\}$ which are only known for lengths N_c = 2, 3, 4, 5, 7, 11, and 13. Figure 3.2 illustrates concept for a Barker code of length thirteen. A Barker code of length n is denoted as B_n. Table 3.1 shows some known Barker codes with their peak side lobe level (PSL). PSL can be defined as

$$\text{PSL}=10\log_{10}\left[\frac{\text{Max side lobe power}}{(\text{Peak response})^2}\right] \tag{3.10}$$

For Binary case;

$$PSL = 10\log_{10}\left[\frac{(N_c)^2}{(1)^2}\right] = 20\log_{10} N_c \tag{3.11}$$

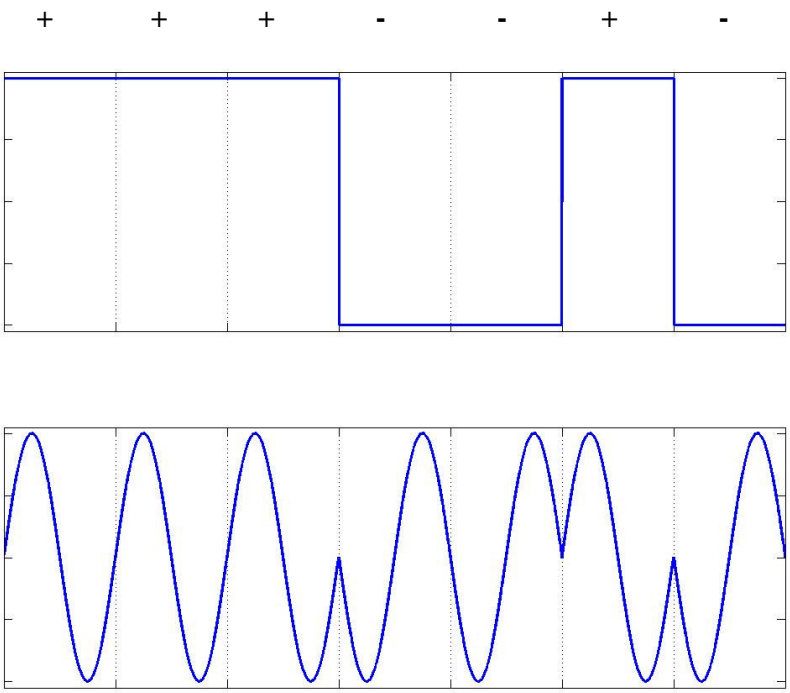

Figure 3.2: Binary phase code of length 7.

Table 3.1. Barker Codes with Corresponding PSL

Code length	Code elements	PSL (dB)
2	+−, −+	**6.0**
3	++−	**9.5**
4	++−+, +++−	**12.0**
5	+++−+	**14.0**
7	+++−−+−	**16.9**
11	+++−−−+−−+−	**20.8**
13	+++++−−++−+−+	**22.3**

The Barker codes are the most frequently used binary code since they result in an ambiguity function with side lobe levels, at zero Doppler, not higher than $1/N_c$ relative to a main lobe level of 1.

The most side lobe reduction offered by a Barker code is -22.3 dB, which may not be sufficient for desired radar application. However, Barker codes can be combined to generate much longer codes. In this case, a B_m code can be used within a B_n code (m within n) to generate a code of length mn. The compression ratio for the combined B_{mn} code is equal to mn. These Barker codes called as Compound Barker codes (Barker code within a Barker code). Although a larger compression gain is achieved, a larger compression gain is achieved; the peak side lobes are not proportionally decreased.

Some side lobes of a Barker code autocorrelation function can be reduced to zero if the matched filter is followed by a linear transversal filter. Assuming that, filter's

order is N and subcode duration is t_b. The filter of order N produces N zero side lobes on either side of the main lobe. The main lobe amplitude and width do not change.

In addition to having a limited code length, Barker codes are very sensitive to Doppler shifts. The Doppler shift of the return waveform (due to motion of the target) can compress the waveform within the filter such that the matched filter gives incorrect results. That is, these codes are only perfect in time domain (unknown range, zero Doppler shift). This characteristic restricts binary Barker code applications. As results, Barker codes are not considered LPI since they are easily detected by an intercept receiver that uses frequency doubling. Frequency doubling is a simple technique involves multiplying the receiver signal by itself and processing the result with an envelope detector [4].

The aperiodic autocorrelation function of the 13 – element Barker code is shown in Fig. 3.3. Fig. 3.4(a) shows the ACF of a CW signal phase coded with $N_c = 13$ - bit Barker sequence, and reveals the side lobe structure of the code. For the $N_c = 13$ - bit code shown $PSL = 20\log_{10}(N_c) = -22.3$ dB. Figure 3.4(b) reveals the fact that the Barker codes do not have a perfect PACF side lobe level that equals to PSL shown for the ACF (-22.3 dB). In figure 3.5, a plot of the PAF is shown for $N = 1$. The delay axis is normalized by the bit period t_b. Note the presence of the large Doppler side lobes.

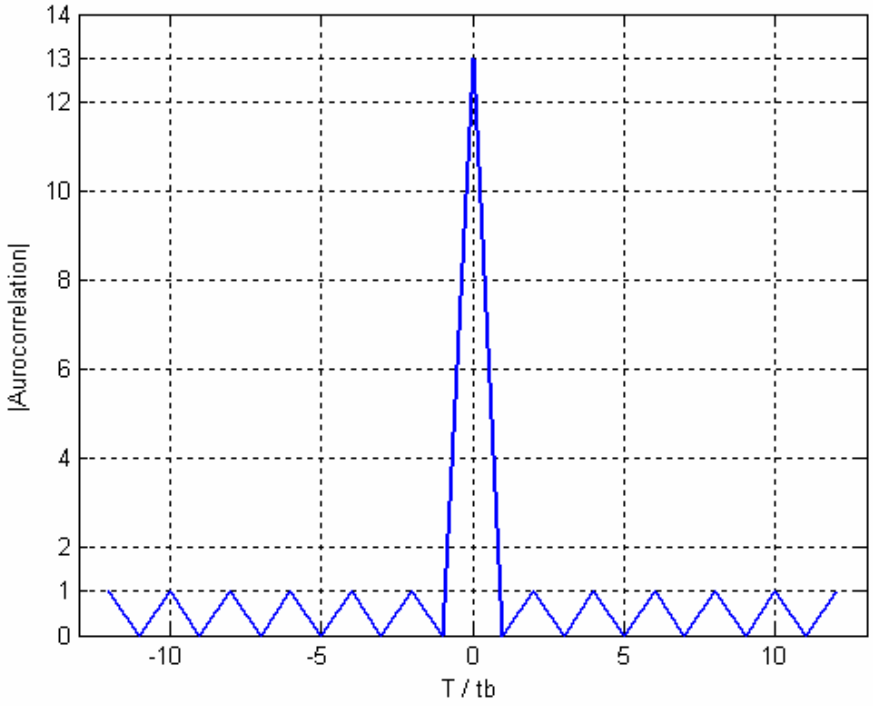

Figure 3.3: Autocorrelation function of a pulse coded using the 13-element Barker code.

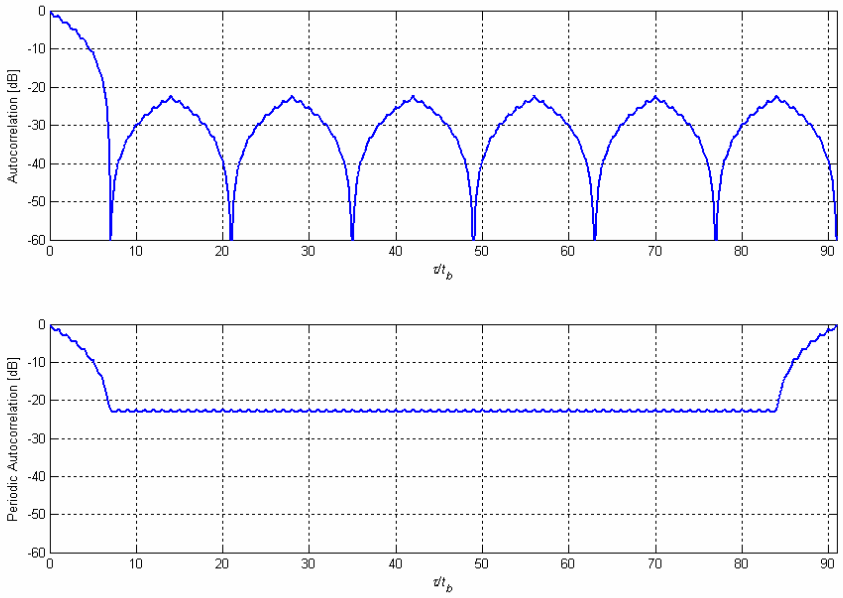

Figure 3.4: (a) ACF and (b) PACF for the $N_c = 13$ -bit Barker binary PSK signal.

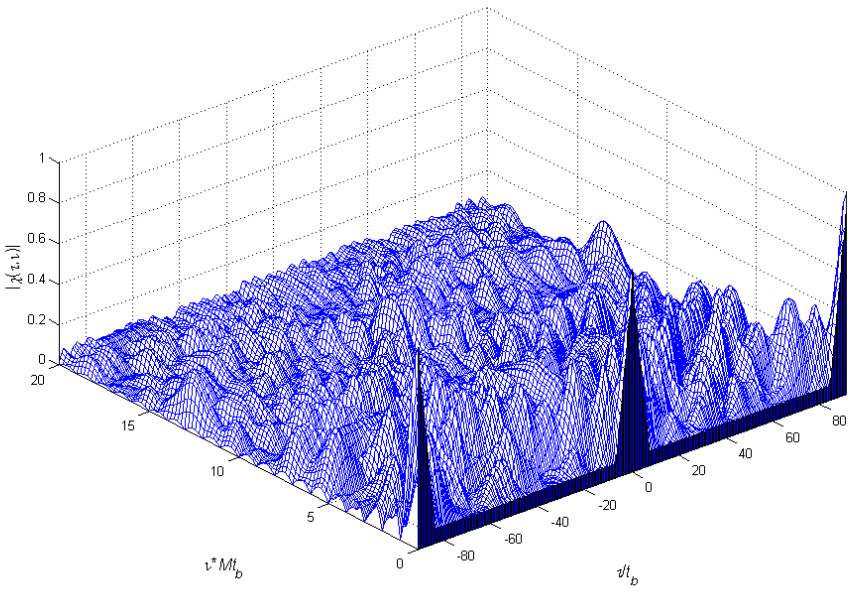

Figure 3.5: PAF for the 13-bit Barker binary PSK signal.

3.3 Polyphase Codes

Codes that use any harmonically related phases based on a certain fundamental phase increment are called polyphase codes. Polyphase codes exhibit better Doppler tolerance for broad range-Doppler coverage than do the biphase codes, and they exhibit relatively good side lobe characteristics.

Polyphase sequences are discrete time complex sequences with constant magnitude but with a variable phase ϕ_k. Polyphase coding refers to phase modulation of the CW carrier, with a polyphase sequence consisting of a number of discrete phases. The number of the sequence elements is greater than 2. Increasing the number of elements or phase values in the sequence allows the construction of longer sequences, resulting in a high range resolution waveform with greater processing gain in the receiver or equivalently a larger compression ratio. The trade-off is that a more complex matched filter is required compared to a Barker code filter. Note that a greater sequence length N_c does not affect the signal bandwidth at the antenna or change the transmitted signal bandwidth. Because, transmitted signal bandwidth depends on subcode period. ($B = 1/t_b$)

Polyphase compression codes have also been derived from step approximation to linear frequency modulation waveforms (Frank, P1, P2) and linear frequency modulation waveforms (P3, P4). These codes are derived by dividing the waveform into subcodes of equal duration, and using phase value for each subcode that best matches the overall phase trajectory of the underlying waveform. An alternate approach to approximating these waveforms is to quantize the underlying waveform into a user-selected number of phase states, where the time spent at each phase state changes (in time) throughout the duration of the waveform. These codes are referred to as polytime codes. Other codes, such as P(n,k) polyphase codes, have been derived using a step approximation of the phase function from a nonlinear frequency modulation waveform with favorable energy density.

The importance of polyphase coding to the LPI community is that by increasing the alphabet size N_c, the autocorrelation side lobes can be decreases significantly while

providing a larger processing gain. By narrowing the subcode t_b (so there are fewer cycles per phase), the transmitted signal can also be spread over a larger bandwidth, forcing the receiver to integrate over a larger band of frequencies.

3.4 Frank Code

The Frank code is a classical choice for the polyphase code which needs minimal phase quantization bits. The Frank code is derived from a step approximation to a linear frequency modulation waveform using M frequency steps and M samples per frequency [15]. The Frank code has a length $N_c = M^2$. In the case of a single side band detection, the result is the Frank code. As an example, consider that a local oscillator is at the start of the sweep of the step approximation to the linear frequency waveform. The first M samples of the polyphase codes are 0 phase. The second M samples start with 0 phase, and increase with phase increments of $\left(2\pi/M\right)$ from sample to sample. The third group of M samples start with 0 phase and increase with $(3-1)\left(2\pi/M\right)$ increments from sample to sample and so on.

If i is the number of the sample in a given frequency and j is the number of the frequency, the phase of the *ith* sample of the *jth* frequency is

$$\phi_{i,j} = \frac{2\pi}{M}(i-1)(j-1) \tag{3.12}$$

where $i = 1, 2, ..., M$ and $j = 1, 2, ..., M$.

The Frank polyphase code can also be written as an $M \times M$ matrix;

$$\begin{bmatrix} 0 & 0 & 0 & \cdots & \cdots & 0 \\ 0 & 1 & 2 & \cdots & \cdots & (M-1) \\ 0 & 2 & 4 & \cdots & \cdots & 2(M-1) \\ \vdots & \vdots & \vdots & \cdots & \cdots & \vdots \\ \vdots & \vdots & \vdots & \cdots & \cdots & \vdots \\ 0 & (M-1) & 2(M-1) & \cdots & \cdots & (M-1)^2 \end{bmatrix} \tag{3.13}$$

where the numbers represent multiplying coefficients of the basic phase angle $\left(2\pi/M\right)$.The construction method is demonstrated for 4 phase Frank code, that is $N_c = 16$ ($M = 4$). To calculate the phase values of the 16-element Frank code, we first write the 4×4 Frank matrix given by

$$\begin{bmatrix} 0 & 0 & 0 & 0 \\ 0 & 1 & 2 & 3 \\ 0 & 2 & 4 & 6 \\ 0 & 3 & 6 & 9 \end{bmatrix}$$

The phase increments within each row represent a stepwise approximation of an up-chirp LFM waveform. The phase increments for subsequent rows increase linearly versus time. Thus, the corresponding LFM chirp slopes also increase linearly for subsequent rows. This is illustrated in Fig. 3.6.

The 16-element Frank code is formed by concatenating the rows of the Frank matrix and multiplying by fundamental phase increment $\Delta\phi = 2\pi/M = 2\pi/4 = \pi/2$, resulting in the 16-element phase code given by

$$\left[0 \quad 0 \quad 0 \quad 0 \quad 0 \quad \frac{\pi}{2} \quad \pi \quad \frac{3\pi}{2} \quad 0 \quad \pi \quad 2\pi \quad 3\pi \quad 0 \quad \frac{3\pi}{2} \quad 3\pi \quad \frac{9\pi}{2}\right]$$

Taking the phase value modulo 2π gives

$$\left[0 \quad 0 \quad 0 \quad 0 \quad 0 \quad \frac{\pi}{2} \quad \pi \quad \frac{3\pi}{2} \quad 0 \quad \pi \quad 0 \quad \pi \quad 0 \quad \frac{3\pi}{2} \quad \pi \quad \frac{\pi}{2}\right]$$

The connection between the Frank code and a frequency stepped pulse is demonstrated in Fig. 3.7, showing the history of a 16-element Frank code. Note that the code is made from four equal segments of linear phase dependence (constant frequency). The segments' phase slope changes linearly from segment to segment implying linear frequency stepping between segments. Note also that the first phase in each section is obtained by a linear prediction based on the phase values of the previous section.

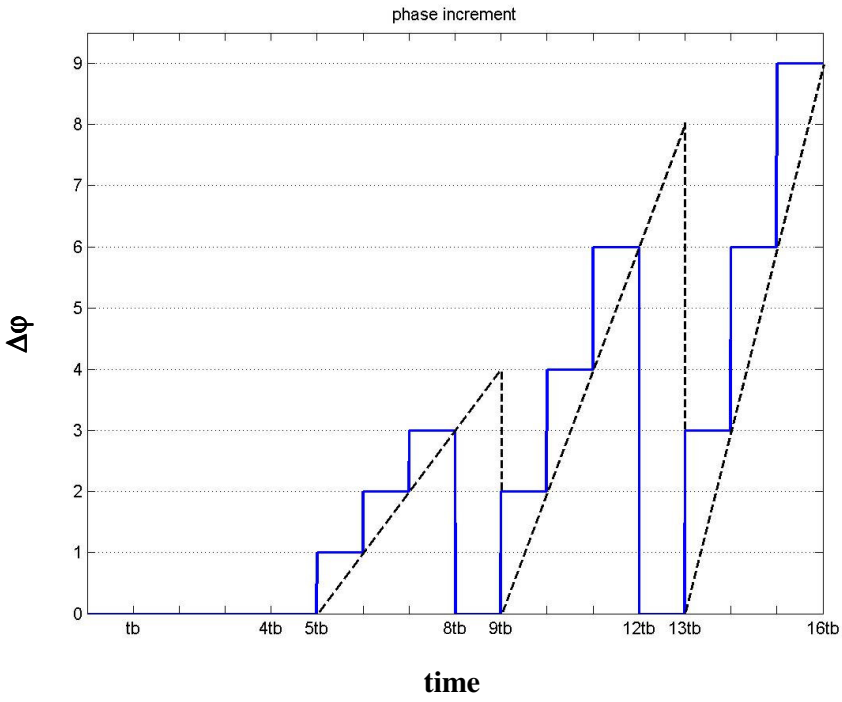

Figure 3.6: Stepwise approximation of an up-chirp waveform, using a Frank code of 16 elements.

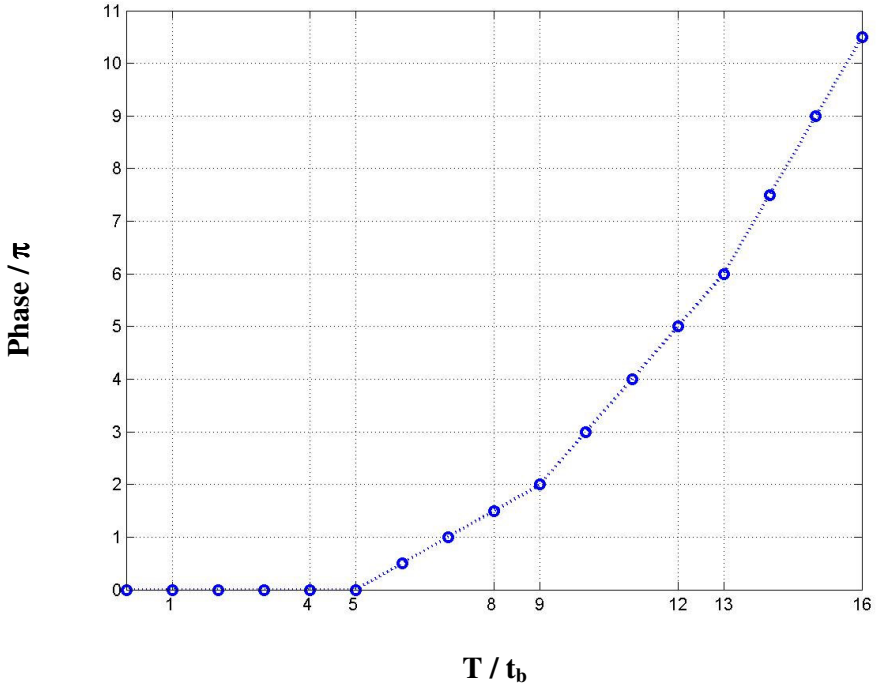

Figure 3.7 : Phase history of a 16 – element Frank code.

For the Frank Code PSL given as below [16];

$$PSL = 20\log_{10}\left(\frac{1}{M\pi}\right) \tag{3.14}$$

For $M = 8$, $Nc = 64$, the $PSL = 20\log_{10}\left(1/(M\pi)\right) = 20\log 10\left(1/8\pi\right) = -28dB$.

Let's consider the signal with the polyphase Frank coded sequences that is determined in the basic band. In this case the signal analytic formula is as follows [17]:

$$s(t) = \begin{cases} S(t)\sum_{k=0}^{N-1} rect\left[\frac{t-k\cdot t_b}{t_b}\right]\exp\{j\cdot\phi_k\} & \text{for } 0 \le t < N_c\cdot t_{sub} \\ 0 & \text{for other values of } t \end{cases} \tag{3.15}$$

where:

$S(t)$: envelope of the $s(t)$ signal,

k: subpulse number, $k = 0,1,2,.....,N-1$,

N_c: code sequence length (number of signal subpulses),

ϕ_k: phase argument of Frank code,

$rect[\bullet]$: unit pulse which is defined as:

$$rect\left[\frac{t-t_b}{t_b}\right] = \begin{cases} 1 & \text{for } k.t_b \le t \le (k+1).t_b \\ 0 & \text{for other values of } t \end{cases}$$

The k th phase element of the Frank code $\{\phi_k\}$ in linear transformation can be written:

$$\phi_k = \frac{2\pi}{M}\frac{\left[k-(k)\bmod M\right]}{M}\left[(k)\bmod M\right] \tag{3.16}$$

where:

M: any positive integer which defines code sequence length $N_c = M^2$,

$(k)\bmod M$: means that index k is reduced modulo M.

If the signal given by (3.15) is converted into digital form with sample rate $\Delta t = t_b$, and assuming that $S(t) = 1$, then k th signal sample with the polyphase Frank code sequence can be described as follows:

$$s_k = \exp\left\{ j.\frac{2\pi}{M}.\frac{\left[k-(k)\bmod(M)\right]}{m}(k)\bmod M \right\}, k = 0,1,....,N-1. \qquad (3.17)$$

In the radar application needed the sampling rate is higher than $\Delta t = t_b$. On the contrary the sampled signal may have distortioned spectrum and the range resolution of radar targets may be not sufficient. Assuming that the sampling period equals $\Delta t = t_b / s$, where s is number of the samples per subpulse, finally k th sample of s_k signal can be written as follows:

$$s_k = \exp\left\{ j\cdot\frac{2\pi}{M}\cdot\frac{\left[k-(k)\bmod(M\cdot s)\right]}{M\cdot s}\cdot\frac{(k)\bmod(m\cdot s)-\left((k)\bmod(m\cdot s)\right)\bmod s}{s} \right\}$$

$$\text{for } k = 0,1,.....,N\cdot s-1 \qquad (3.18)$$

The influence of the Doppler effect was not taken into consideration in the model described by equation (3.18).

Figure 3.8 shows the discrete phase values that result for the Frank code for $M = 8$, ($N_c = 64$). Figure 3.9 shows the signal phase modulo 2π, and demonstrates that the Frank code has the largest phase increments from sample to sample in the center of the code. Consequently, when the Frank code is passed through a bandpass amplifier in a radar receiver, the code is attenuated most heavily in the center of the waveform. This attenuation tends to increase the side lobes of the Frank code ACF. The aperiodic autocorrelation function of the 16 – element Frank code is shown in Fig. 3.10. The aperiodic autocorrelation exhibits relatively low sidelobes.

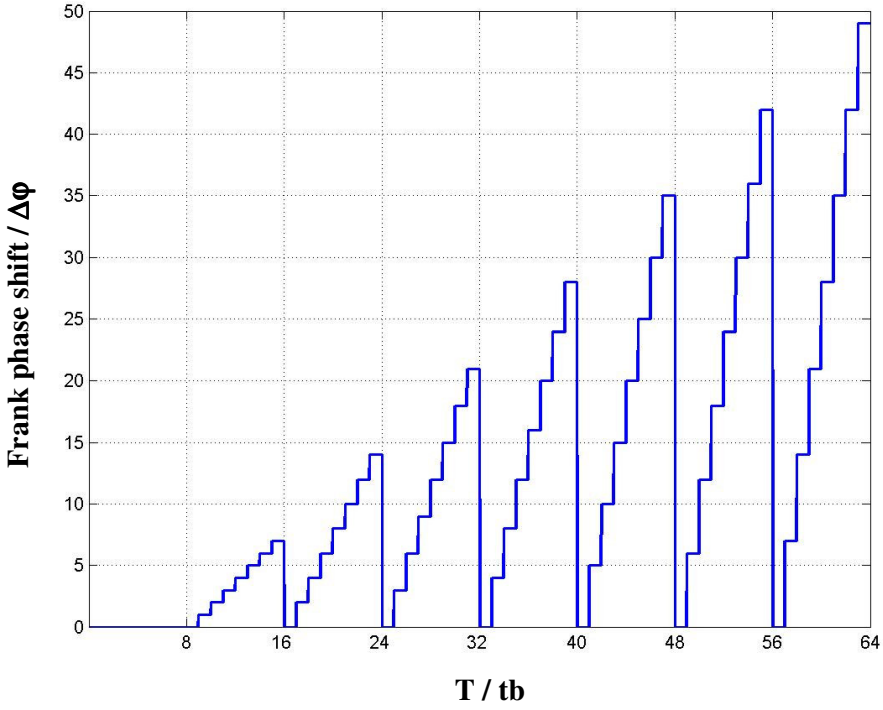

Figure 3.8: Frank code Discrete phase values for $M = 8$, $N_c = 64$.

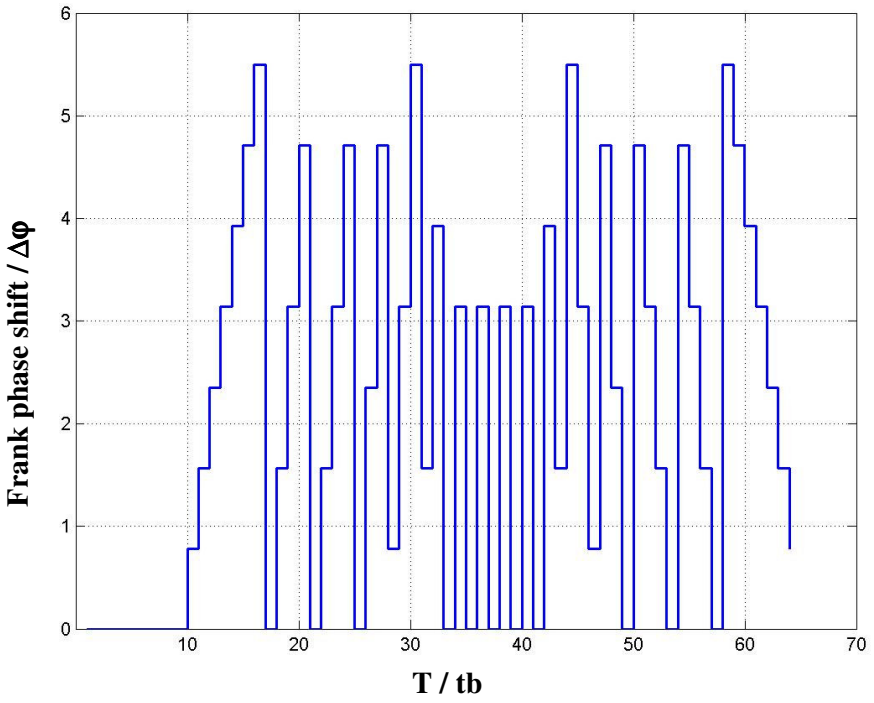

Figure 3.9: Frank code signal phase modulo 2π for $M = 8$, $N_c = 64$.

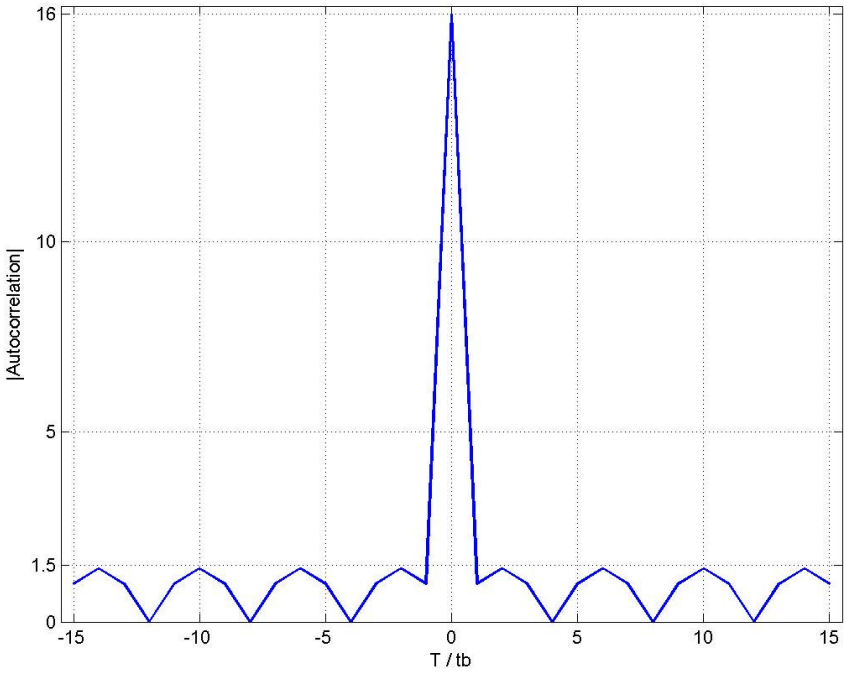

Figure 3.10: Autocorrelation function of a pulse coded using the 16 - element Frank code.

Figure 3.11(a) shows the ACF and the PACF for the $N_c = 64$ and $N = 1$. The ACF reveals the peak side lobe level $PSL = -28\ dB$. Figure 3.11(b) shows the PACF, and the fact that the Frank code has a perfect PACF. Figure 3.12 shows the PAF for the Frank code for $N_c = 64$ and $N = 1$. Note the delay and the Doppler side lobe levels are much lower than the BPSK code.

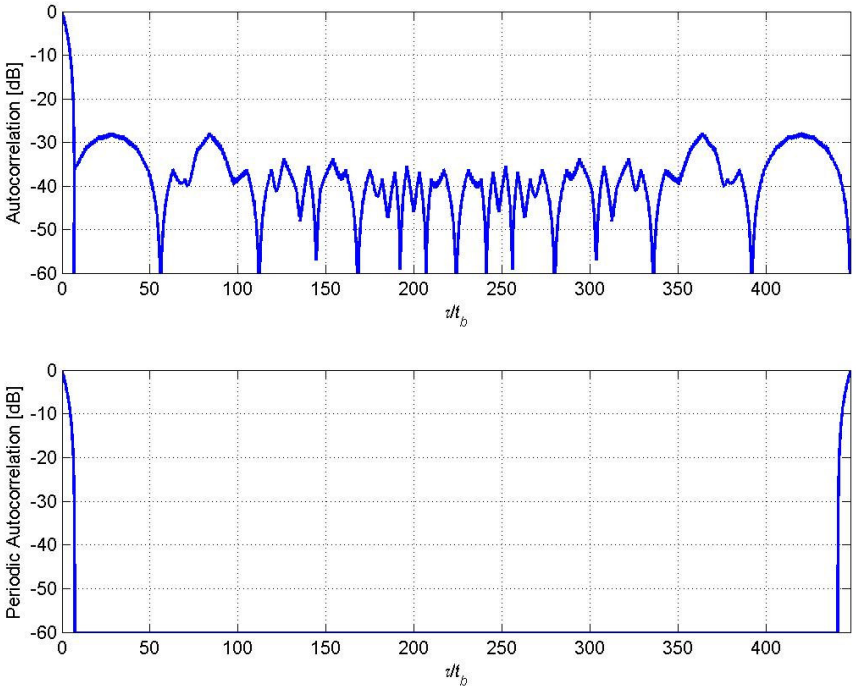

Figure 3.11: Frank code (a) ACF, and (b) PACF for $N_c = 64,\ N = 1.$

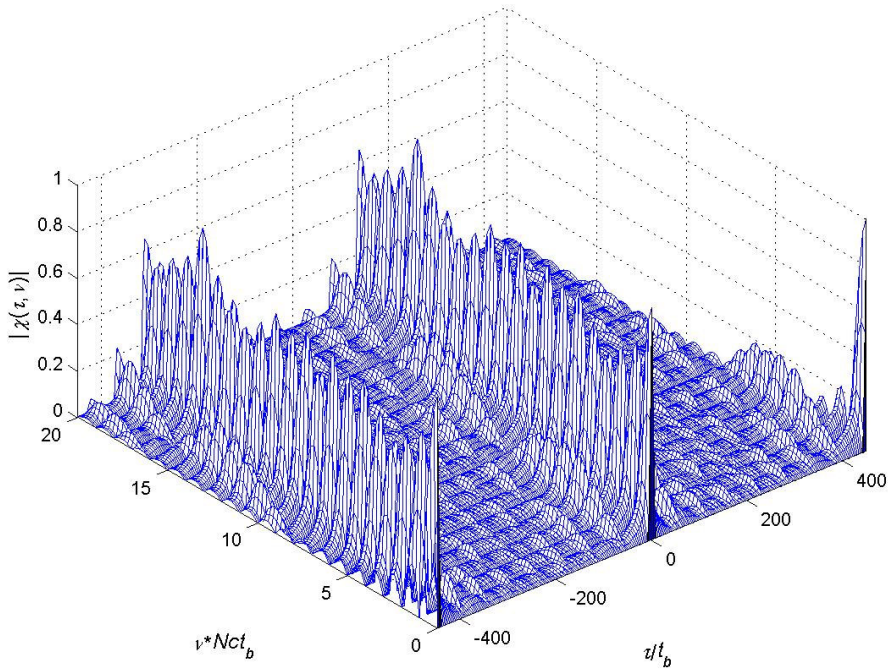

Figure 3.12: Frank code PAF for $N_c = 64,\ N = 1.$

3.5 P1 Code

The P1, P2, P3, and P4 codes are all modified versions of the Frank code, with the dc frequency term in the middle of the pulse instead of at the beginning. In the case of step approximation to linear frequency modulation with M frequency steps, M samples per frequency are obtained and M x M samples result. In the case of single sideband detection, the polyphase code that results is the Frank code and in the case of double sideband the code results is the P1 code [18].

If the detection is double sideband, i.e., if the local oscillator is at band center, the code will be the P1 code. The P1 code also consist of M x M elements and the phase of the i th element of the j th group may be expressed as

$$\phi_{i,j} = \left(\frac{-\pi}{M}\right)\left[M-(2j-1)\right]\left[(j-1)M+(i-1)\right] \qquad (3.19)$$

where $i = 1, 2, ..., M$, and $j = 1, 2, ..., M$. For the P1 code the $PSL = 20\log_{10}\left(1/(M\pi)\right) = 20\log_{10}\left(1/8\pi\right) = -28dB$ (the same as the frank code).

The difference between the frank and The P1 codes is that the Frank code has the highest phase increments from sample to sample in the center of the code and the P1 code has the highest phase increments from sample to sample at the two ends of the code. Thus, when waveforms phase coded with these codes are passed through band pass amplifiers in a radar receiver, the Frank code is attenuated most heavily in the center of the waveform while the P1 code is attenuated most heavily at the two ends of the waveform. This difference in attenuation over the waveform reduces the sidelobes of the P1 code autocorrelation function and increases those of the Frank code autocorrelation.

Figure 3.15(a) shows the ACF and the corresponding side lobe structure for the $N_c = 1$ and $N = 1$. Here, $PSL = -28$ dB down from the peak as predicted. Figure 3.15(b) shows the PACF. Note that the P1 code has a perfect PACF with zero side lobes. Figure 3.16 shows the corresponding PAF for the P1 code.

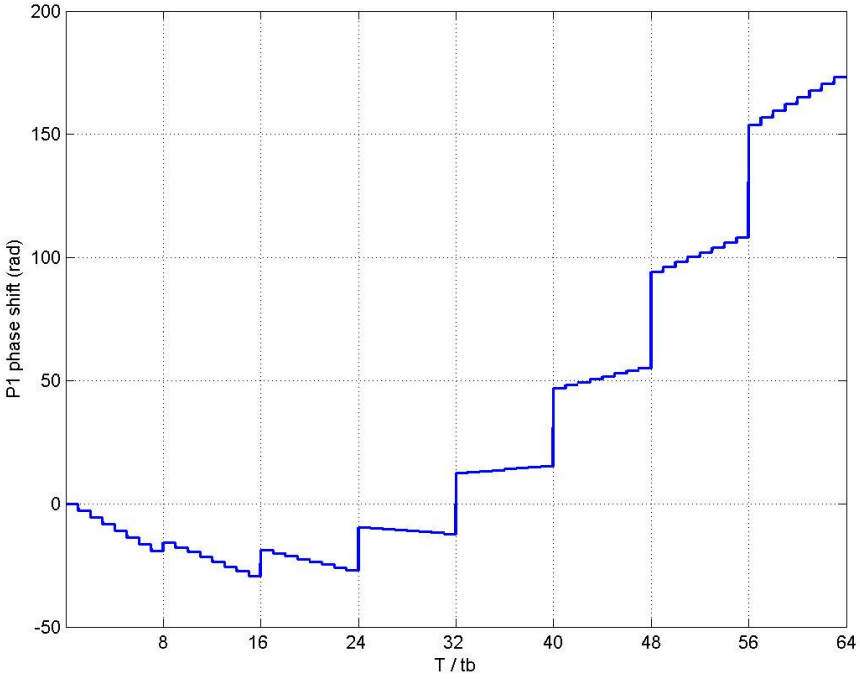

Figure 3.13: P1 code phase increment for $M = 8$ $(N_c = 64)$.

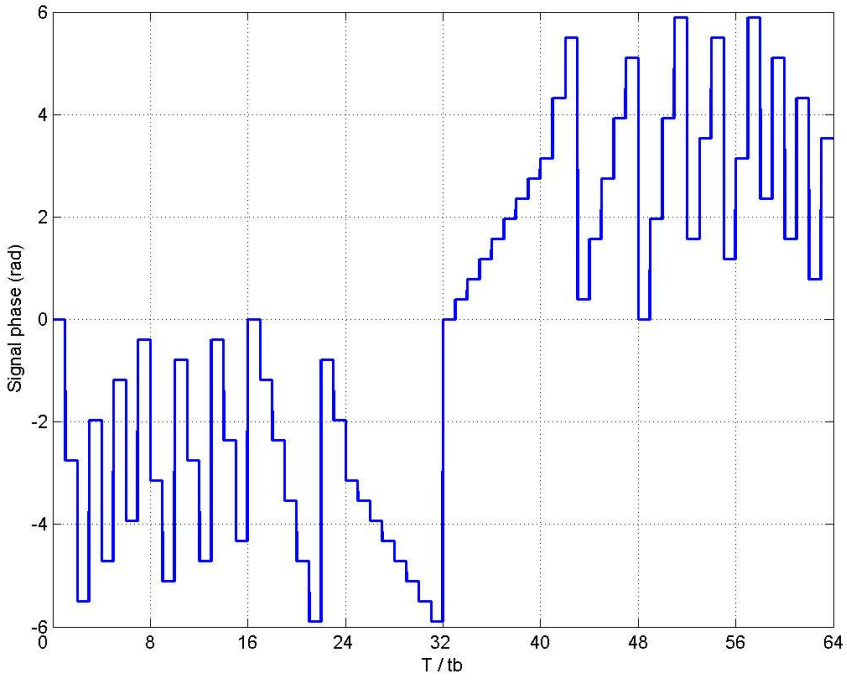

Figure 3.14 : P1 code signal phase modulo 2π for $M = 8$ $(N_c = 64)$

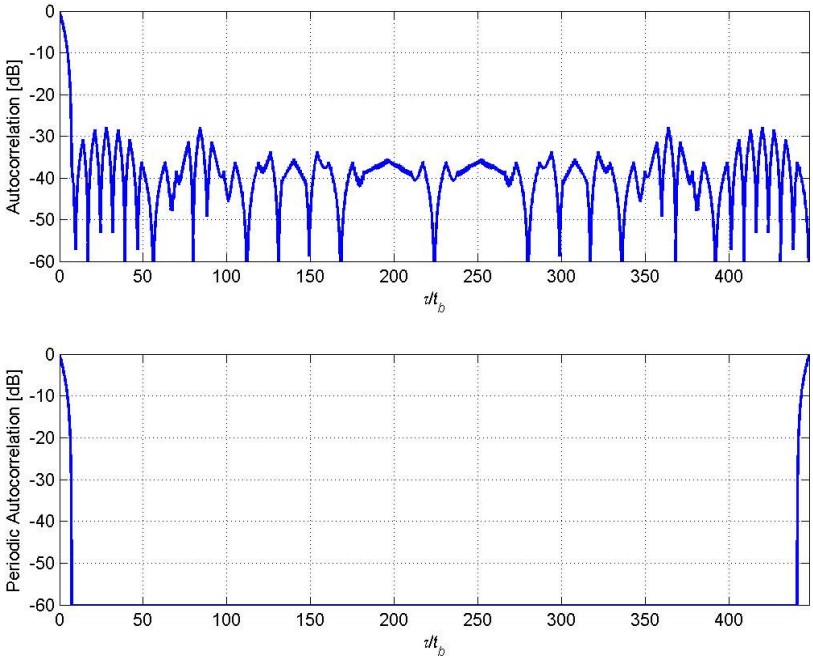

Figure 3.15: P1 code (a) ACF, and (b) PACF for $N_c = 64,\ N = 1$.

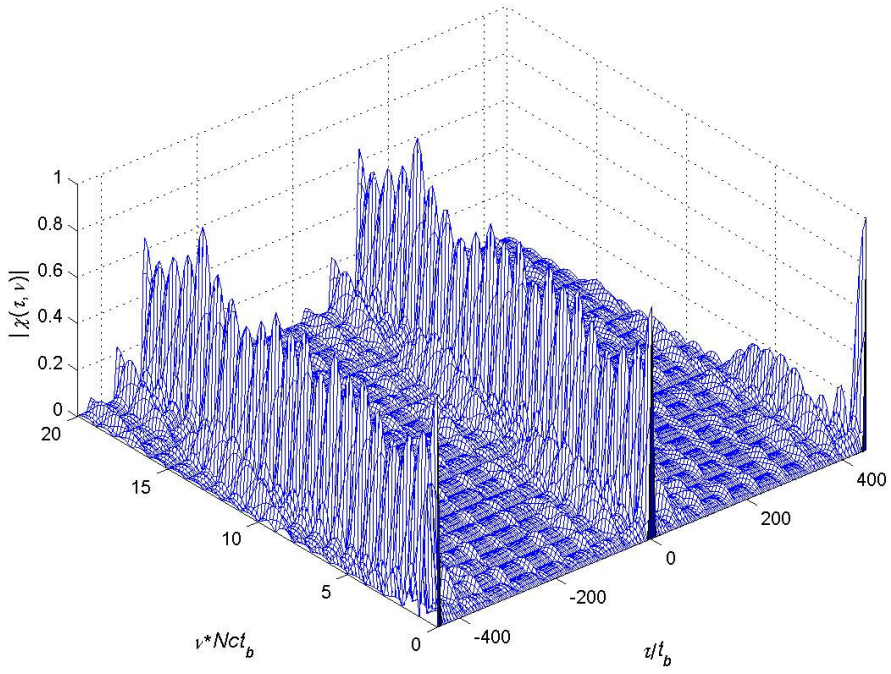

Figure 3.16: P1 code for $N_c = 64,\ N = 1$.

The aperiodic autocorrelation function of the 16 – element P1 code is shown in Fig. 3.17. The aperiodic autocorrelation exhibits relatively low sidelobes. Also note that autocorrelation function is same as the autocorrelation of the Frank code.

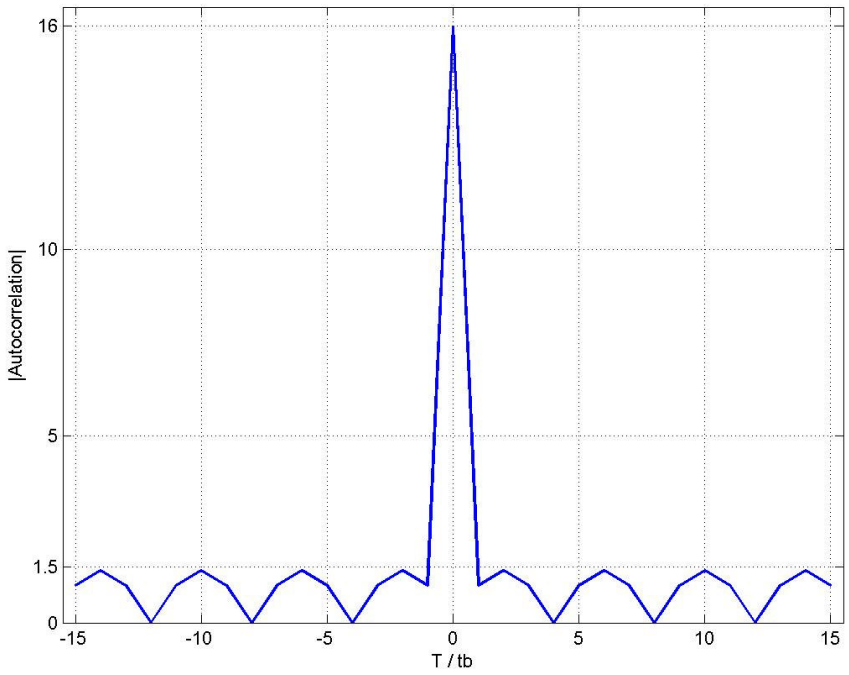

Figure 3.17: Autocorrelation function of a pulse coded using the 16 - element P1 code.

3.6 P2 Code

The phase increment within each phase group is the same as the P1 code, except that the starting phases are different. The P2 code also has a length or compression ratio of $N_c = M^2$. The P2 code is give by [19]

$$\phi_{i,j} = \left(\frac{-\pi}{2M}\right)\cdot\left[2i-1-M\right]\cdot\left[2j-1-M\right] \qquad (3.20)$$

where $i = 1, 2, ..., M$, and $j = 1, 2, ..., M$. The requirement for M to be even in this code stems from the desire for low autocorrelation side lobes. For the P2 code,

the $PSL = 20\log_{10}\left({}^{1}\!/\!_{(M\pi)} \right)$ and is the same as the Frank code and P1 code. The phase changes are largest toward the end of the code.

Figure 3.21(a) and (b) shows the corresponding ACF and PACF, respectively. Note that the P2 code does have not a perfect PACF. In fact, the PACF is identical to the ACF. Figure 3.22 shows the PAF for the P2 code for the P2 code for $N_c = 64,\ N = 1.$

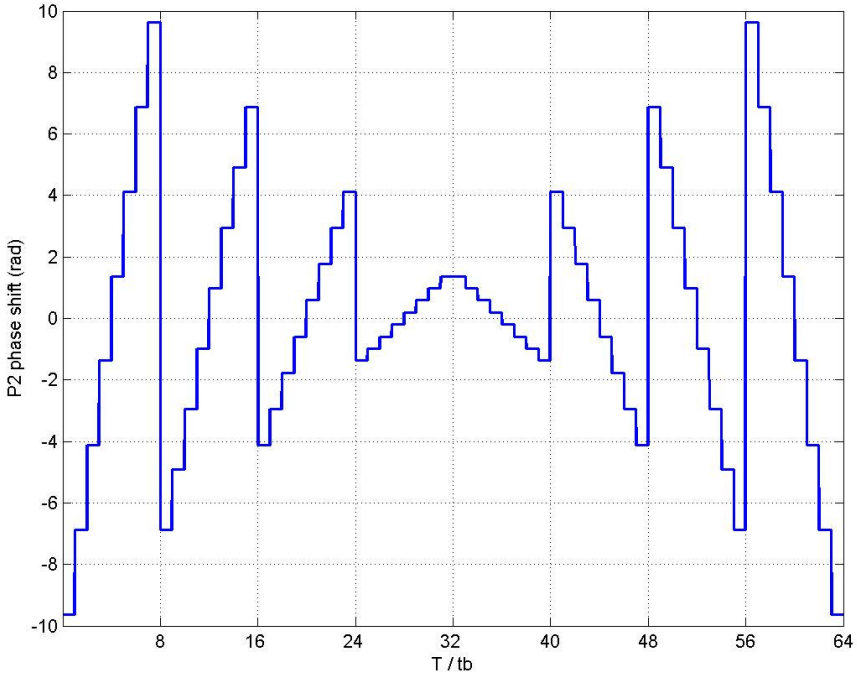

Figure 3.18: P2 code phase increment for $M = 8$ $(N_c = 64)$

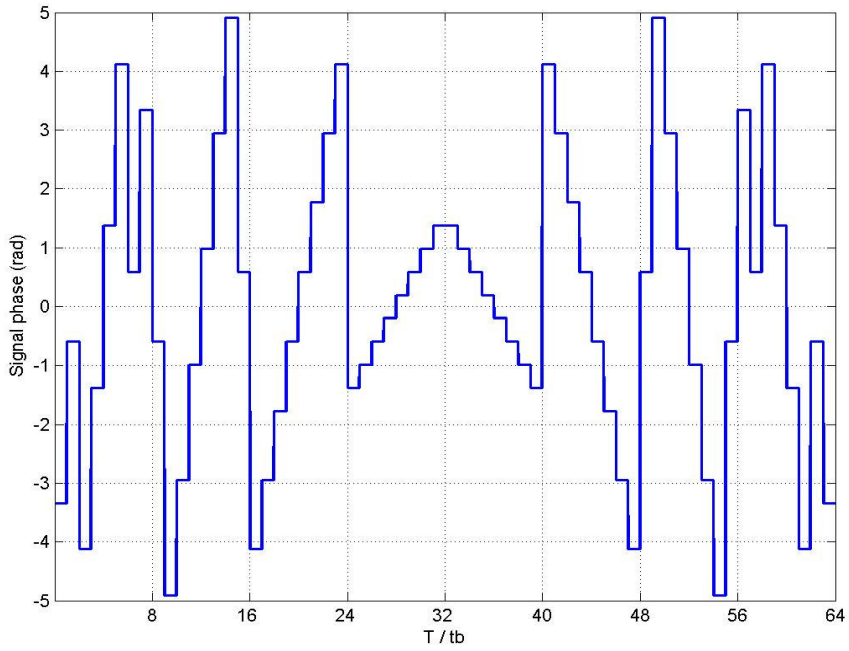

Figure 3.19 : P2 code signal phase modulo 2π for $M = 8$ $(N_c = 64)$

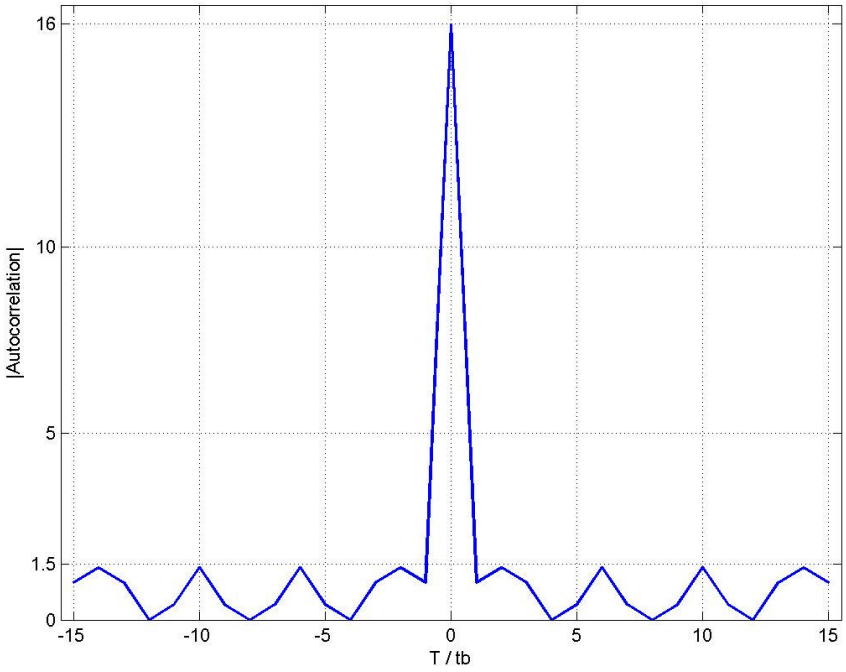

Figure 3.20: Autocorrelation function of a pulse coded using the 16 - element P2 code.

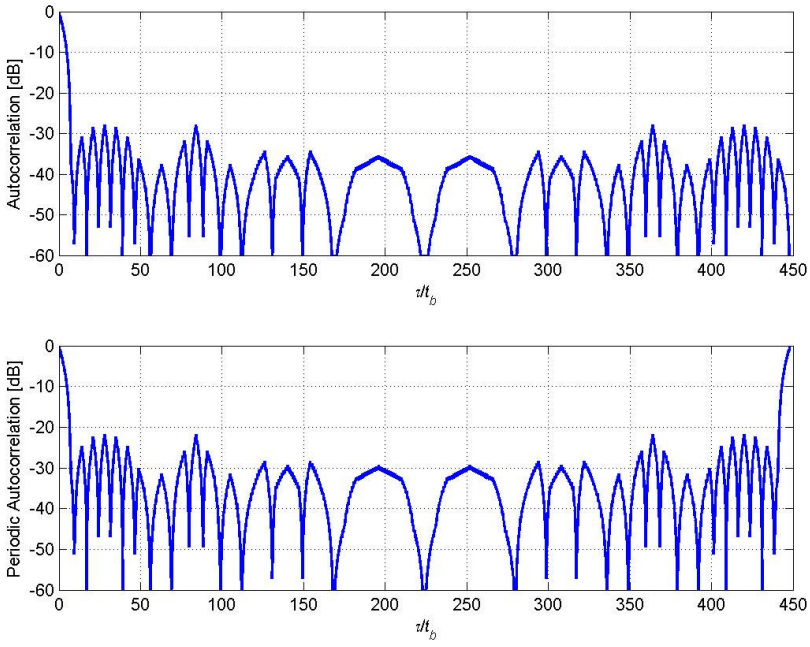

Figure 3.21: P2 code (a) ACF, and (b) PACF for $N_c = 64,\ N = 1$.

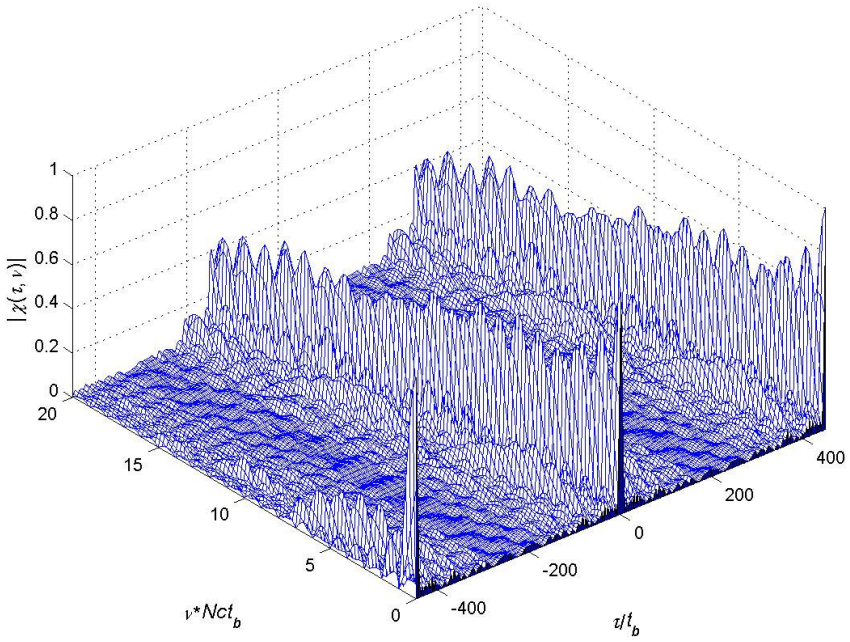

Figure 3.22: P2 code PAF for $N_c = 64,\ N = 1$.

3.7 P3 Code

The P3 code, suggested by Lewis and Kretschmer [20], are basically phase samples of a linear-FM signal. The phase sequence of the P3 signal is given by

$$\phi_i = \frac{\pi}{N_c}(i-1)^2 \tag{3.21}$$

where $i = 1, 2, ..., N_c$, and N_c is the compression ratio.

By converting a linear frequency modulation waveform to baseband, by using synchronous oscillator on one end of the frequency sweep (single sideband detection), and sampling the I and Q video at the Nyquist rate, the P3 code is derived.

In the P3 code, the largest phase increments occur at the center of the code. The P3 shares the intolerance to precompression band limiting associated with the Frank code.

The peak side lobe ratio for P3 code is a bit larger than the Frank, P1, P2 codes. For the P3 code $PSL = 20\log_{10}\left(\sqrt{2/\left(N_c\pi^2\right)}\right)$ dB, down from the peak. With $N_c = 64$, $PSL = -25dB$. This is revealed in Figure 3.26(a) which shows the corresponding ACF. Figure 3.26(b) shows the PACF for the P3 code and indicates that the P3 code has a perfect PACF. The PAF for the P3 code is shown in Fig. 3.27. Here $N_c = 64,\ N = 1.$

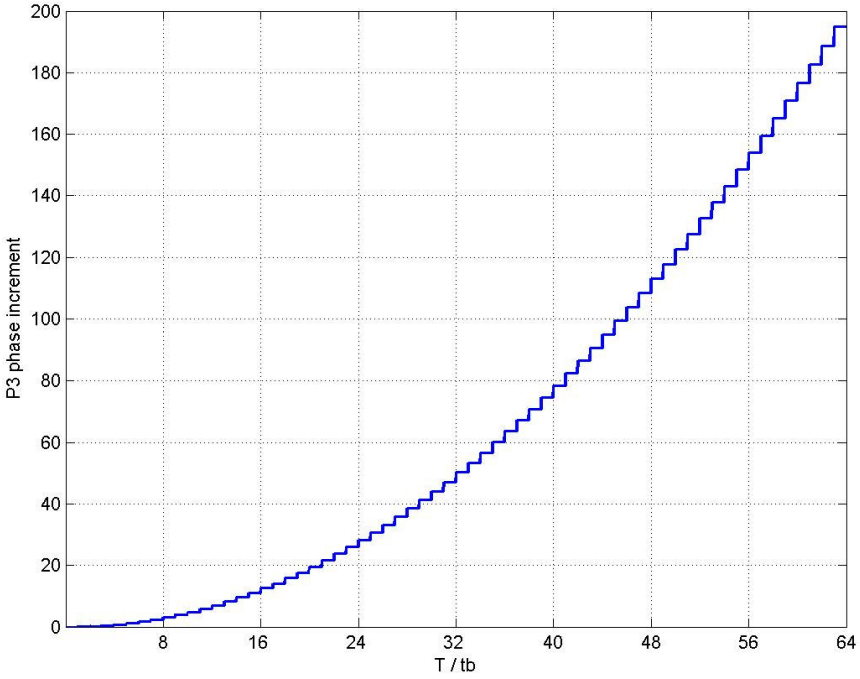

Figure 3.23: P3 code phase increment for $(N_c = 64)$

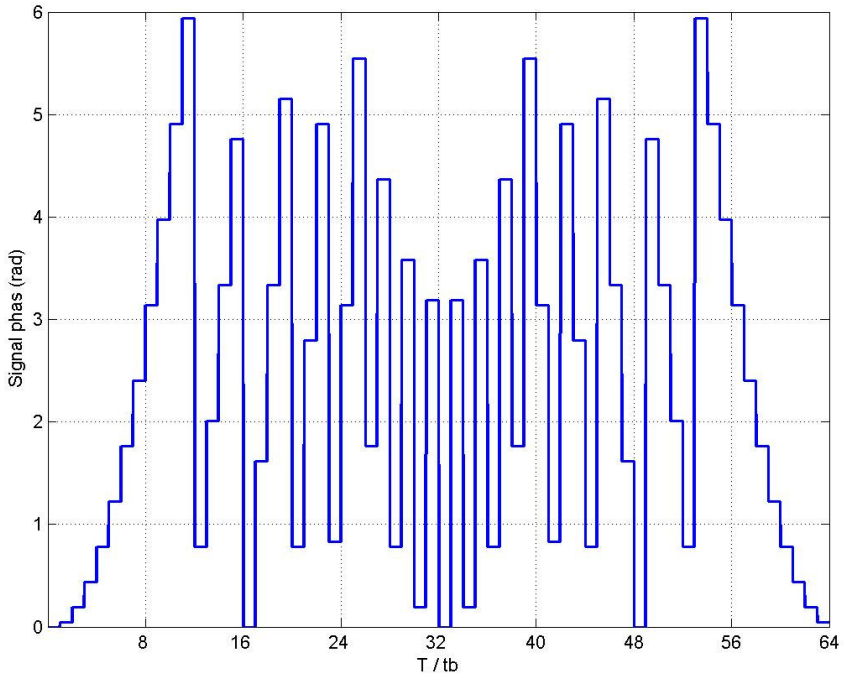

Figure 3.24 : P3 code signal phase modulo 2π for $(N_c = 64)$

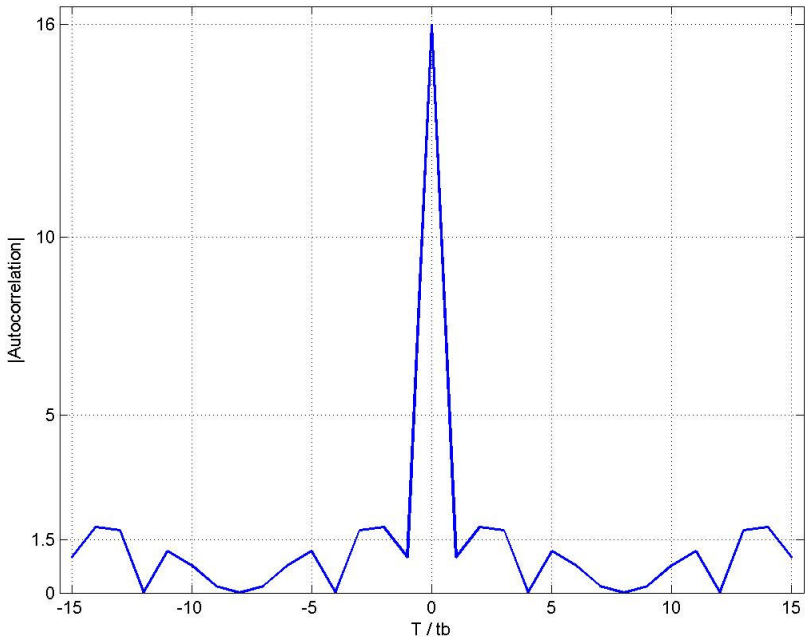

Figure 3.25: Autocorrelation function of a pulse coded using the 16 - element P3 code.

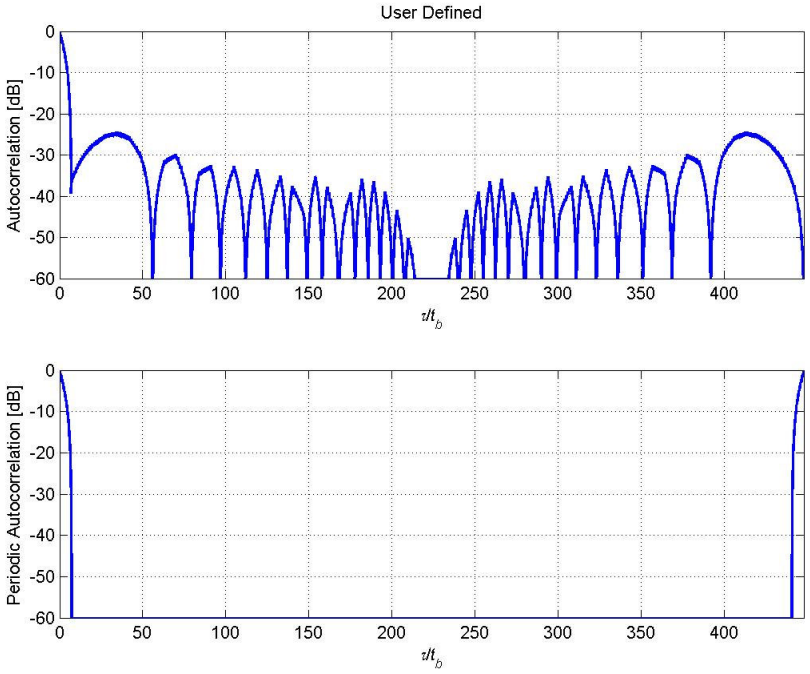

Figure 3.26: P3 code (a) ACF, and (b) PACF, for $N_c = 64,\ N = 1$.

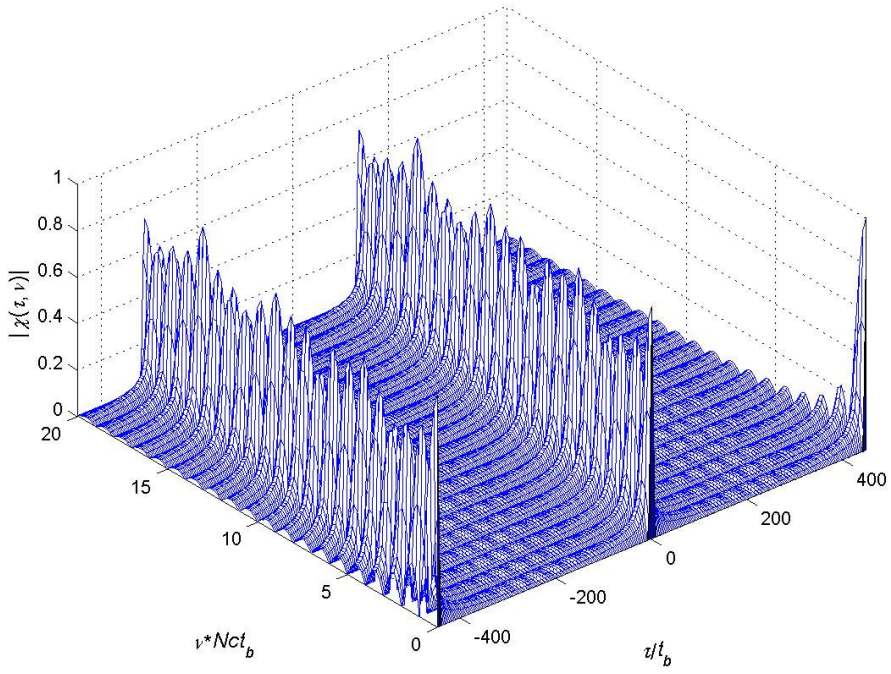

Figure 3.27: P3 code for $N_c = 64,\ N = 1$.

3.8 P4 Code

Conceptual coherent double sideband detection of a linear frequency modulation waveform and sampling at the Nyquist rate yields a polyphase code named the P4 code [18]. This code is similar to the P1 code in having the smallest phase increments from sample to sample on the center of the waveform instead of on the two ends like the P3 code. Here again, the P4 code is more tolerant of radar band limiting than the P3 code.

The phase of the i th sample of P4 code is given by

$$\phi_i = \left(\frac{\pi}{N_c}\right)\cdot(i-1)^2 - \pi\cdot(i-1) \qquad (3.22)$$

where $i = 1, 2, ..., Nc$ and N_c is the pulse compression ratio. The Doppler tolerance of the P3 and P4 codes are much greater than the Frank and P1 codes. They do not

have grating lobes that appear in the Frank and P1 waveform autocorrelation functions with increasing Doppler shift.

The P4 code consists of the discrete phases of the linear chirp waveform taken at specific time intervals, and exhibits the same range Doppler coupling associated with the chirp waveform. However, the peak side lobe levels are lower than those of the unweighted chirp waveform. Various weighting techniques can be applied to reduce the side lobe levels further [4].

The P4 code has its largest phase increments from sample to sample on the ends of the code, similar to the P1 code. For the P4 code $PSL = 20\log_{10}\left(\sqrt{2/\left(N_c\pi^2\right)}\right)$ (same as the P3 code). Fig. 3.31(a) shows the ACF and its corresponding side lobe structure for the $N_c = 64$ and $N = 1$. Figure 3.31(b) shows the PACF. The P4 is a Doppler tolerant perfect code in that exhibits a perfect PACF-namely zero PACF side-lobes.

Figure 3.32 shows the PAF for the P4 code for $N_c = 64$, $N = 1$. Note that the side lobe levels are smaller compared to nonperfect PACF codes, such as the BPSK and P2 code.

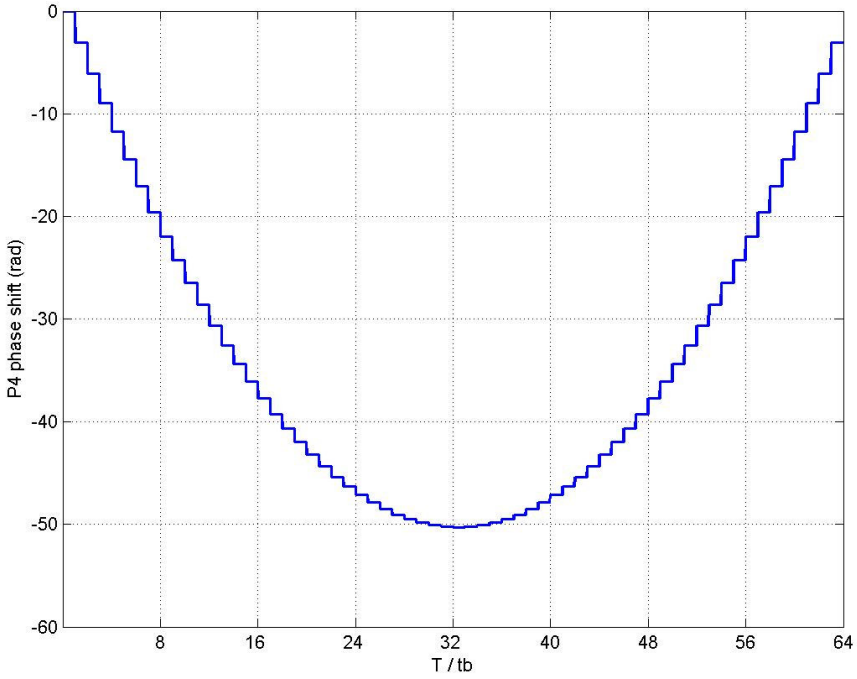

Figure 3.28: P4 code phase increment for $(N_c = 64)$

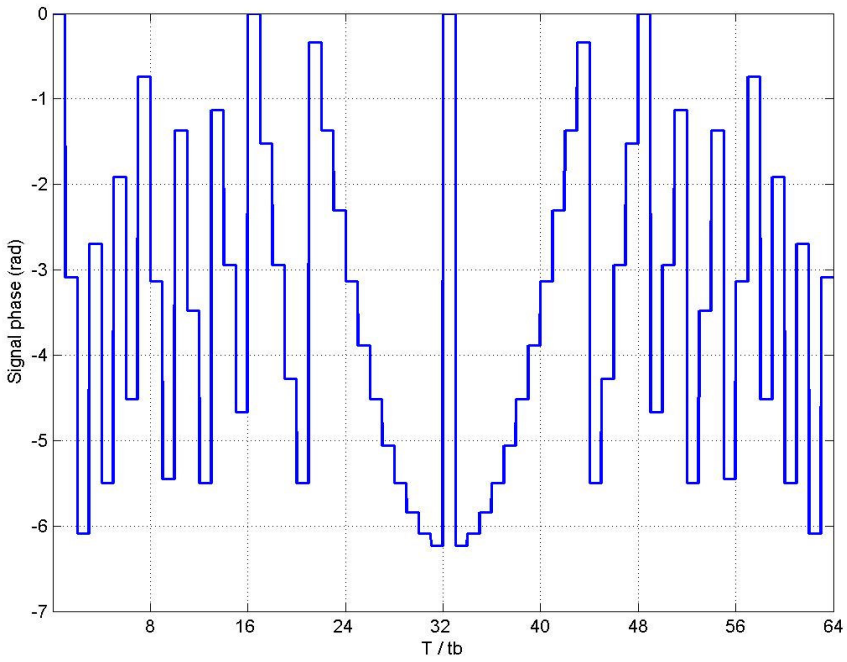

Figure 3.29 : P4 code signal phase modulo 2π for $(N_c = 64)$.

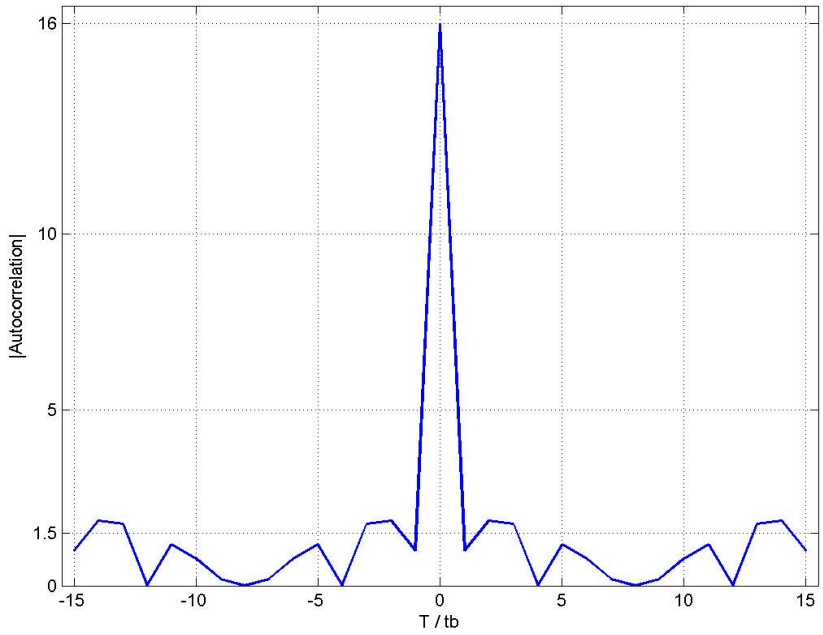

Figure 3.30: Autocorrelation function of a pulse coded using the 16 - element P4 code.

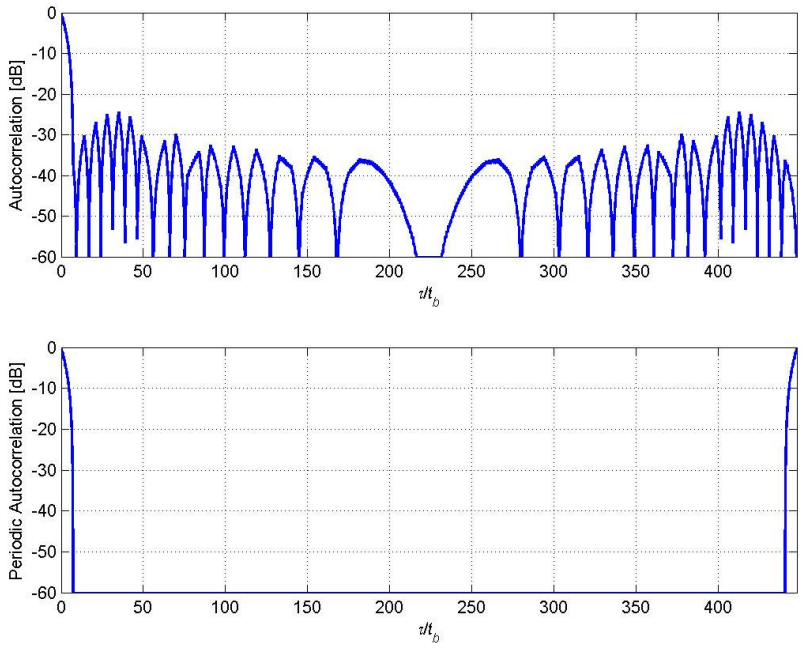

Figure 3.31: P4 code (a) ACF, and (b) PACF, for $N_c = 64,\ N = 1$.

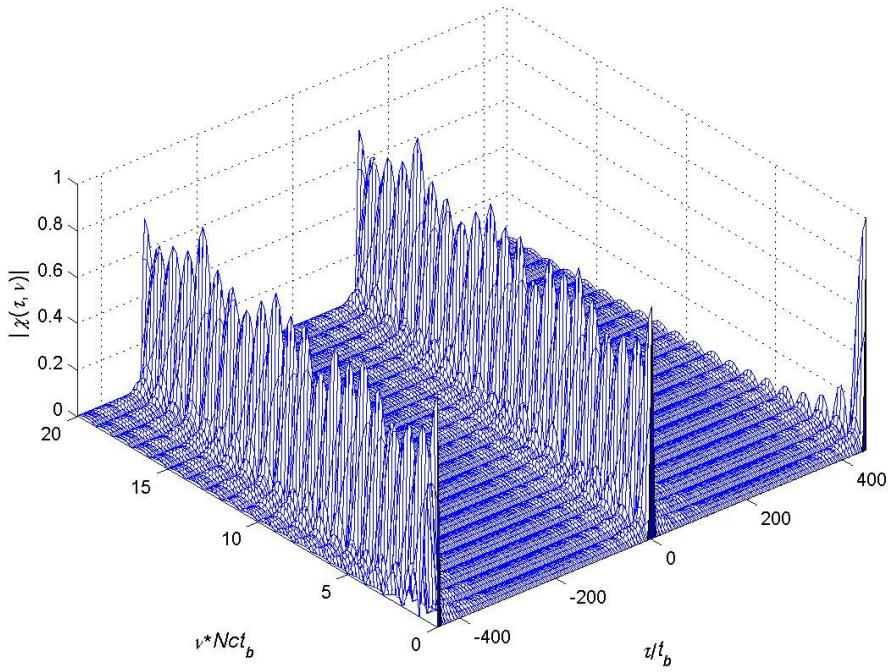

Figure 3.32: P4 code PAF for $N_c = 64,\ N = 1$.

CHAPTER IV

APPLICATIONS OF TARGET DETECTION

4.1 Introduction

In this chapter, Frank, P1, P2, P3, and P4-polyphase codes are examined for target detection by using ambiguity function. Details of the simulation study are presented and various target detection scenarios are tested. All simulations are performed by using MATLAB Programming Language.

At these scenarios, following parameters are commonly used:

$f_c = 35\ GHz$, $V_{\max} = 300\ m/\sec$, $N = 1$, $N_c = 1024$, $t_b = 0{,}1067\ \mu s$.

where f_c: carrier frequency, $V_{\max}$: maximum target velocity, N: number of the code period, N_c: number of subcodes, t_b: subcode period.

$$T(\text{code period}) = N_c t_b = 1024 \cdot 0{,}10667.10^{-6} = 0{,}10923 \text{ ms.} \tag{4.1}$$

$$\Delta R(\text{range resolution}) = \frac{ct_b}{2} = \frac{3.10^8 \times 0{,}1067.10^{-6}}{2} = 16 \text{ m.} \tag{4.2}$$

$$R_{\max}(\text{unambiguous range}) = \frac{cT}{2} = \frac{cN_c t_b}{2} = \frac{3.10^8 \times 1024 \times 0{,}10667.10^{-6}}{2} = 16384 \text{ m.} \tag{4.3}$$

$$\Delta f(\text{Doppler resolution}) = \frac{1}{NT} = 9155 \text{ Hz.} \tag{4.4}$$

$$\Delta v = \frac{\Delta f_d \cdot c}{2 f_c} = \frac{9155 \times 3.10^8}{2 \times 35.10^9} = 39,24 \text{ m/s.} \quad (4.5)$$

4.2 Single Target Scenarios

In this section, all simulations are performed by using 1024-element codes of Frank, P1, P2, P3 and P4 coding types.

4.2.1 Scenario 1: Target at a Close Range

At this simulation there is one target which is 2500 meter far from the radar, having 250 m/sec. radial velocity with respect to the radar, i.e. $R = 2500$ m. and $v_r = 250$ m/sec.

The transmitted CW signal is first coded by using the Frank code with $M = 32$ ($N_c = 1024$). The resulting cross-contour plot for the ambiguity function of the transmitted and received radar signal is given in Figure 4.1. The portion of the plot around the peak point is enlarged in Figure 4.2 to examine the details for range resolution and Doppler resolution. The three-dimensional AF (Ambiguity Function) plot is also given in Figure 4.3 to see the levels of side lobes. Side lobe level and resolution information are further displayed in 4.4 and 4.5 where the cross-sections of the 3D AF plots are given along range axis and velocity axis, respectively.

It is observed on these figures that the target is detected at about $R = 2501,05$ m. with $v_r = 250,91$ m/sec. The percentage errors in range and radial velocity are calculated by eqn. 4.6.

$$\varepsilon = \frac{|\text{measured value-actual value}|}{\text{actual value}} \times 100 \quad (4.6)$$

$$\varepsilon_{range} = \frac{|2501,05 - 2500|}{2500} \times 100 = 0,0420\,\%$$

$$\varepsilon_{velocity} = \frac{|250,91 - 250|}{250} \times 100 = 0,364\,\%$$

As seen in Figure 4.4 and 4.5, the side lobes of the AF plot are lower than 50% of the normalized peak magnitude of one at the largest point. It is also observed that, the side lobe magnitudes quickly decay along the range axis as we move farther away from the target location but the decay in the side lobe levels along the velocity axis is negligible.

After the Frank code, the P1 code is applied to the transmitted CW radar signal with the results presented in Figures 4.6 through 4.10. The accuracy levels in range and radial velocity of the target are about same as those found for Frank code case. Next, the codes P2, P3, and P4 with the same length of $Nc = 1024$ are utilized in signal coding for the same target detection problem. Based upon the simulation results displayed in Figures 4.11 through 4.25 it is concluded that the values of the detected range and radial velocity remain the same. The side lobe behaviors of the P1 and P2 codes are same as the side lobe behavior of Frank code. On the other hand, at the ramp time, the side lobe levels both along range and velocity axes tend to increase slightly in P3 and P4 coding simulations.

For all coding types, the accuracy levels in range and radial velocity of the target are the same. Also, for all coding types, the measurement precision in range and radial velocity of the target are the same which is an expected result. This is because, range resolution is related to c (light velocity) and t_b (subcode period), Doppler resolution is related to N (number of the code period), N_c (number of subcodes), and t_b (subcode period). All of these variables are selected to be the same for all the code types for easy comparison purposes.

If figures (Figure 4.1- Figure 4.25) are investigated, it can be seen easily that the target is detected successfully. The target is seen at expected range and radial velocity for all coding types. The simplicity in the computation of the Frank code can be considered as an advantage.

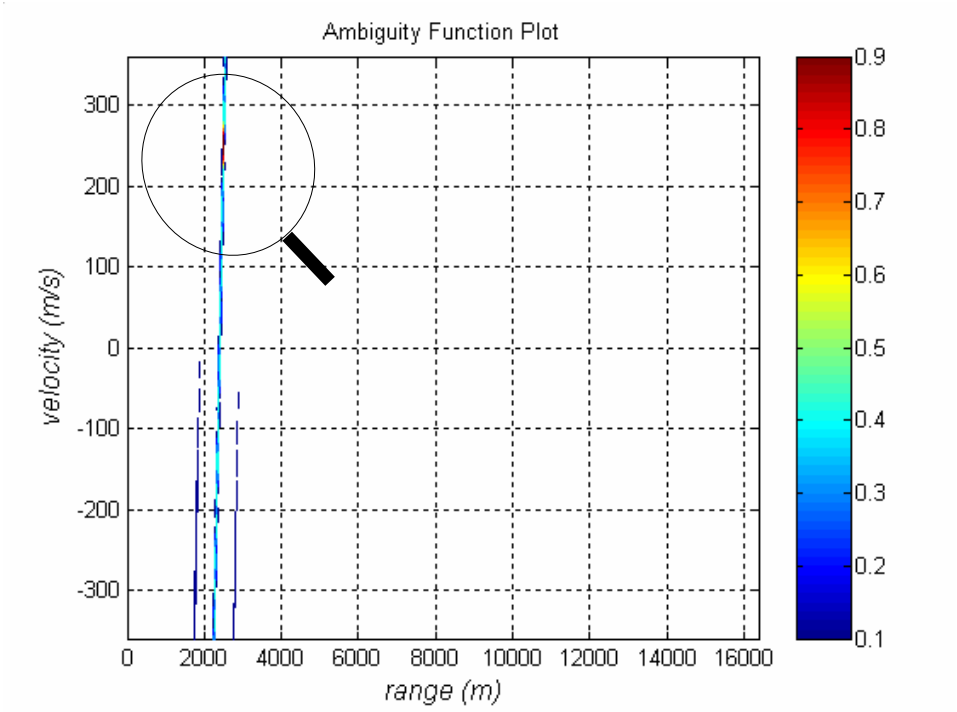

Figure 4.1: 2D Cross - Ambiguity Function of the transmitted and received signal for $M = 32$ ($N_c = 1024$) Frank code. ($R = 2,5\text{km},\ v = 250m/\sec.$)

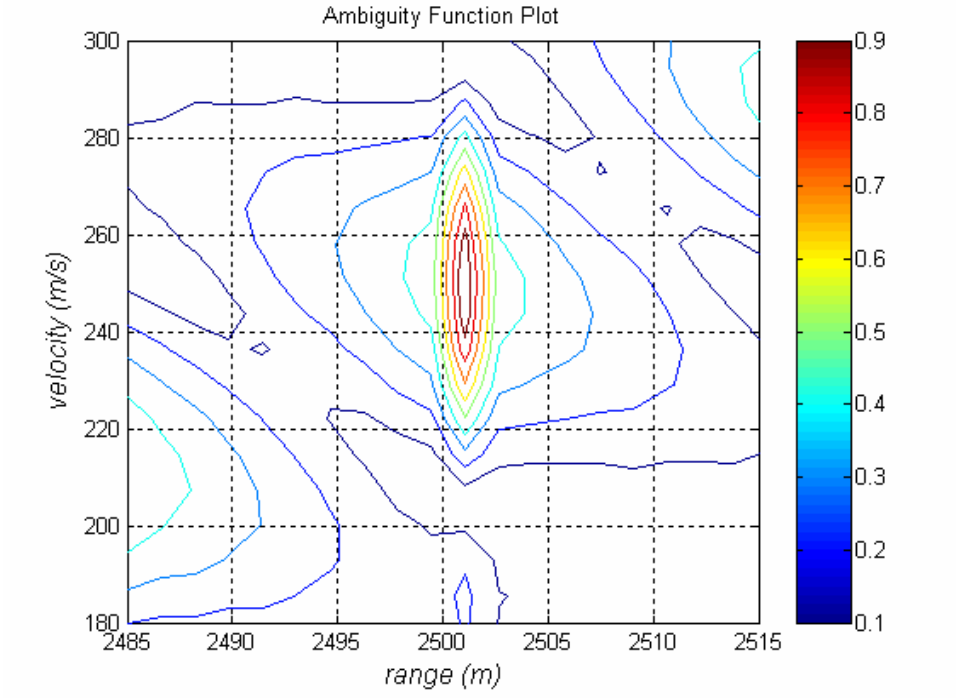

Figure 4.2: Close-up illustration of Figure 4.1

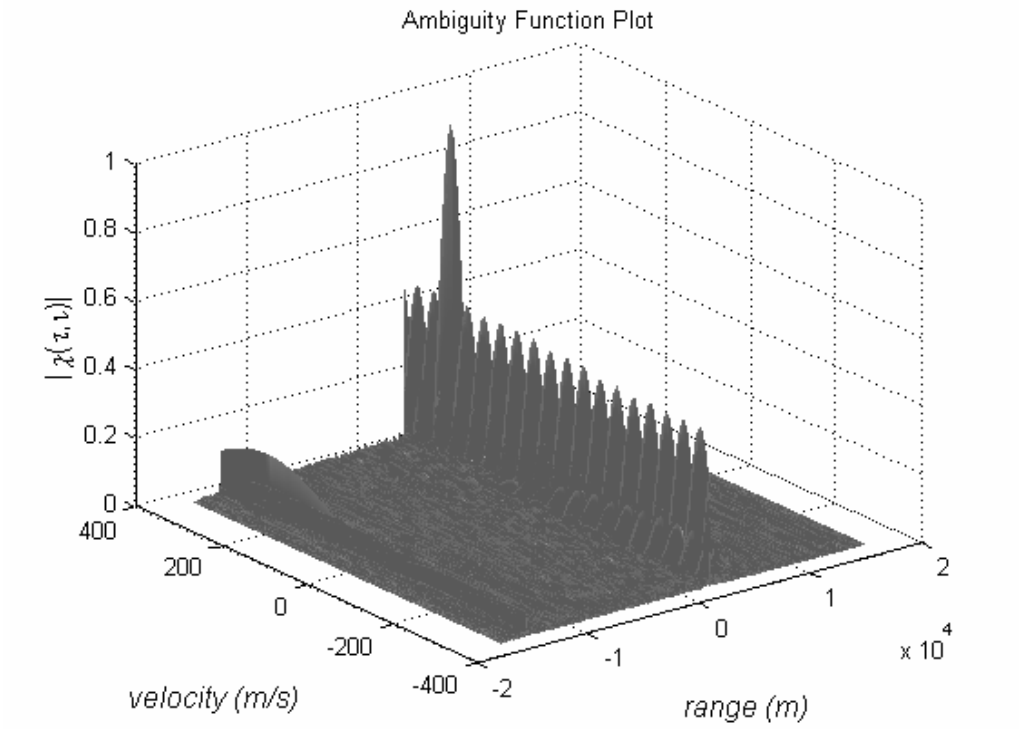

Figure 4.3: 3D Cross - Ambiguity Function plot of the transmitted and received signal for $M = 32$ $(N_c = 1024)$ Frank code. ($R = 2,5$km, $v = 250m/\sec.$)

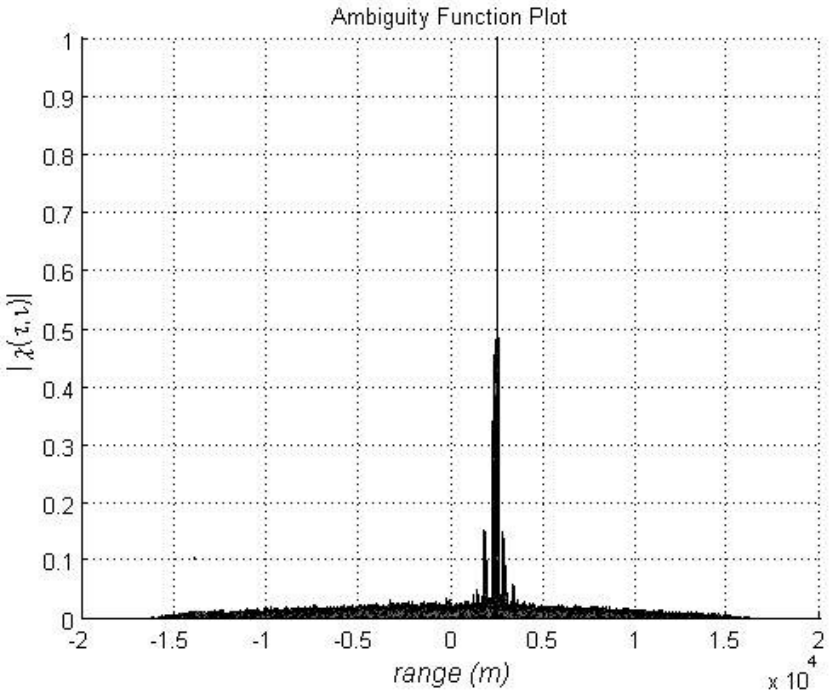

Figure 4.4: Cut along the range axis of Figure 4-3.

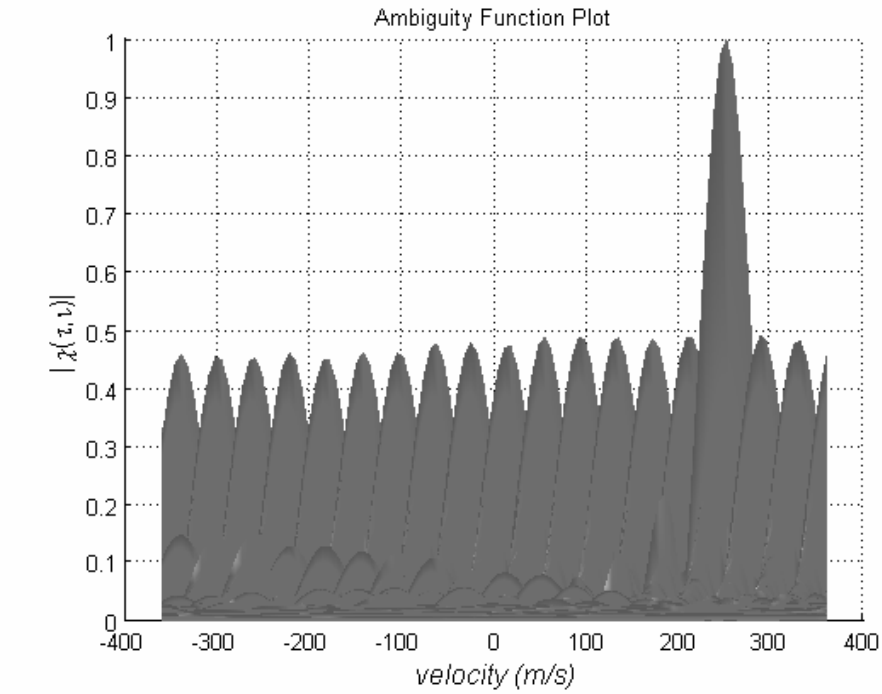

Figure 4.5: Cut along the velocity axis of Figure 4.3.

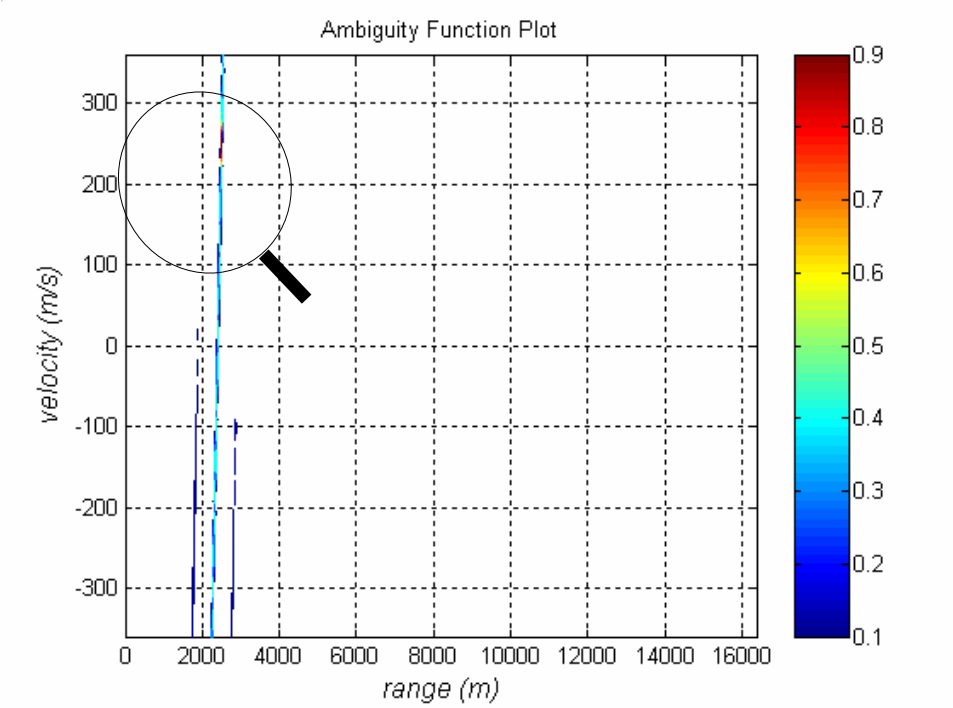

Figure 4.6: 2D Cross - Ambiguity Function plot of the transmitted and received signal for $M = 32$ $(N_c = 1024)$ P1 code. ($R = 2,5$km, $v = 250m/\sec.$)

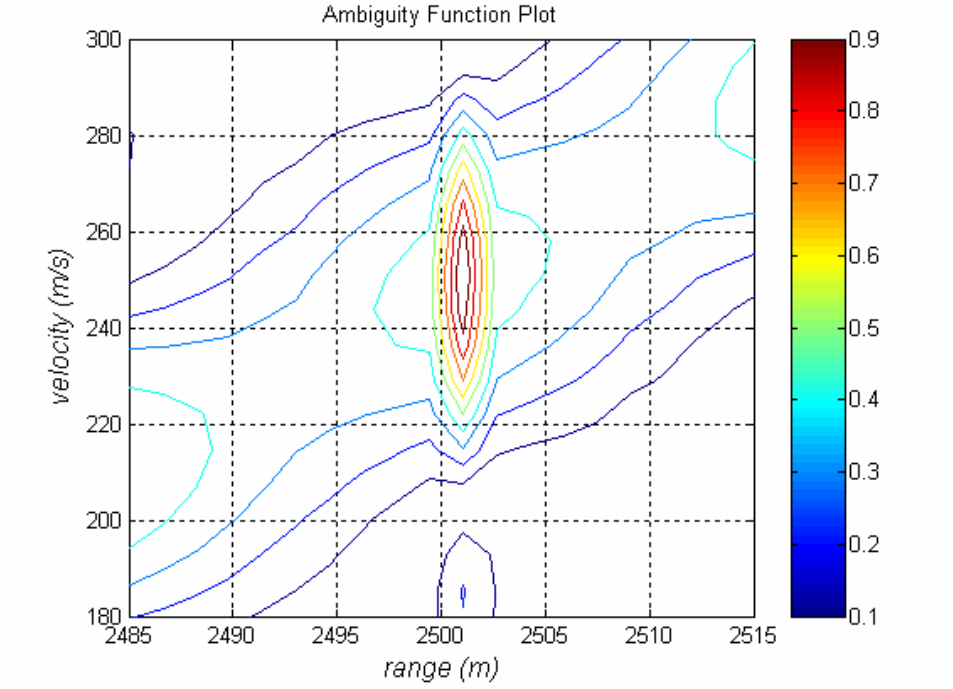

Figure 4.7: Close-up illustration of Figure 4.6

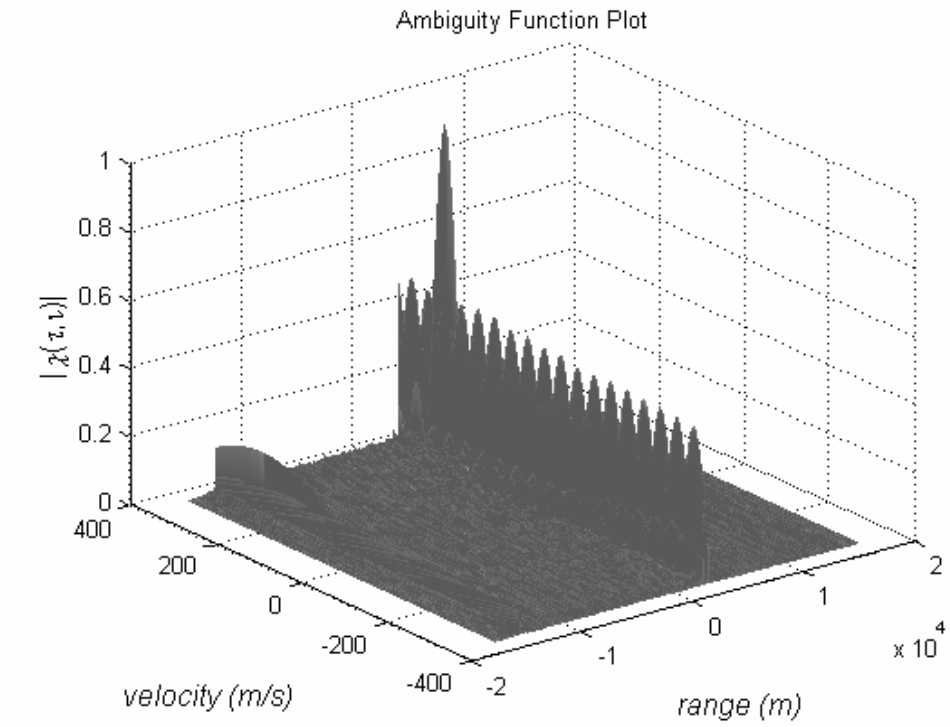

Figure 4.8: 3D Cross - Ambiguity Function plot of the transmitted and received signal for $M = 32$ ($N_c = 1024$) P1 code. ($R = 2,5$km, $\nu = 250m/\sec.$)

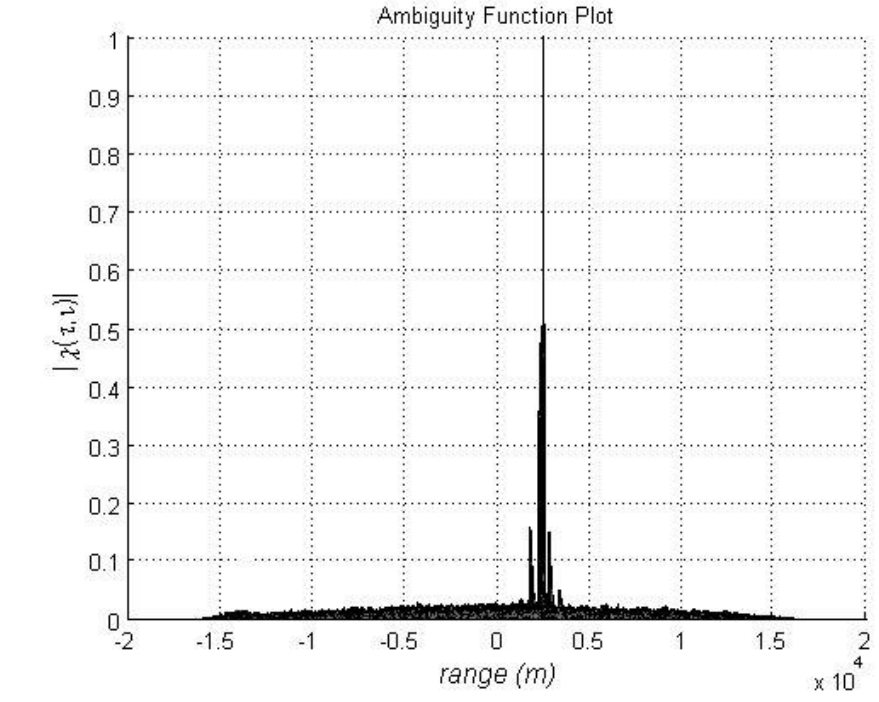

Figure 4.9: Cut along the range axis of Figure 4.8.

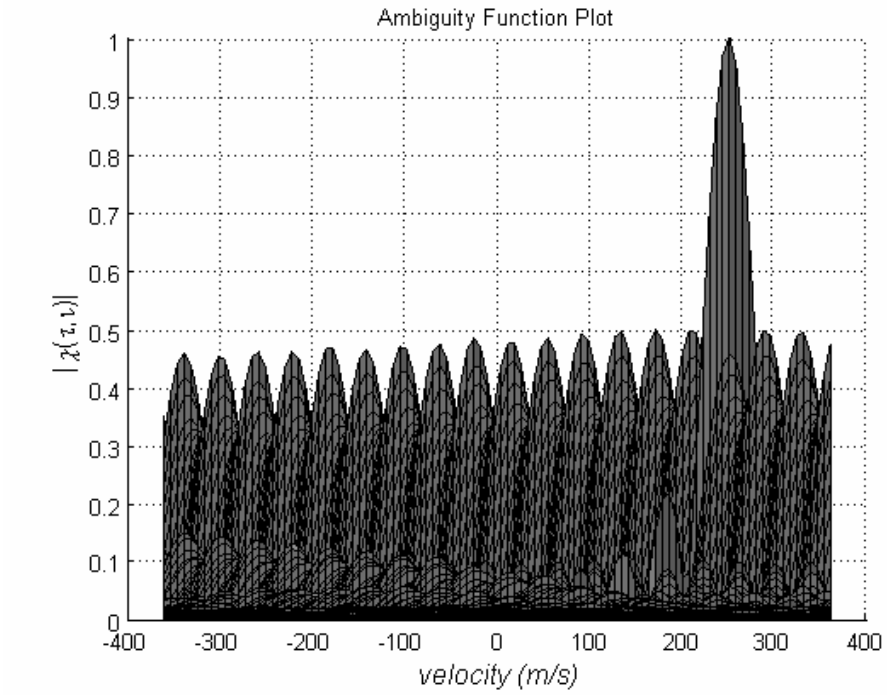

Figure 4.10: Cut along the velocity axis of Figure 4.8.

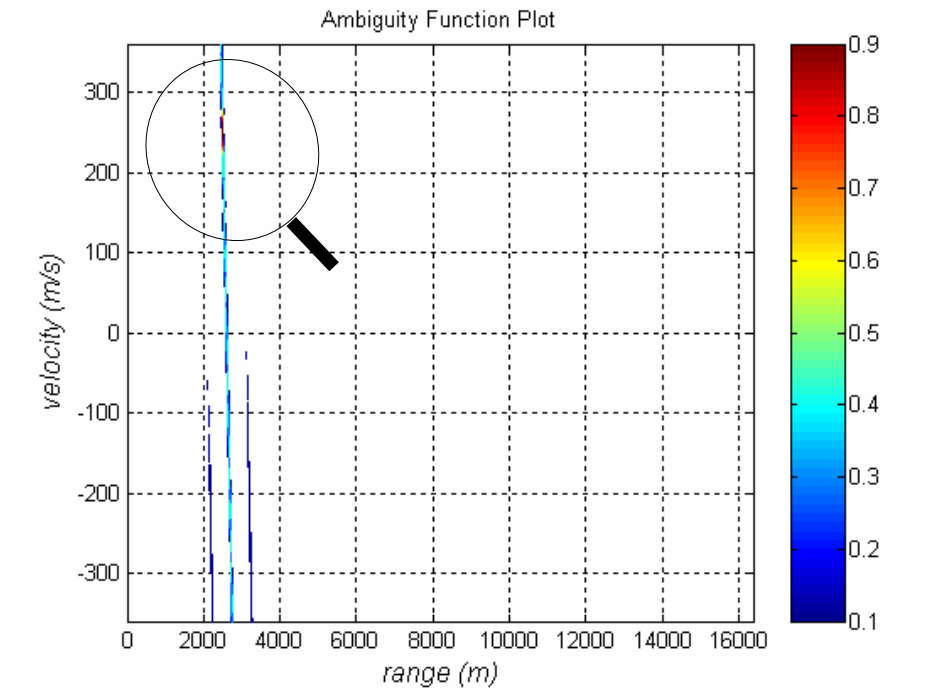

Figure 4.11: 2D Cross - Ambiguity Function plot of the transmitted and received signal for $M = 32$ $(N_c = 1024)$ P2 code. ($R = 2,5$km, $v = 250m/\sec.$)

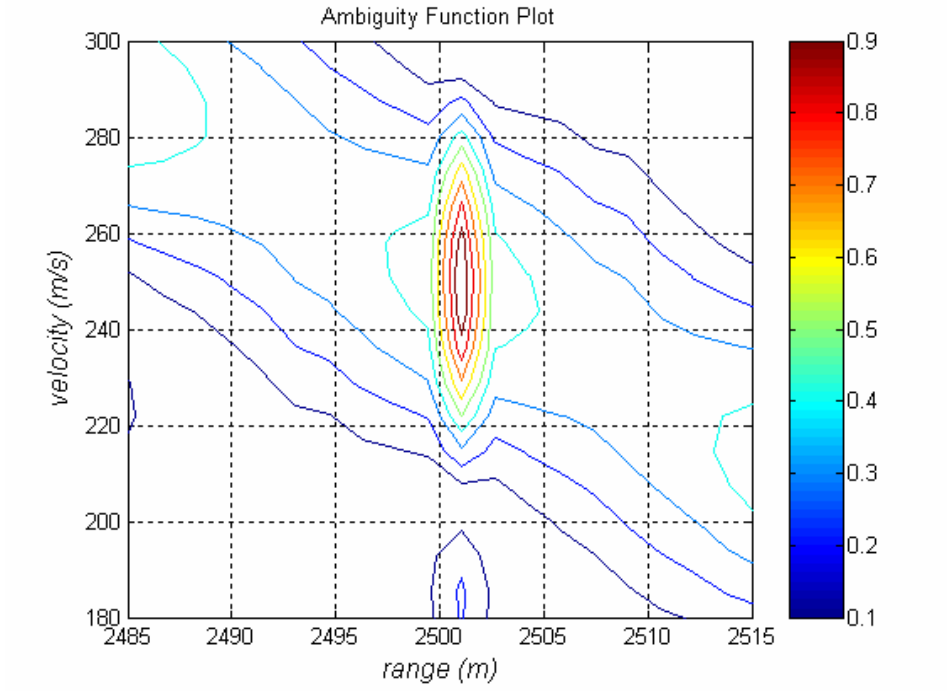

Figure 4.12: Close-up illustration of Figure 4.11

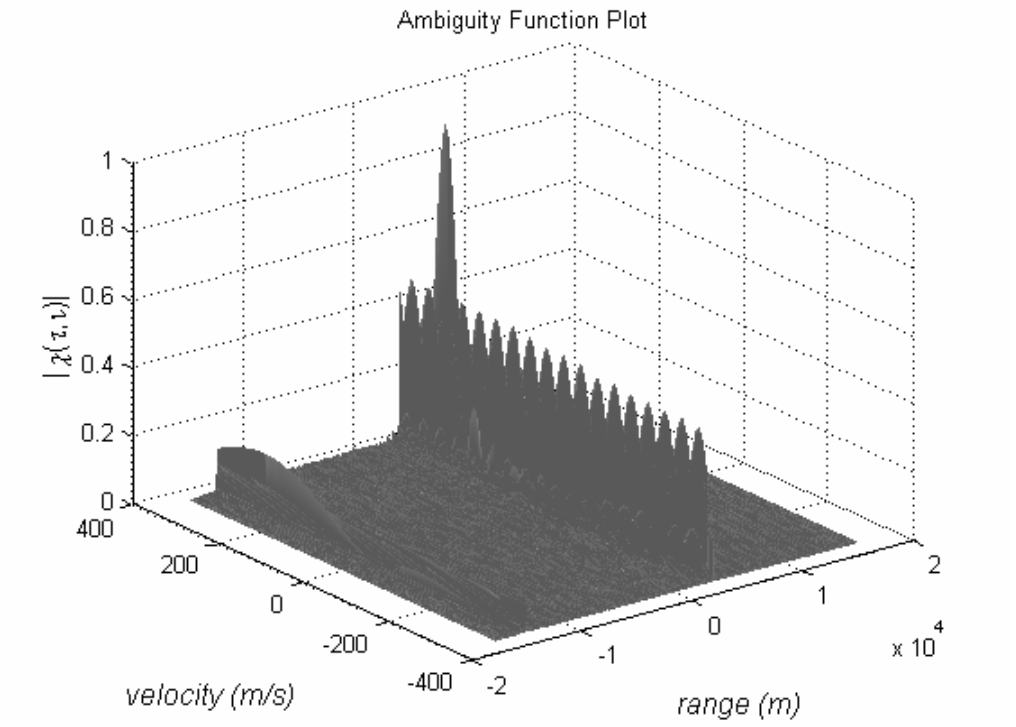

Figure 4.13: 3D Cross - Ambiguity Function plot of the transmitted and received signal for $M = 32$ ($N_c = 1024$) P2 code. ($R = 2,5$km, $v = 250m/\sec.$)

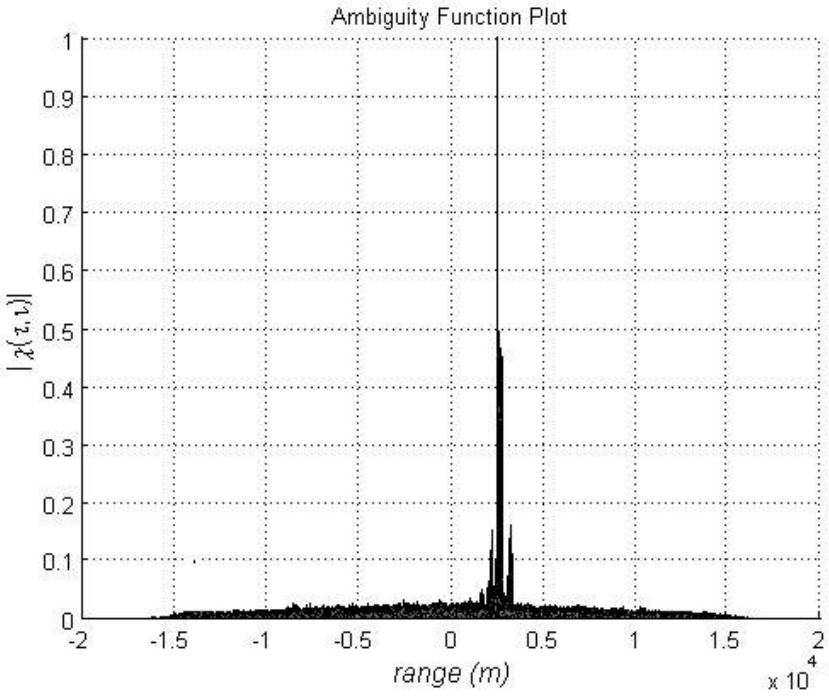

Figure 4.14: Cut along the range axis of Figure 4.13.

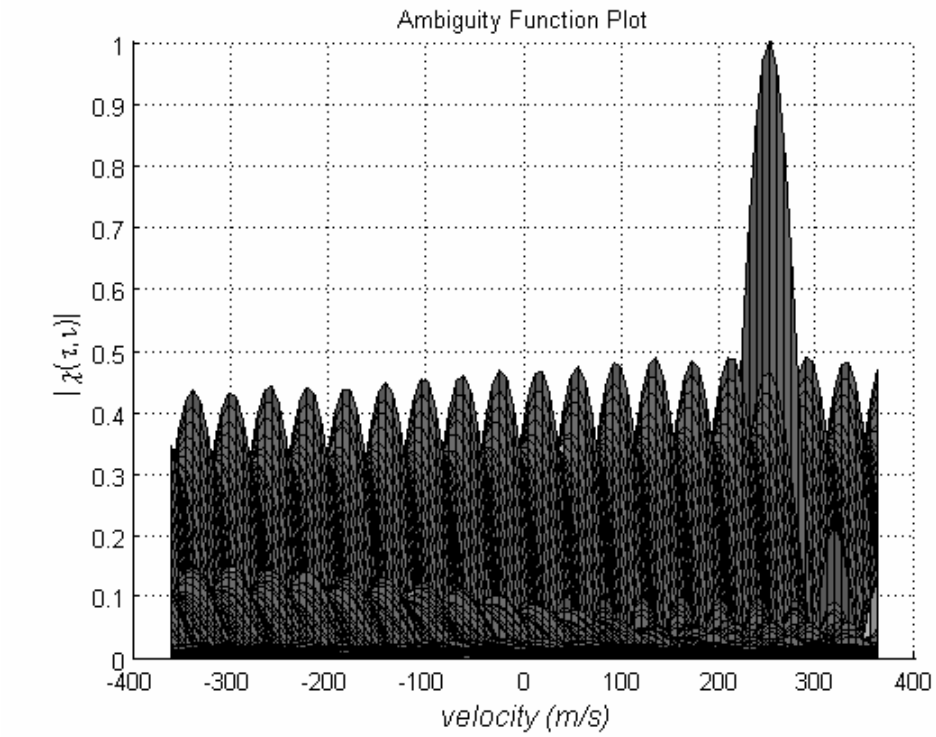

Figure 4.15: Cut along the velocity axis of Figure 4.13.

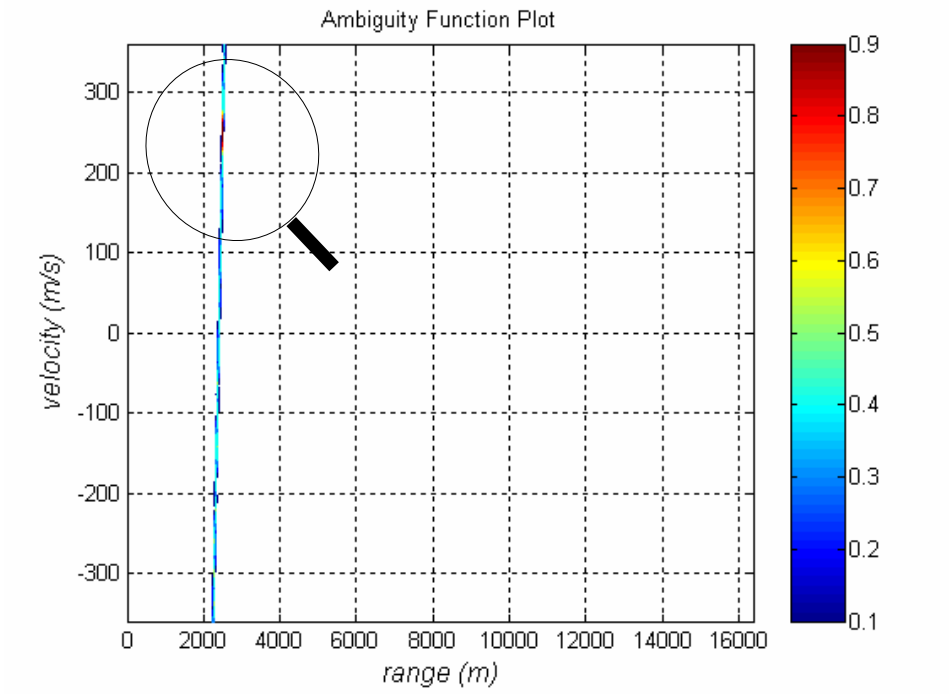

Figure 4.16: 2D Cross - Ambiguity Function plot of the transmitted and received signal for $M = 1024$ ($N_c = 1024$) P3 code. ($R = 2{,}5\text{km}$, $v = 250 m/\sec.$)

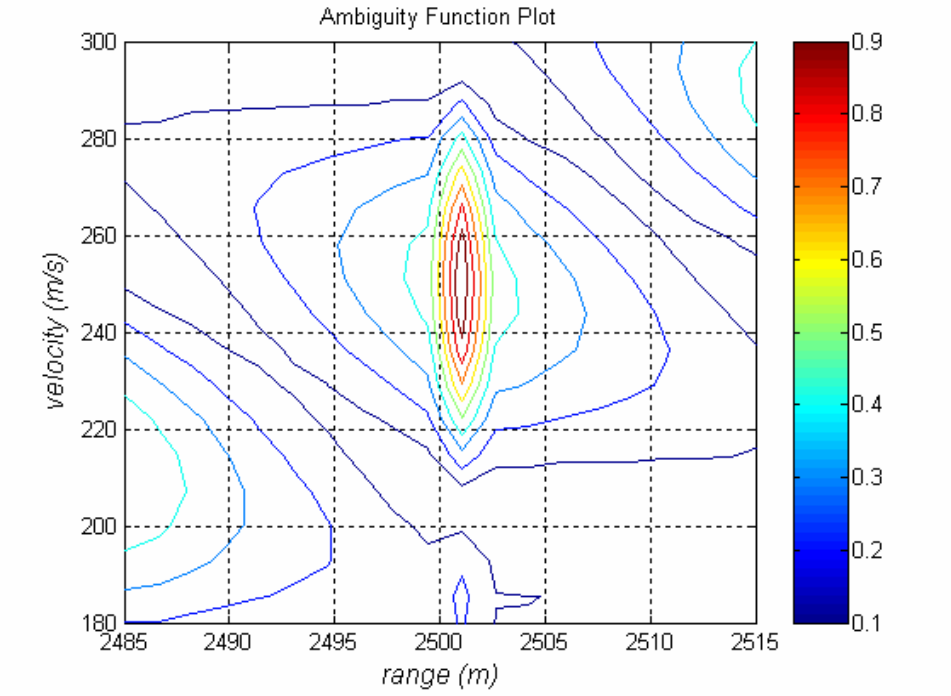

Figure 4.17: Close-up illustration of Figure 4.16.

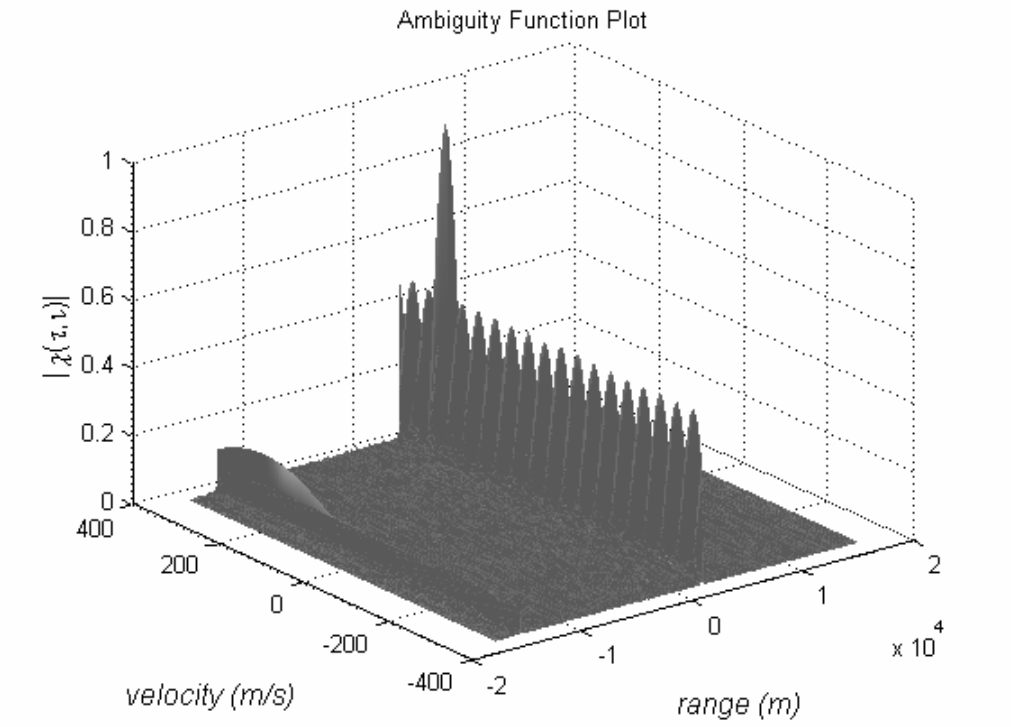

Figure 4.18: 3D Cross - Ambiguity Function plot of the transmitted and received signal for $M = 1024$ ($N_c = 1024$) P3 code. ($R = 2{,}5\text{km}$, $v = 250 m/\sec.$)

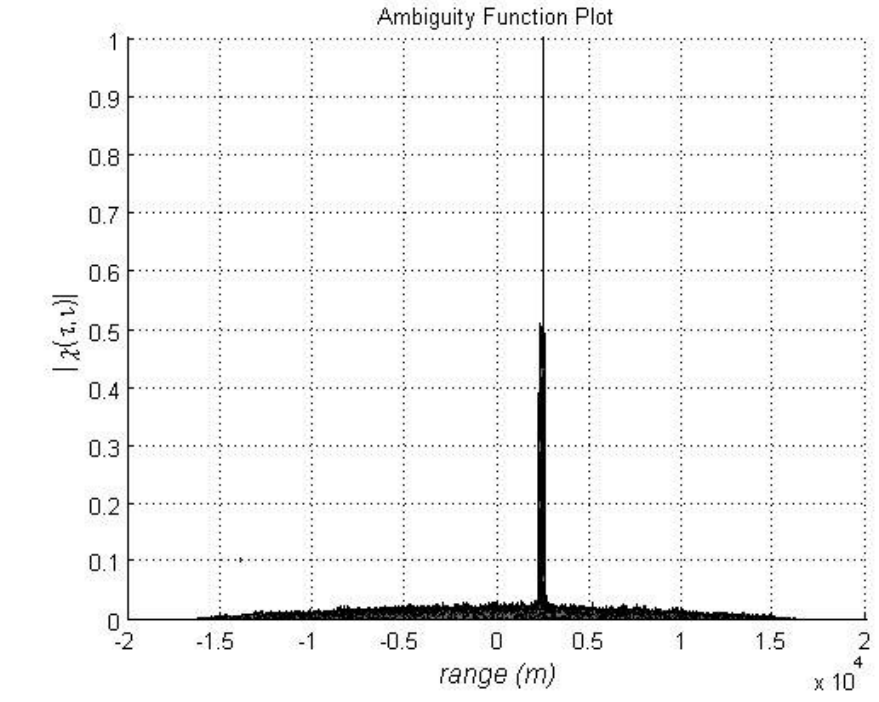

Figure 4.19: Cut along the range axis of Figure 4.18.

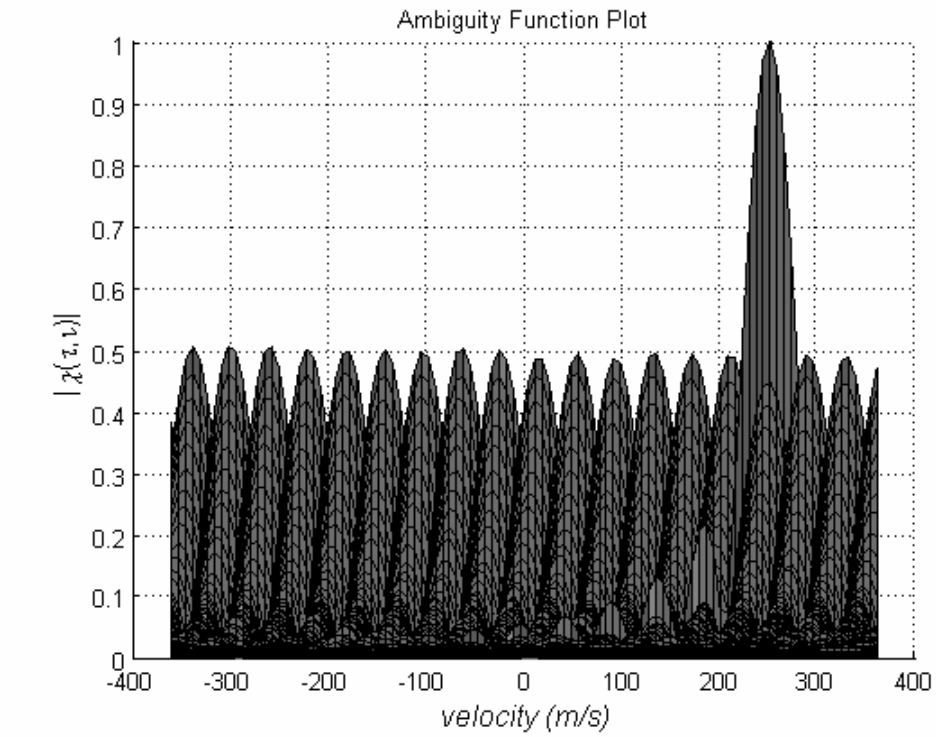

Figure 4.20: Cut along the velocity axis of Figure 4.18.

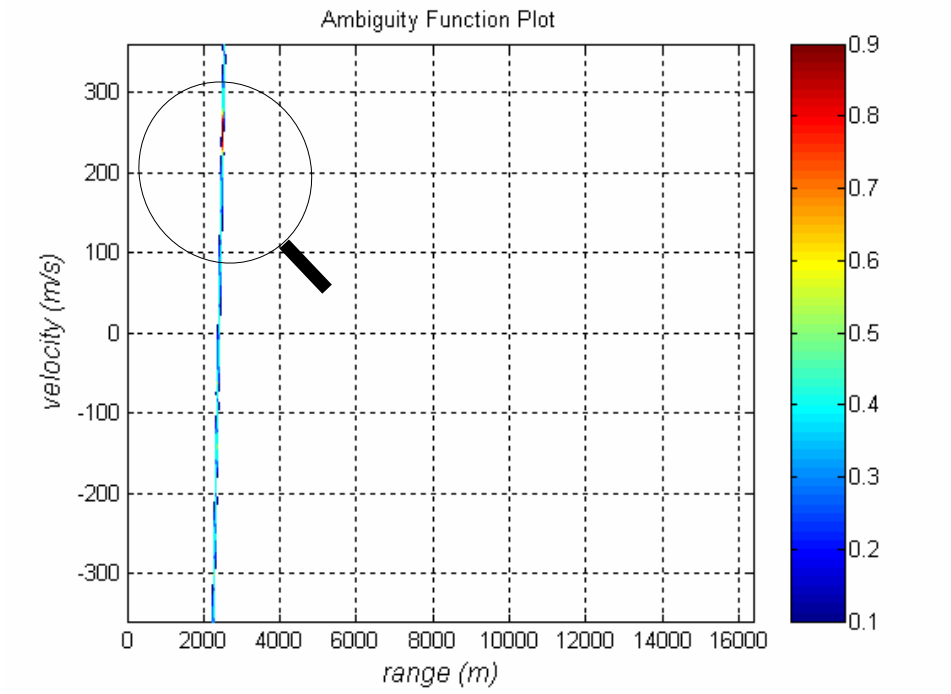

Figure 4.21: 2D Cross - Ambiguity Function plot of the transmitted and received signal for $M = 1024$ ($N_c = 1024$) P4 code. ($R = 2{,}5\text{km}$, $v = 250 m/\sec.$)

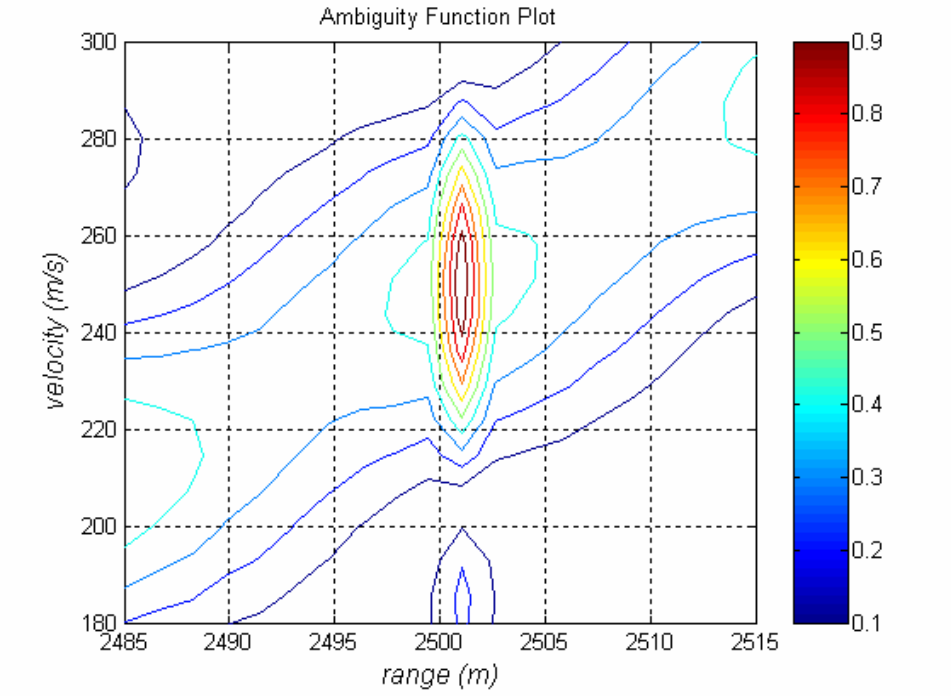

Figure 4.22: Close-up illustration of Figure 4.21.

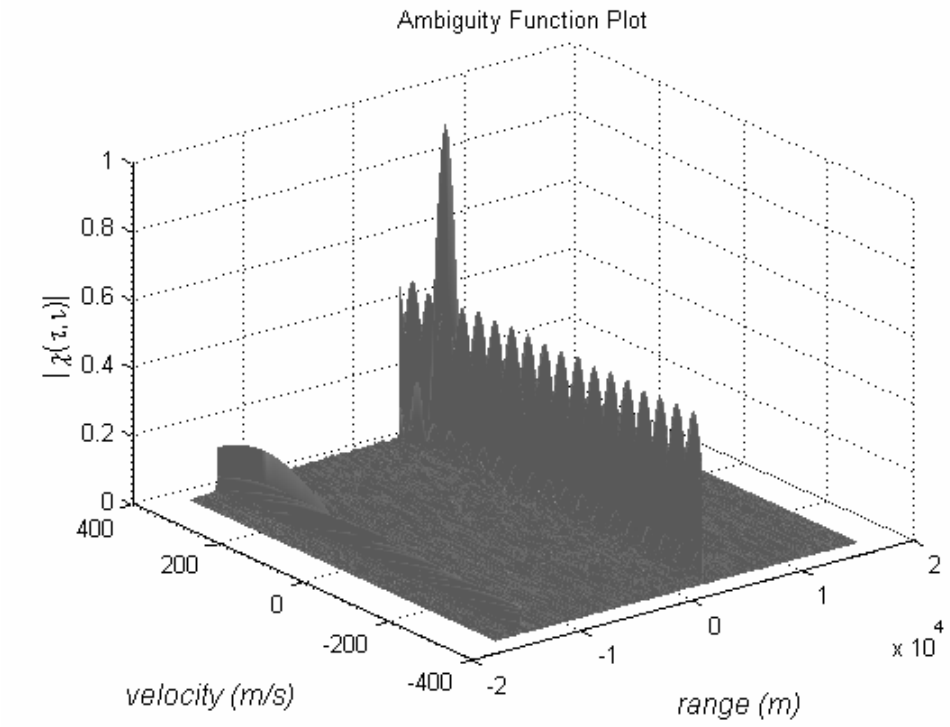

Figure 4.23: 3D Cross - Ambiguity Function plot of the transmitted and received signal for $M = 1024$ ($N_c = 1024$) P4 code. ($R = 2{,}5\text{km}$, $v = 250 m/\sec.$)

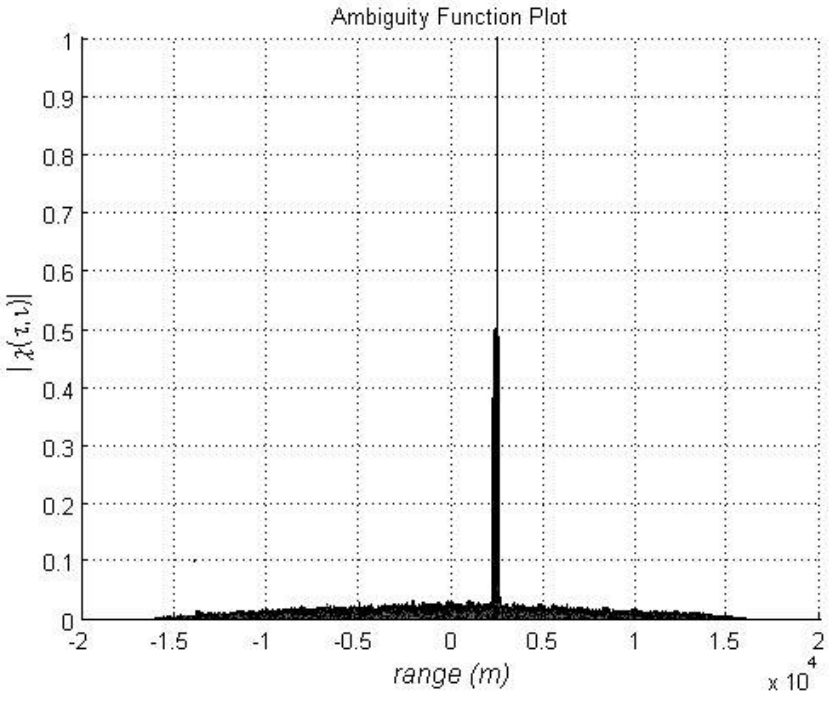

Figure 4.24: Cut along the range axis of Figure 4.23.

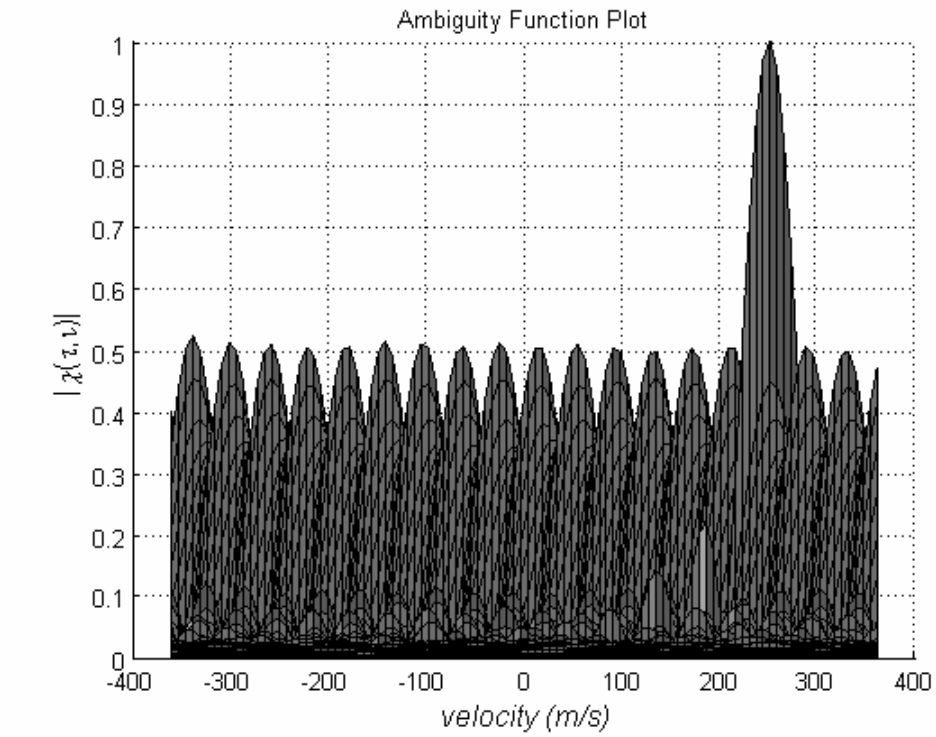

Figure 4.25: Cut along the velocity axis of Figure 4.23.

4.2.2 Scenario 2: Target at a longer range.

At this scenario there is one target which is 14000 meter away from the radar having 50 m/sec. radial velocity with respect to the radar, i.e. $R = 14000$ m and $v_r = 50$ m/sec.

The transmitted CW signal is coded by using the Frank, P1, P2, P3, and P4 coding types with $N_c = 1024$. The resulting cross-contour plots for the ambiguity function of the transmitted and received radar signal are given in Figure 4.26, Figure 4.28, Figure 4.30, Figure 4.32, and Figure 4.34. The portion of the plot around the peak point for all coding types is enlarged in Figure 4.27, Figure 4.29, Figure 4.31, Figure 4.33, and Figure 4.35 to examine the details for range resolution and Doppler resolution. It is observed on these figures that the target is detected at about $R = 14001$ m. with $v_r = 46$ m/sec. The percentage errors in range and radial velocity are calculated at below.

$$\varepsilon_{range} = \frac{|14001 - 14000|}{14000} \times 100 = 0,0071\,\%$$

$$\varepsilon_{velocity} = \frac{|46 - 50|}{50} \times 100 = 8\,\%$$

Note that, velocity error is increase dramatically, when target range is increased from 2500 meters to 14000 meters. On the other hand, range error is decrease when target range is increased.

Based upon the simulation results displayed in Fig. 4.26 through 4.35 it is concluded that the values of the detected range and radial velocity remain the same. For all coding types, the measurement precision in range and radial velocity of the target are the same which is an expected result. This is because, range resolution is related to c (light velocity) and t_b (subcode period), Doppler resolution is related to N (number of the code period), N_c (number of subcodes), and t_b. All of these variables are selected to be the same for all the code types for easy comparison.

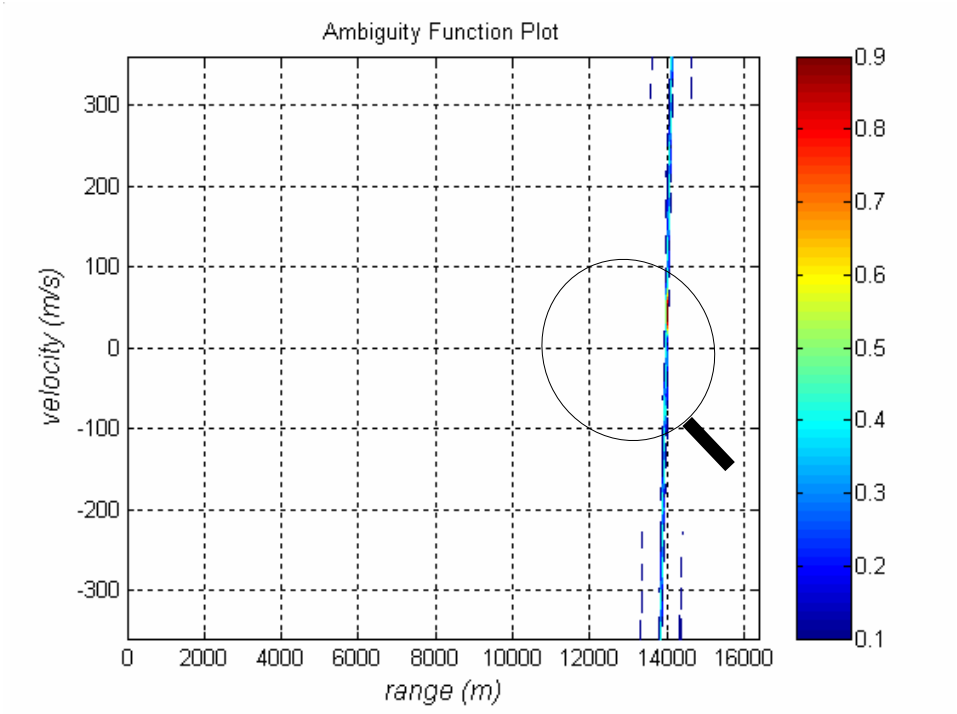

Figure 4.26: 2D Cross - Ambiguity Function plot of the transmitted and received signal for $M = 32$ $(N_c = 1024)$ Frank code. ($R = 14$km, $v = 50m/\sec.$)

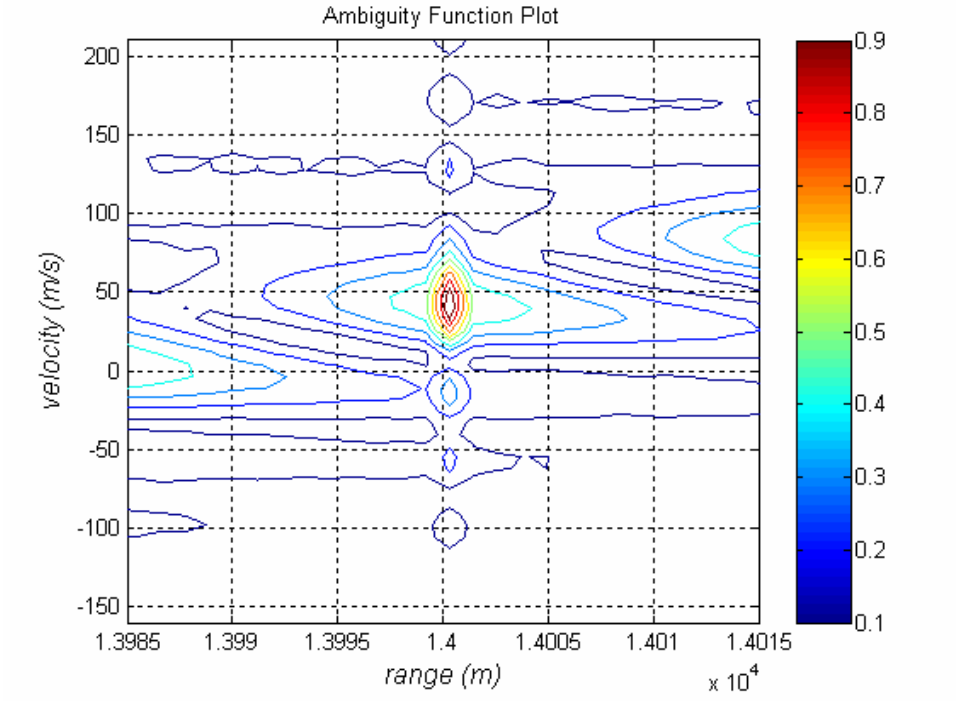

Figure 4.27: Close-up illustration of Figure 4.26.

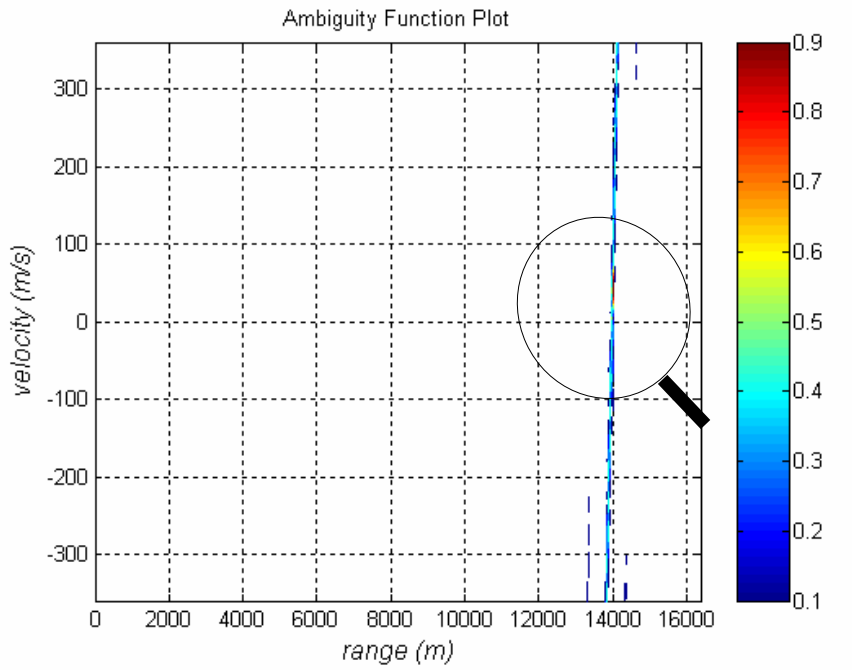

Figure 4.28: 2D Cross - Ambiguity Function plot of the transmitted and received signal for $M = 32$ ($N_c = 1024$) P1 code. ($R = 14$km, $v = 50m/\sec.$)

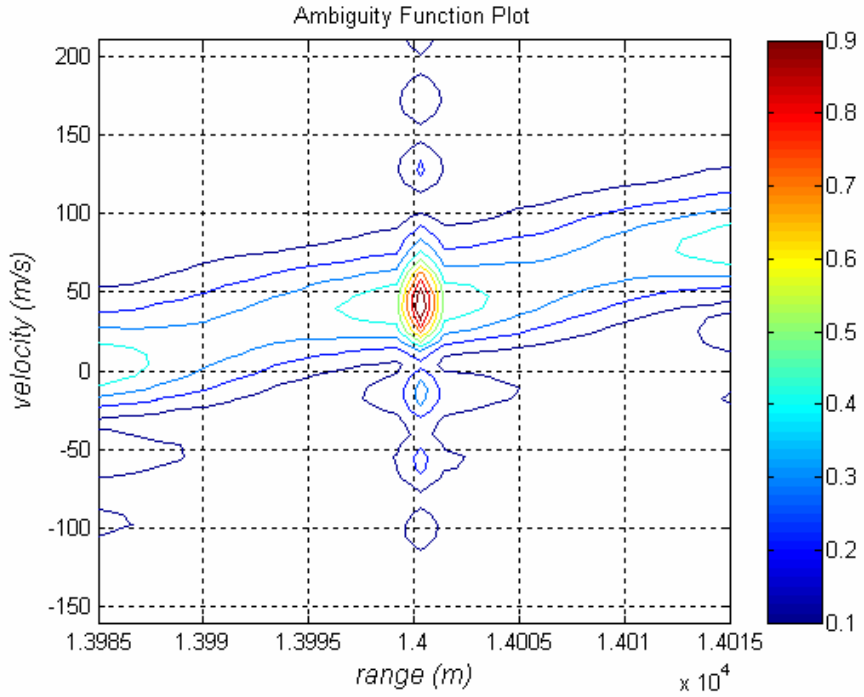

Figure 4.29: Close-up illustration of Figure 4.28.

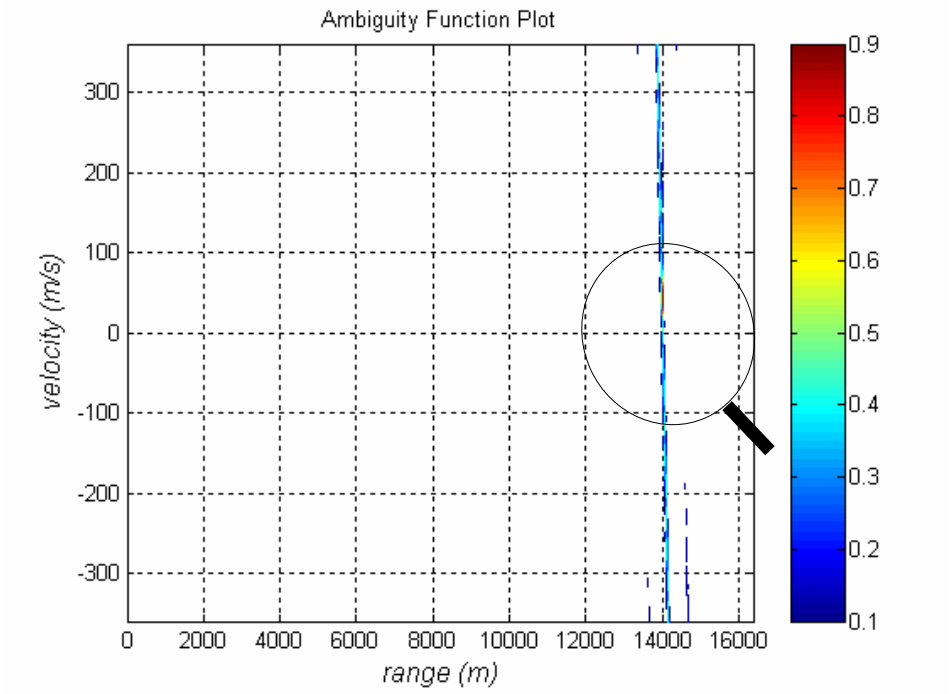

Figure 4.30: 2D Cross - Ambiguity Function plot of the transmitted and received signal for $M = 32$ $(N_c = 1024)$ P2 code. ($R = 14$km, $v = 50m/\sec.$)

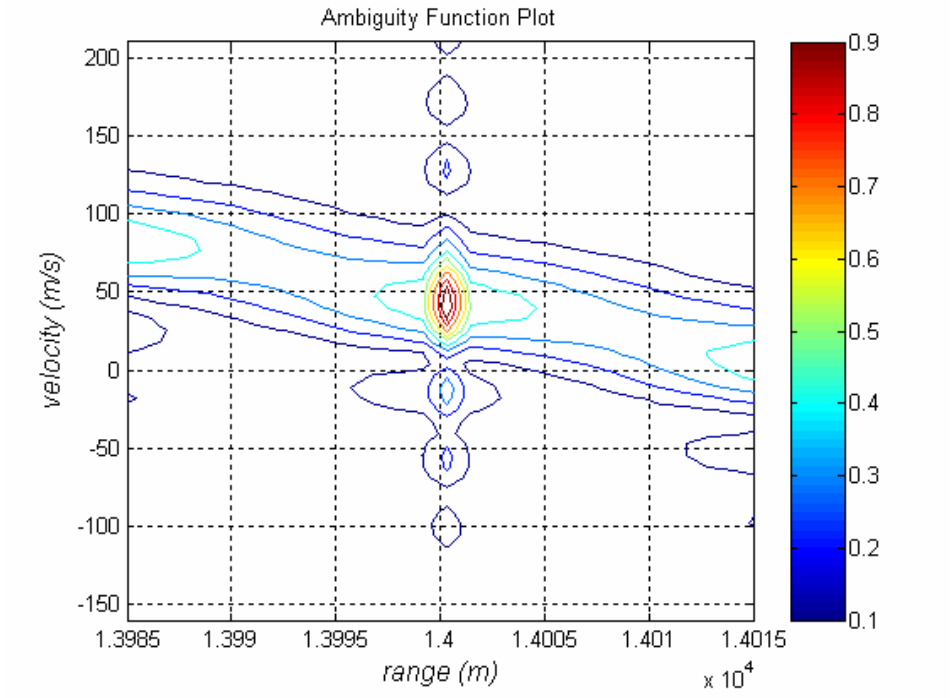

Figure 4.31: Close-up illustration of Figure 4.30.

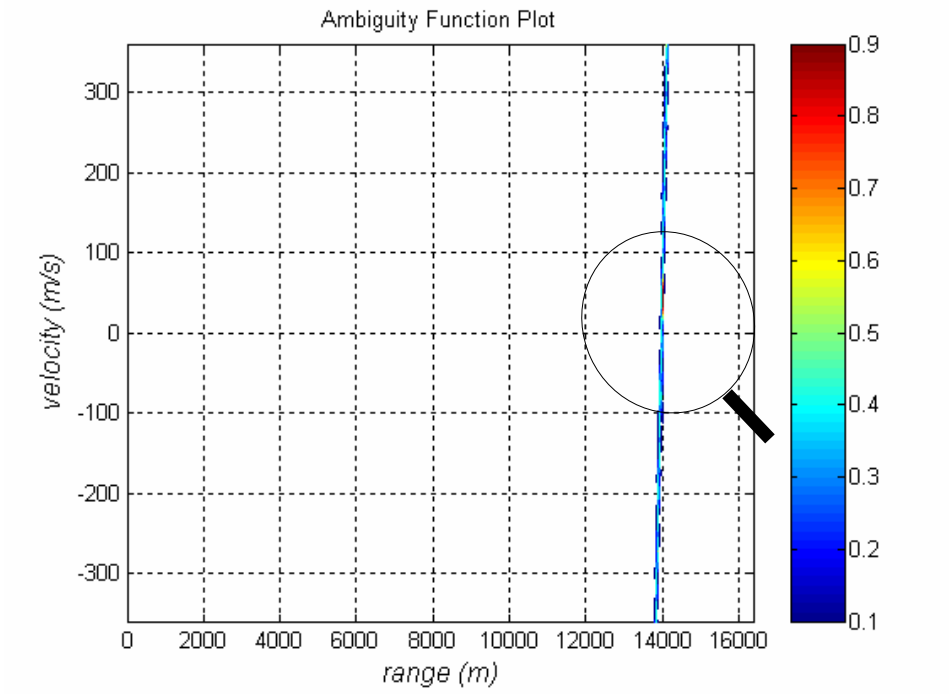

Figure 4.32: 2D Cross - Ambiguity Function plot of the transmitted and received signal for $M = 1024$ ($N_c = 1024$) P3 code. ($R = 14$km, $v = 50m/\sec.$)

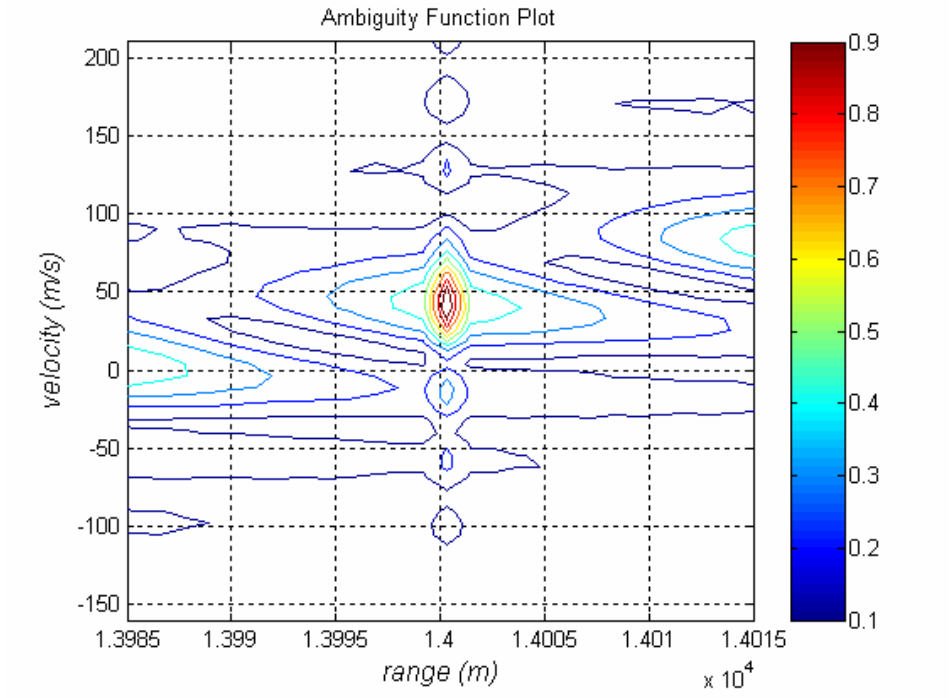

Figure 4.33: Close-up illustration of Figure 4.32.

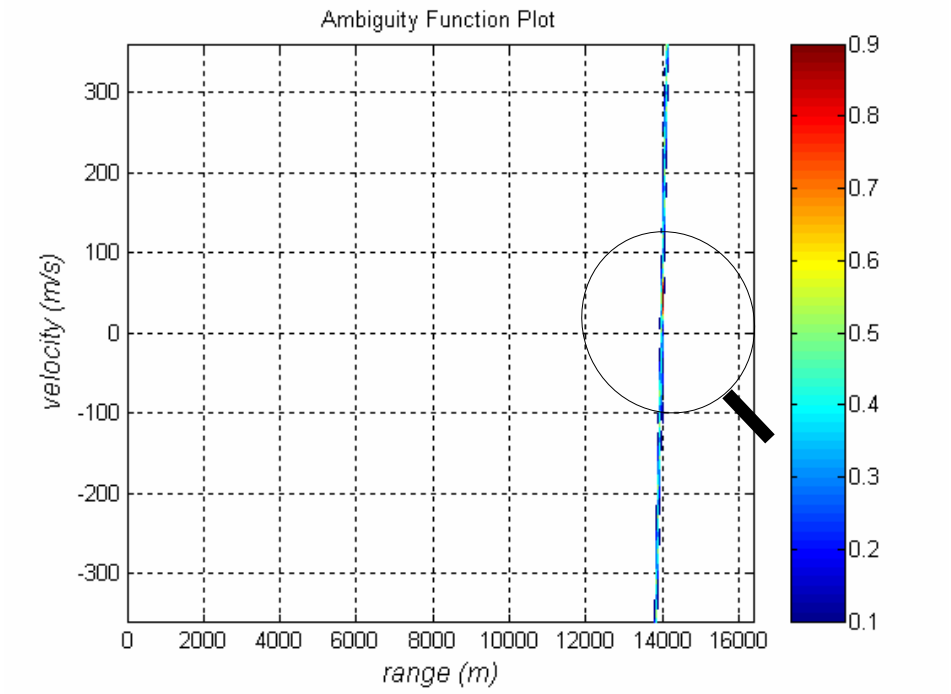

Figure 4.34: 2D Cross - Ambiguity Function plot of the transmitted and received signal for $M = 1024$ ($N_c = 1024$) P4 code. ($R = 14$km, $v = 50m/\sec.$)

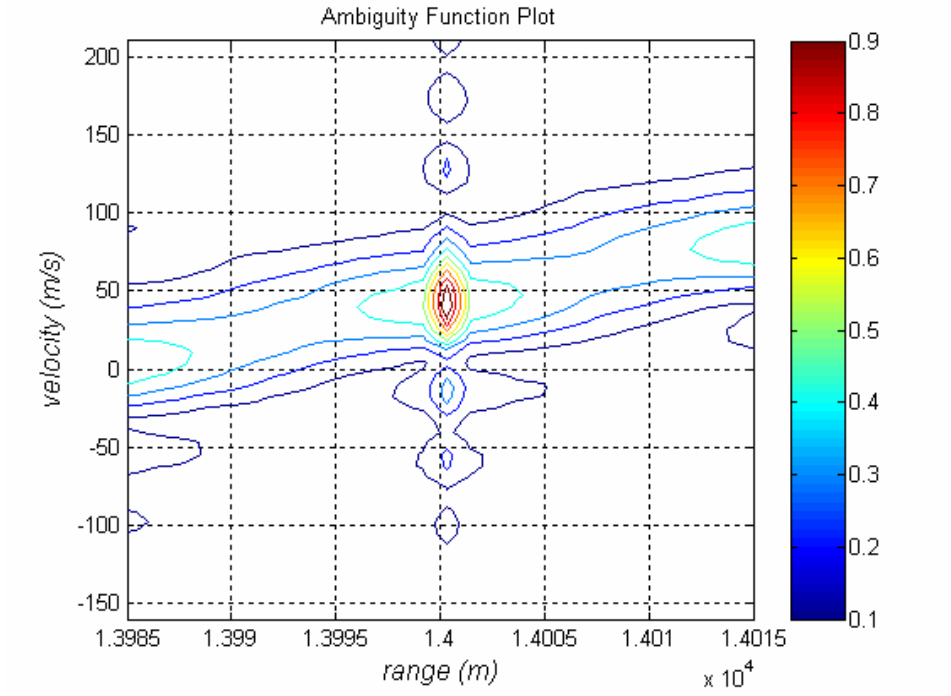

Figure 4.35: Close-up illustration of Figure 4.34.

4.3 A Multiple Target Scenario

At this target scenario, there are three targets which are 1000, 1500, 2000 meter away from the radar, respectively. Targets have 200, 150, 250 m/sec. radial velocity with respect to the radar. In other words, $R_1 = 1$ km, $R_2 = 2$ km, $R_3 = 2.5$ km with $v_1 = 200$ m/sec, $v_2 = 150$ m/sec, and $v_3 = 250$ m/sec. in this target detection scenario.

The transmitted CW signal is coded by using the Frank, P1, P2, P3, and P4 coding types with $N_c = 1024$ respectively. The resulting cross-contour plots for the ambiguity function of the transmitted and received radar signal are given in Figure 4.36, Figure 4.38, Figure 4.40, Figure 4.42, and Figure 4.44. The portion of the plot around the peak point for all coding types is enlarged in Figure 4.37, Figure 4.39, Figure 4.41, Figure 4.43, and Figure 4.45 to examine the details for range resolution and Doppler resolution. It is observed on these figures that the targets are detected at about $R_1 = 1000.1$ m. with $v_1 = 200$ m/sec., $R_2 = 1500.95$ m, $v_2 = 149.1$ m/sec. $R_2 = 2000.2$ m, $v_3 = 250.9$ m/sec. Targets are detected same positions for all coding types. The percentage errors in range and radial velocity are calculated at below.

$$\varepsilon_{range1} = \frac{|1000,1 - 1000|}{1000} \times 100 = 0,01\,\%$$

$$\varepsilon_{range2} = \frac{|1500,95 - 1500|}{1500} \times 100 = 0,0633\,\%$$

$$\varepsilon_{range3} = \frac{|2000,2 - 2000|}{2000} \times 100 = 0,01\,\%$$

$$\varepsilon_{velocity1} = \frac{|200 - 200|}{200} \times 100 = 0\,\%$$

$$\varepsilon_{velocity2} = \frac{|149,1 - 150|}{150} \times 100 = 0,6\,\%$$

$$\varepsilon_{velocity3} = \frac{|250.9 - 250|}{250} \times 100 = 0,36\,\%$$

Based upon the simulation results displayed in Figures 4.36 through 4.45 it is concluded that the values of the detected range and radial velocity remain the same. For all coding types, the measurement precision in range and radial velocity of the target are the same which is an expected result. This is because, range resolution is related to c (light velocity) and t_b (subcode period), Doppler resolution is related to N (number of the code period), N_c (number of subcodes), and t_b (subcode period). All of these variables are selected to be the same for all the code types for easy comparison purposes.

The three-dimensional AF (Ambiguity Function) plot for Frank code is also given in Figure 4.46 to see the levels of side lobes. Side lobe level and resolution information are further displayed in 4.47 and 4.48 where the cross-sections of the 3D AF plots are given along range axis and velocity axis, respectively. As seen in Figure 4.47 and 4.48, the side lobes of the AF plot are lower than 45% of the normalized peak magnitude of one at the largest point. That is, the side lobe levels increase 5% for multiple targets (three targets) scenarios with respect to single target scenario.

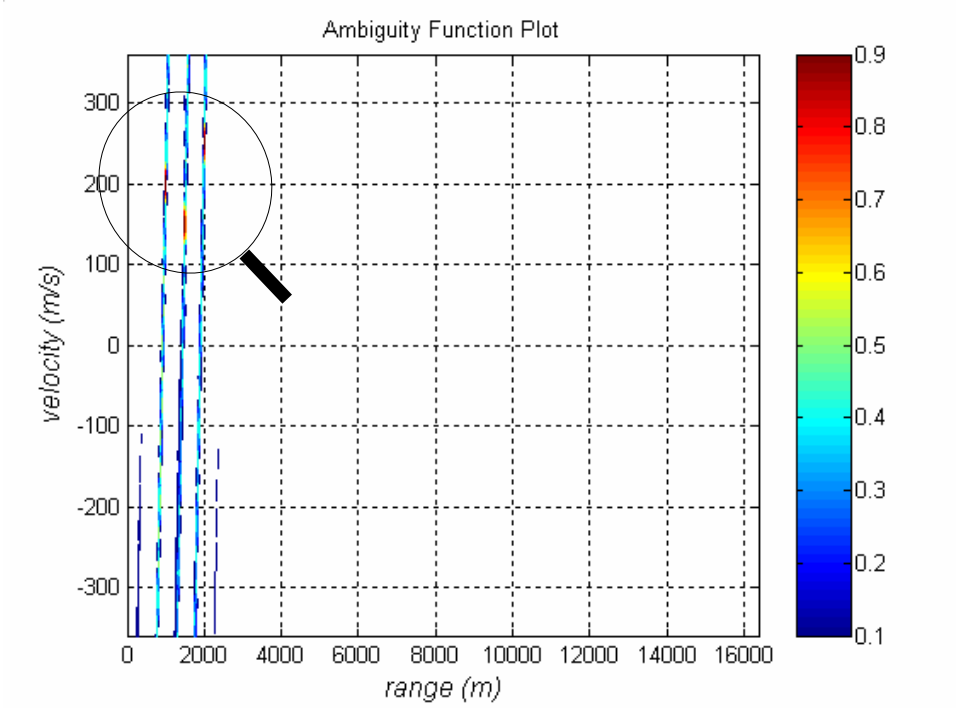

Figure 4.36: 2D Cross - Ambiguity Function plot of the transmitted and received signal for $M = 32$ $(N_c = 1024)$ Frank code $\left(R_1 = 1km, R_2 = 1.5km, R_3 = 2km, v_1 = 200m/\sec, v_1 = 150m/\sec, v_1 = 250m/\sec\right)$.

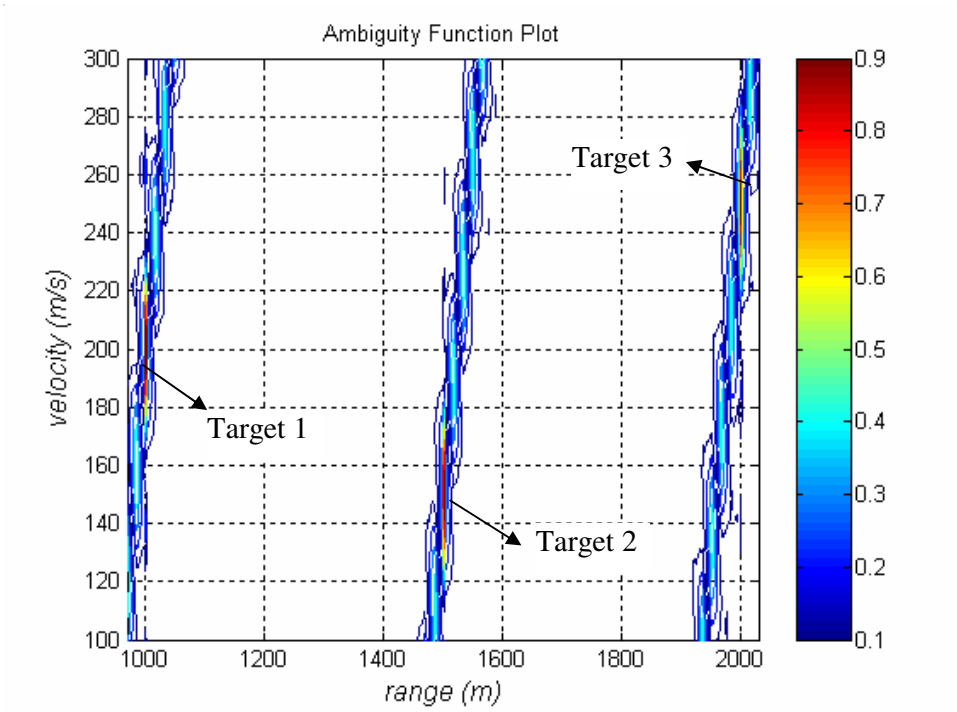

Figure 4.37: Close-up illustration of Figure 4.36.

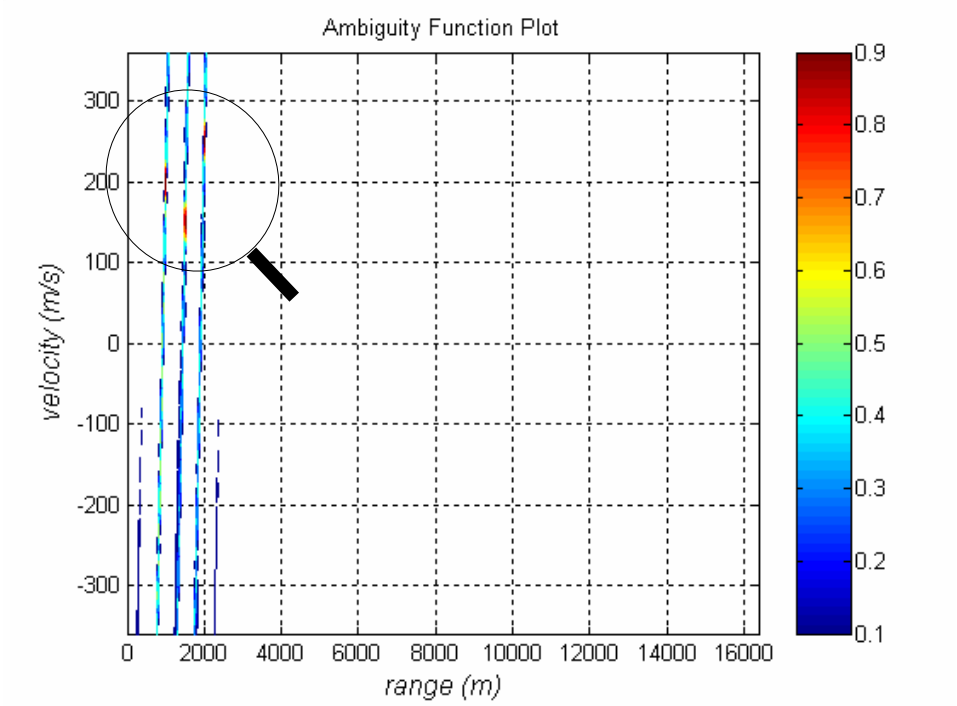

Figure 4.38: 2D Cross - Ambiguity Function plot of the transmitted and received signal for $M = 32$ $(N_c = 1024)$ P1 code

$\left(R_1 = 1km, R_2 = 1.5km, R_3 = 2km, v_1 = 200m/\sec, v_1 = 150m/\sec, v_1 = 250m/\sec\right)$

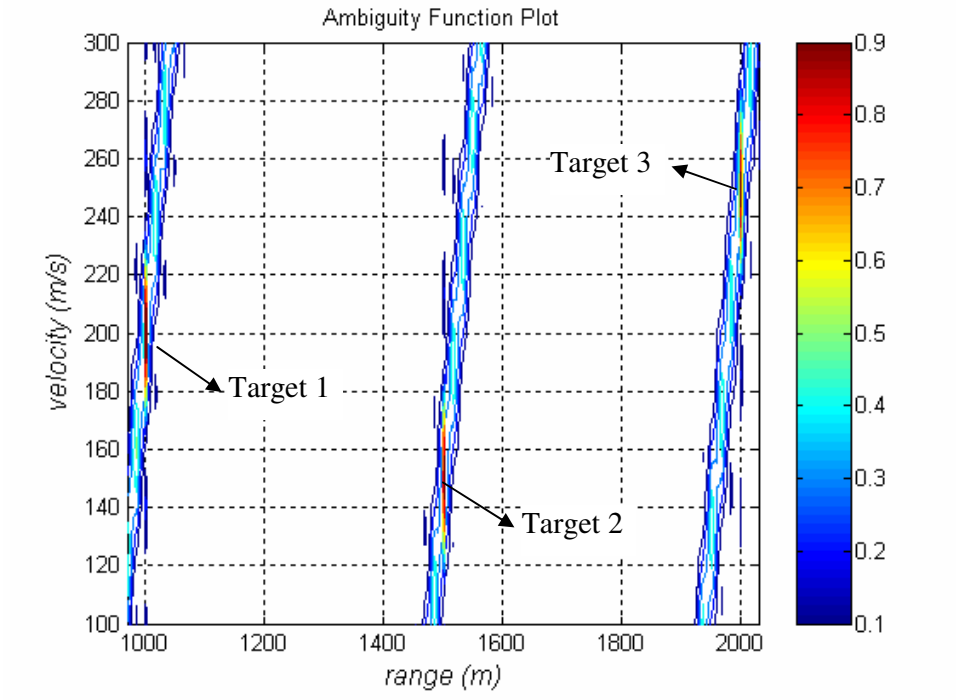

Figure 4.39: Close-up illustration of Figure 4.38.

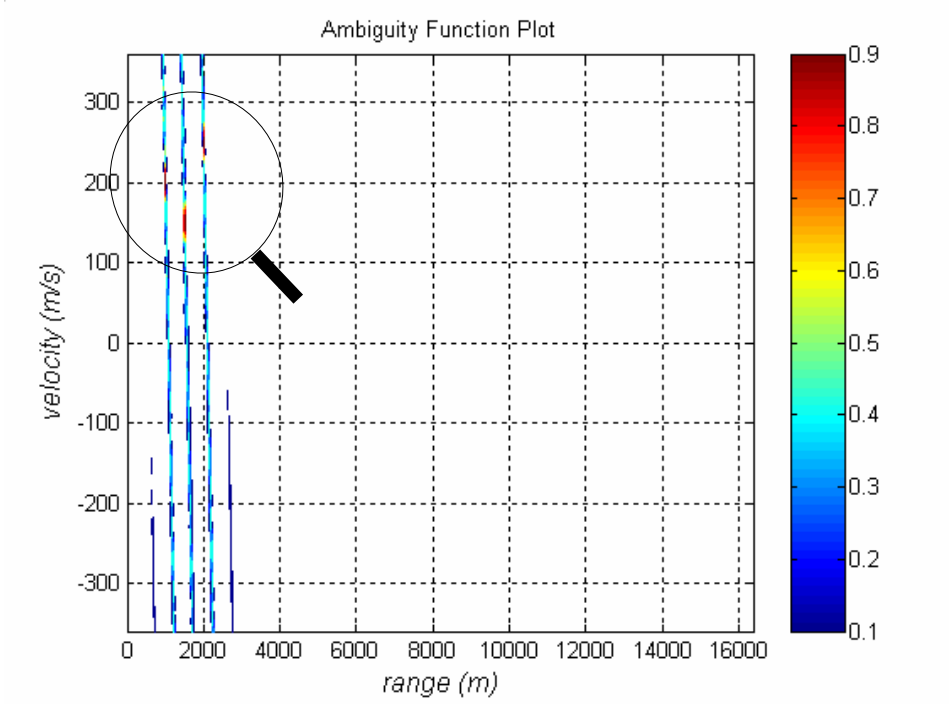

Figure 4.40: 2D Cross - Ambiguity Function plot of the transmitted and received signal for $M = 32$ $(N_c = 1024)$ P2 code $\left(R_1 = 1km, R_2 = 1.5km, R_3 = 2km, v_1 = 200m/\sec, v_1 = 150m/\sec, v_1 = 250m/\sec\right)$.

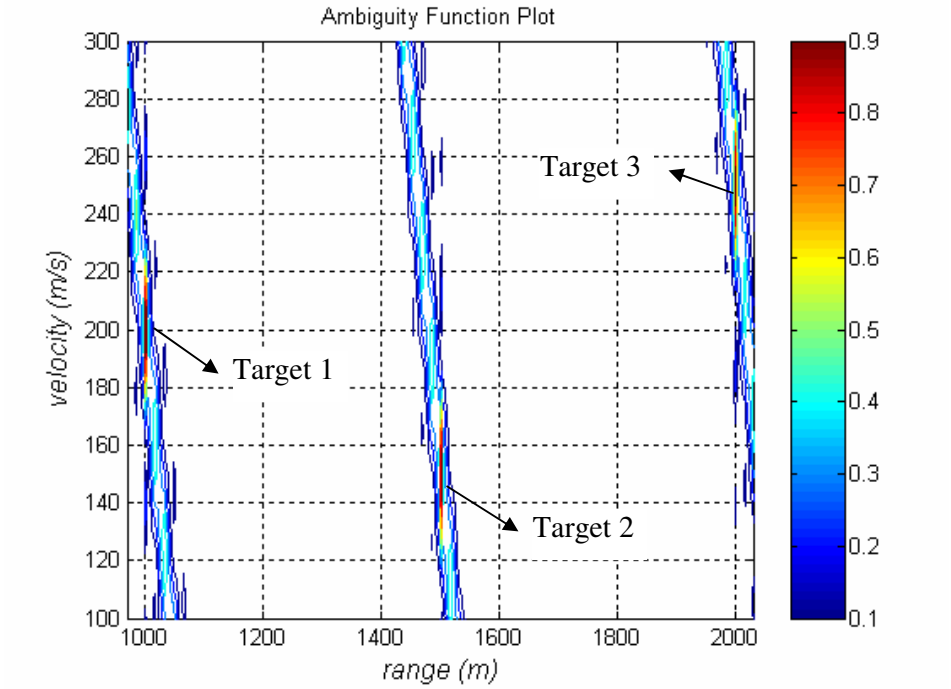

Figure 4.41: Close-up illustration of Figure 4.40.

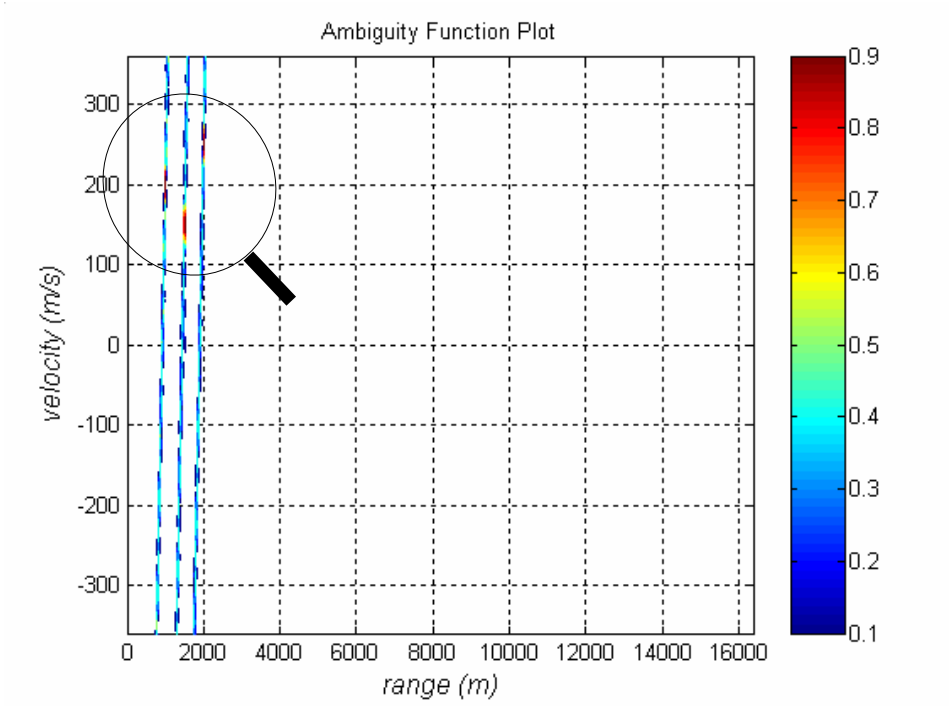

Figure 4.42: 2D Cross - Ambiguity Function plot of the transmitted and received signal for $M = 1024$ $(N_c = 1024)$ P3 code $\left(R_1 = 1km, R_2 = 1.5km, R_3 = 2km, v_1 = 200m/\sec, v_1 = 150m/\sec, v_1 = 250m/\sec\right)$.

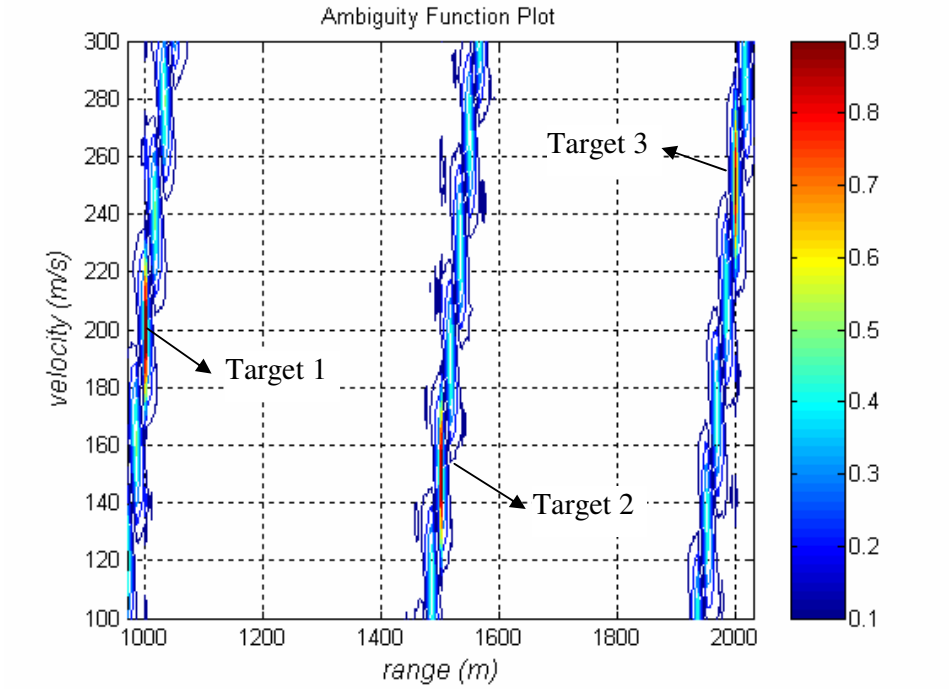

Figure 4.43: Close-up illustration of Figure 4.42.

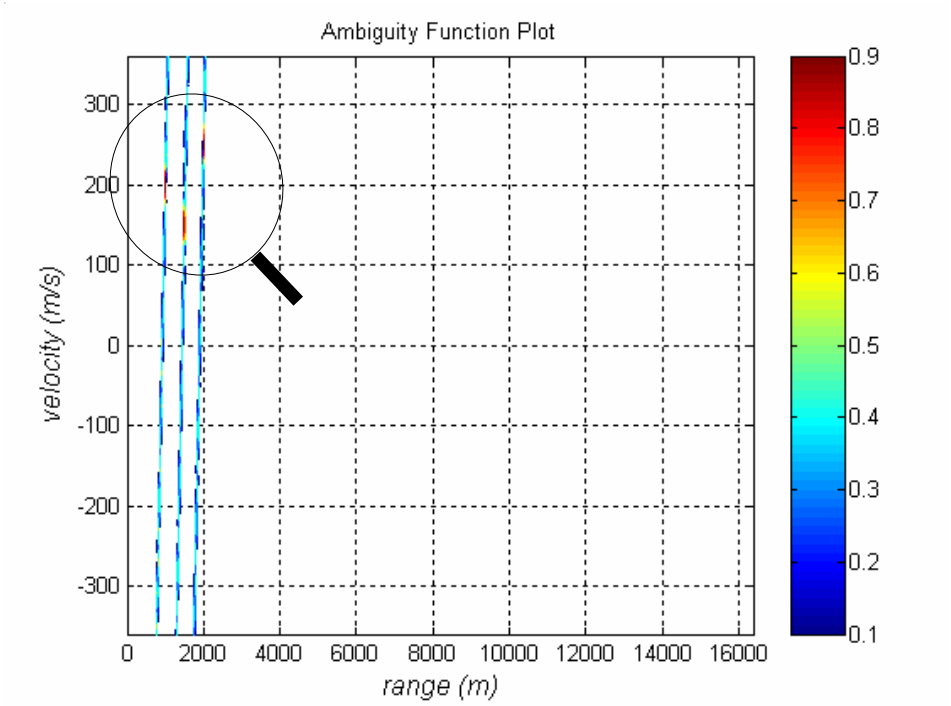

Figure 4.44: 2D Cross - Ambiguity Function plot of the transmitted and received signal for $M = 1024$ $(N_c = 1024)$ P4 code $\left(R_1 = 1km, R_2 = 1.5km, R_3 = 2km, v_1 = 200m/\sec, v_1 = 150m/\sec, v_1 = 250m/\sec\right)$.

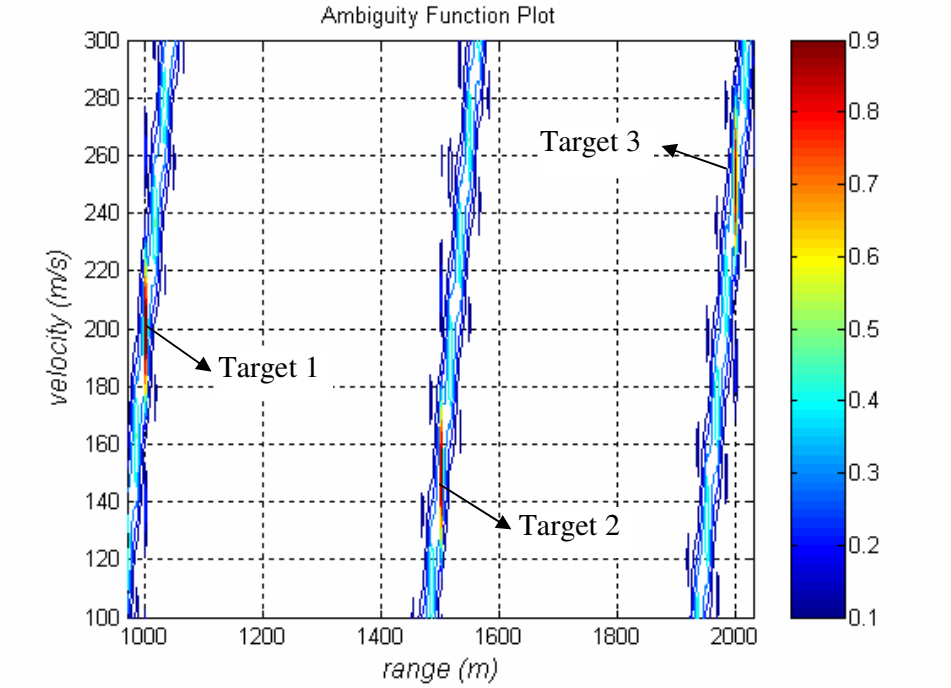

Figure 4.45: Close-up illustration of Figure 4.44.

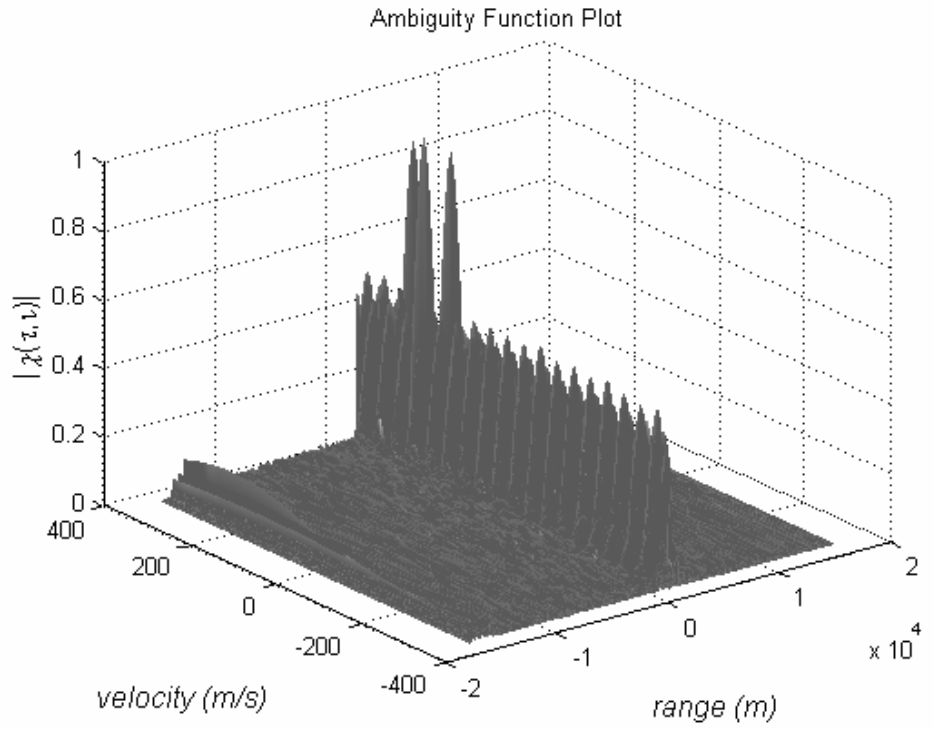

Figure 4.46: 3D Cross - Ambiguity Function plot of the transmitted and received signal for $M = 32$ $(N_c = 1024)$ Frank code $\left(R_1 = 1km, R_2 = 1.5km, R_3 = 2km, v_1 = 200m/\sec, v_1 = 150m/\sec, v_1 = 250m/\sec\right)$.

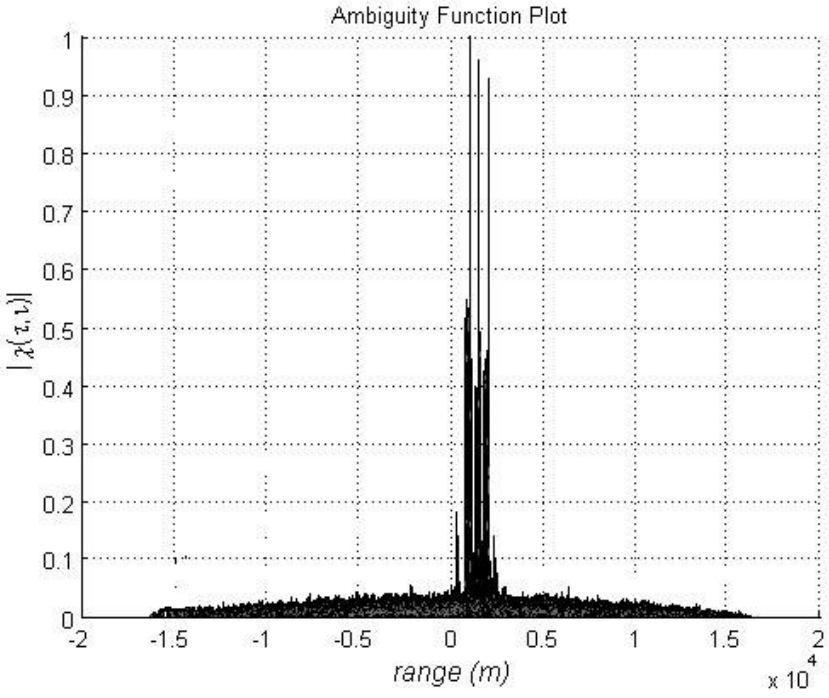

Figure 4.47: Cut along the range axis of Figure 4.46.

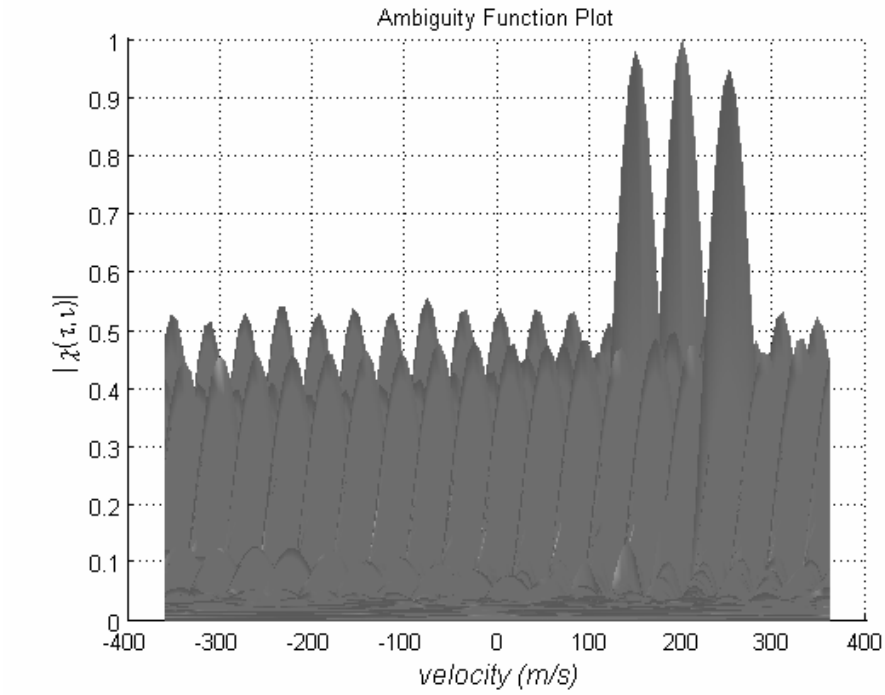

Figure 4.48: Cut along the range axis of Figure 4.4.46.

4.4 Noise Effect on Detection

At this scenario, as in the scenario presented in section 4.2.1, there is one target 2500 m. away from the radar with 250 m/sec. radial velocity with respect to the radar. Also, effect of the noise on detection and behavior of the code types are investigated. For sufficiently high SNR levels, the detection power of the proposed AF approach is not affected much. Even at 0 dB SNR level, the detection of the target is accomplished successfully. For that reason, a particularly low level of SNR at -20 dB is chosen to examine an almost worst case scenario where the noise power is 100 times of the signal power.

The contour plots of the AF output matrices together with their enlarged versions are given in Figure 4.49, Figure 4.50, Figure 4.54, Figure 4.55, Figure 4.59, Figure 4.60, Figure 4.64, Figure 4.65, Figure 4.69, Figures 4.70. 3D AF plots and their cuts along range axis and velocity axis plots are given in Figures 4.51 - 4.53, Figures 4.56 - 4.58, Figures 4.61 - 4.63, Figures 4.66 - 4.68, and Figures 4.71 - 4.73.

When 3D AF plots and their cuts along the range axis and the velocity axis are examined, it can be seen that Frank and P2 coding types have lower side lobe levels than the side lobe levels of other coding types. For these aspects, Frank and P2 coding types give better results than the other coding types.

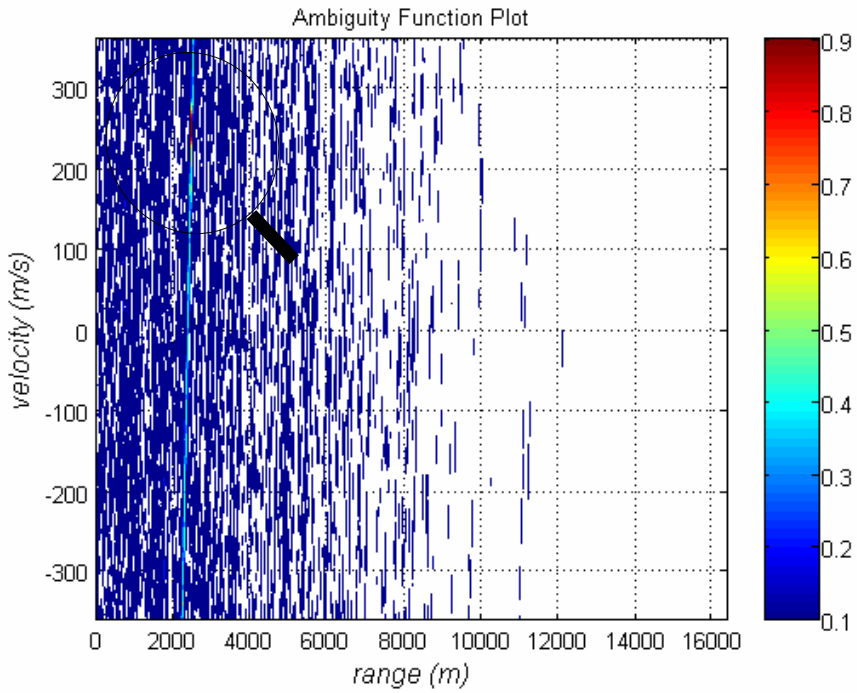

Figure 4.49: 2D Cross - Ambiguity Function plot of the transmitted and received signal for $M = 32$ $(N_c = 1024)$ Frank code with SNR = -20 dB.
($R = 2,5$km, $v = 250m/\sec.$)

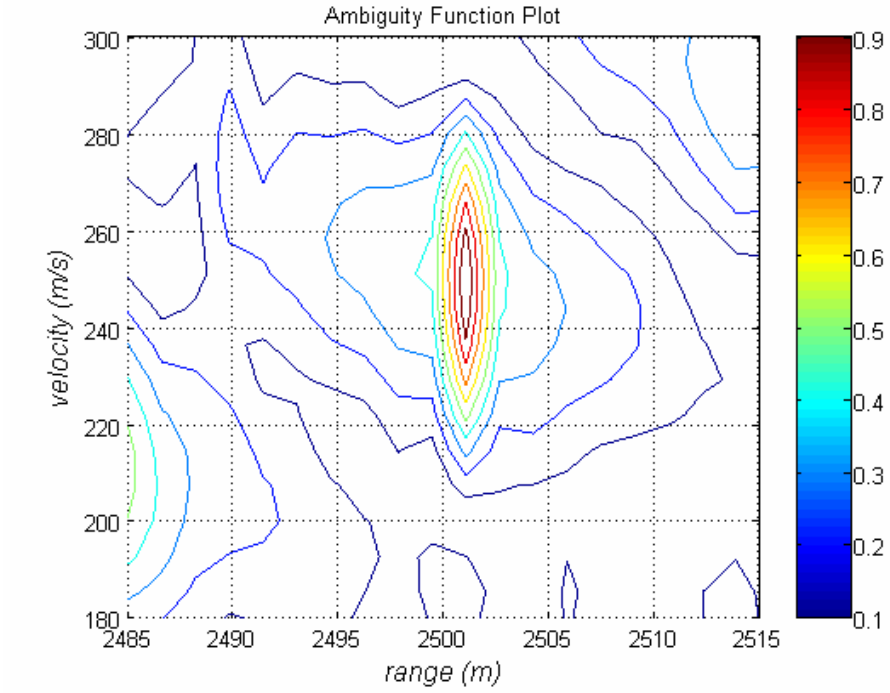

Figure 4.50: Close-up illustration of Figure 4.49.

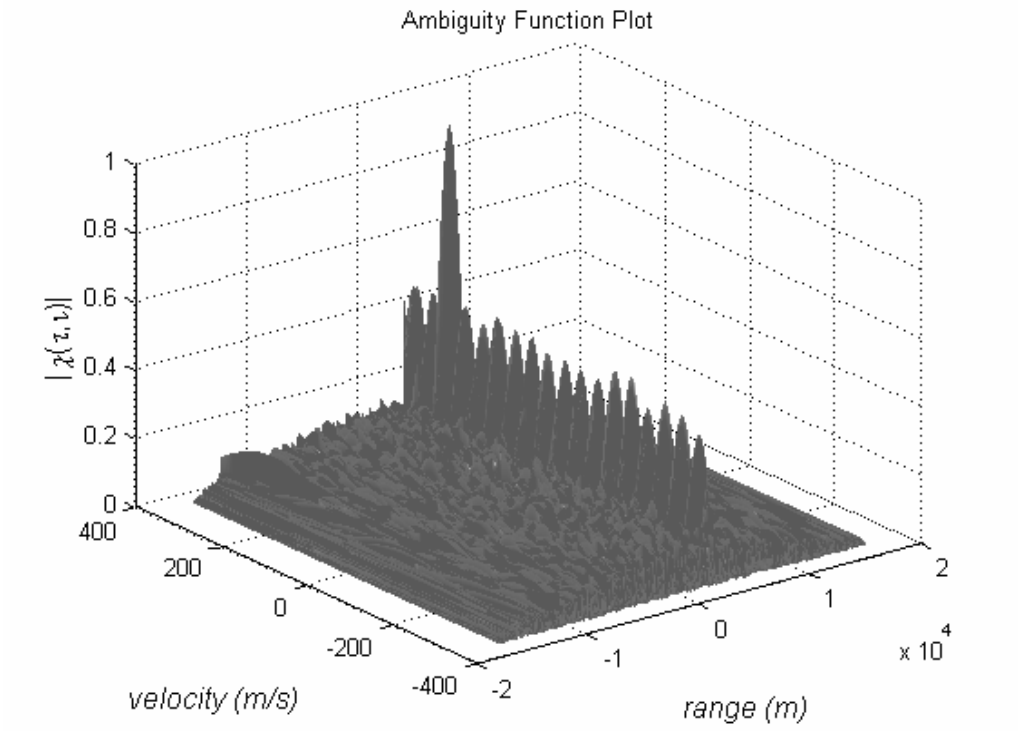

Figure 4.51: 3D Cross - Ambiguity Function plot of the transmitted and received signal for $M = 32$ ($N_c = 1024$) Frank code with SNR = -20 dB ($R = 2{,}5$km, $\nu = 250 m/\sec.$).

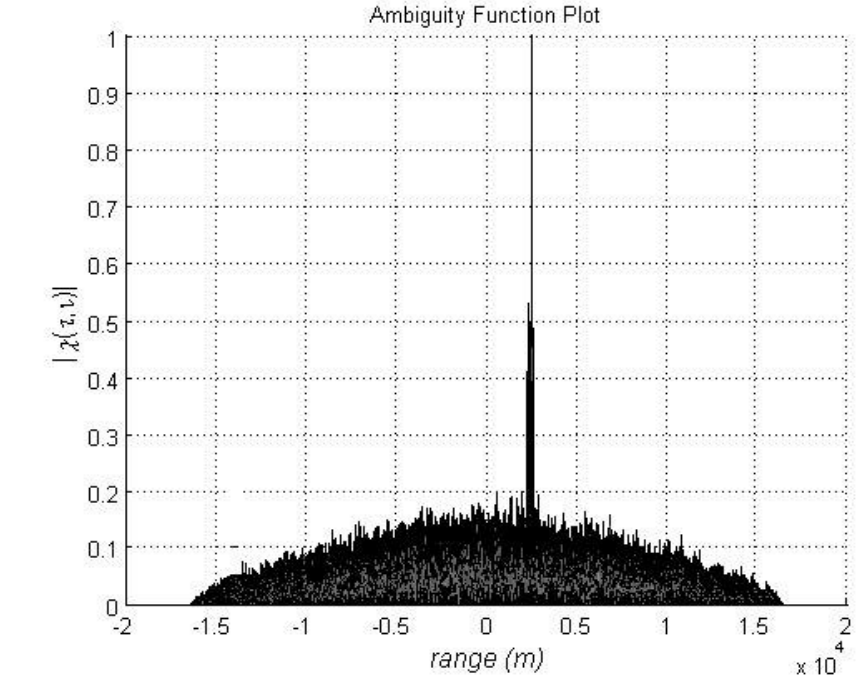

Figure 4.52: Cut along the range axis of Figure 4.51.

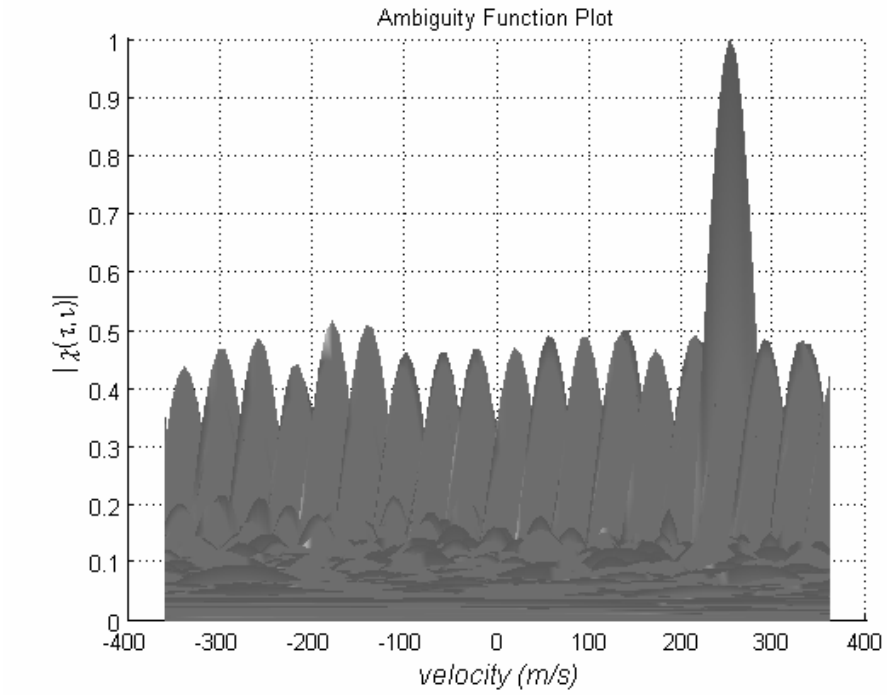

Figure 4.53: Cut along the velocity axis of Figure 4.51.

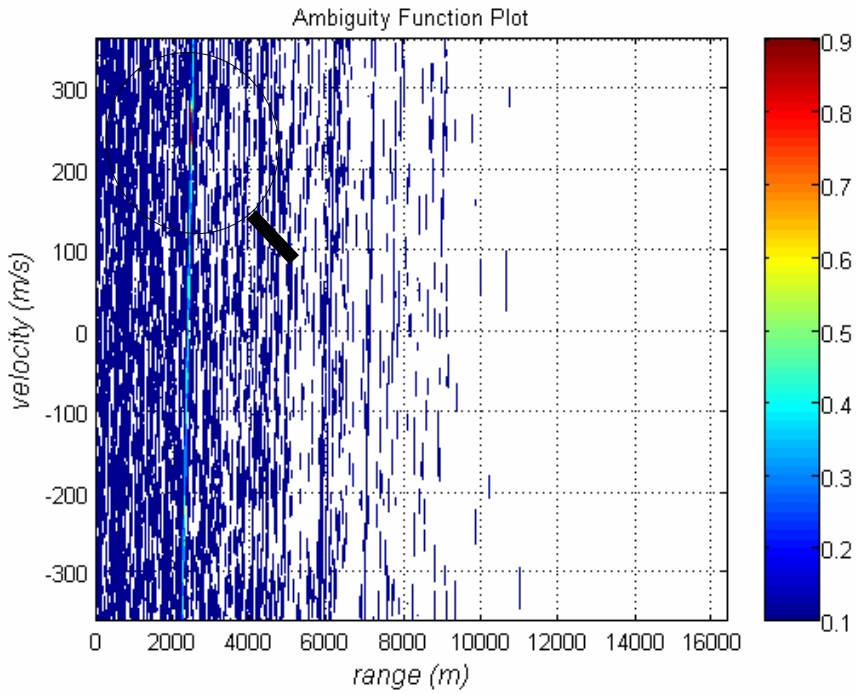

Figure 4.54: 2D Cross - Ambiguity Function plot of the transmitted and received signal for $M = 32$ ($N_c = 1024$) P1 code with SNR = -20 dB ($R = 2{,}5$km, $v = 250 m/\sec.$).

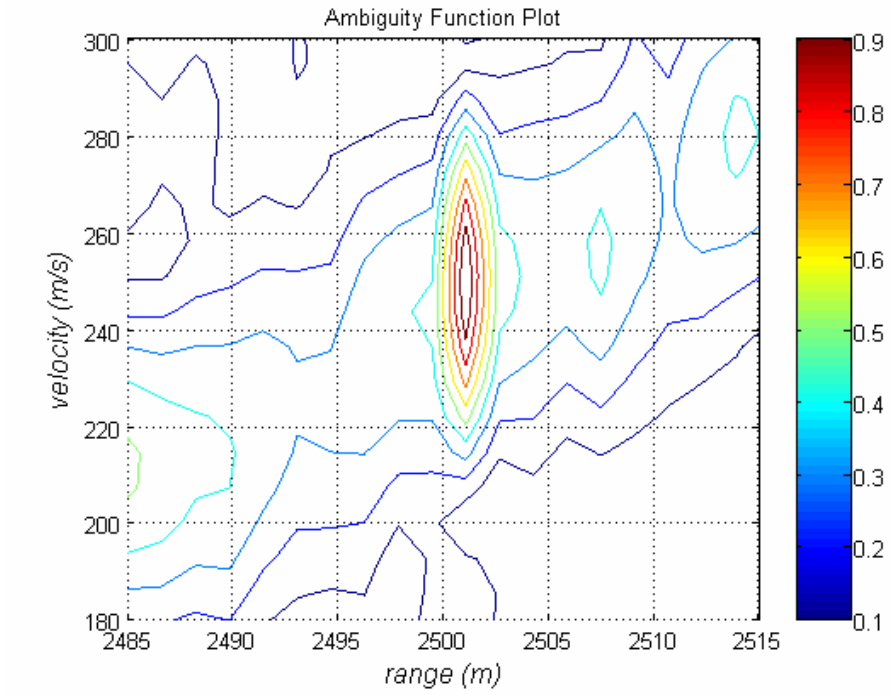

Figure 4.55: Close-up illustration of Figure 4.54.

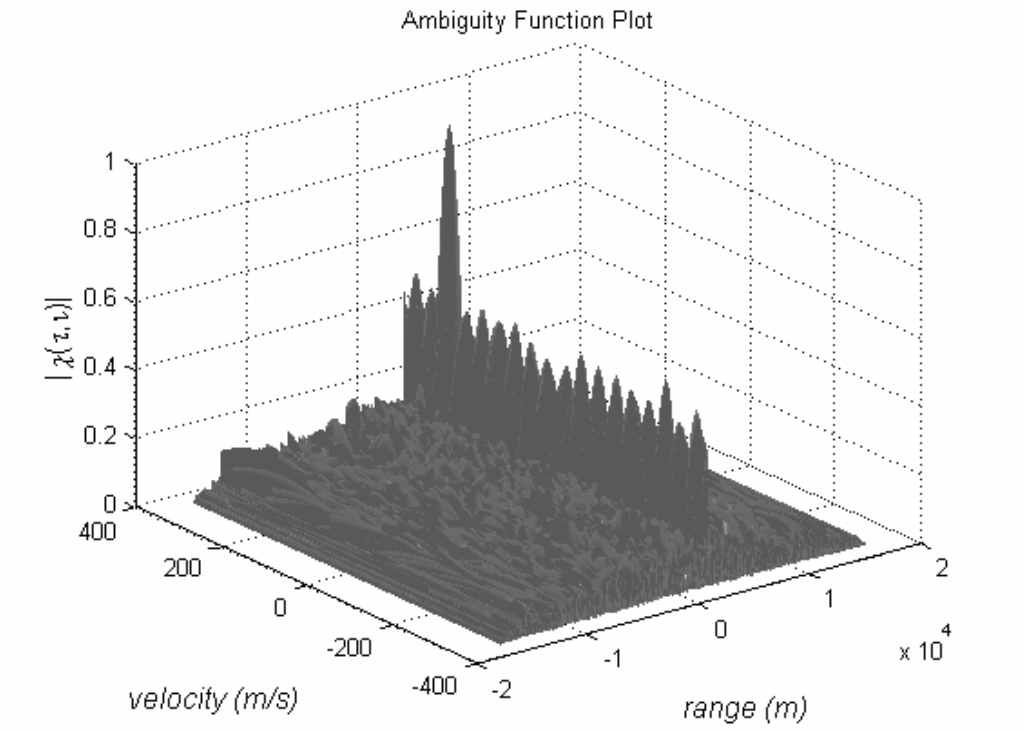

Figure 4.56: 3D Cross - Ambiguity Function plot of the transmitted and received signal for $M = 32$ ($N_c = 1024$) P1 code with SNR = -20 dB
($R = 2,5$km, $\nu = 250 m/\sec.$)

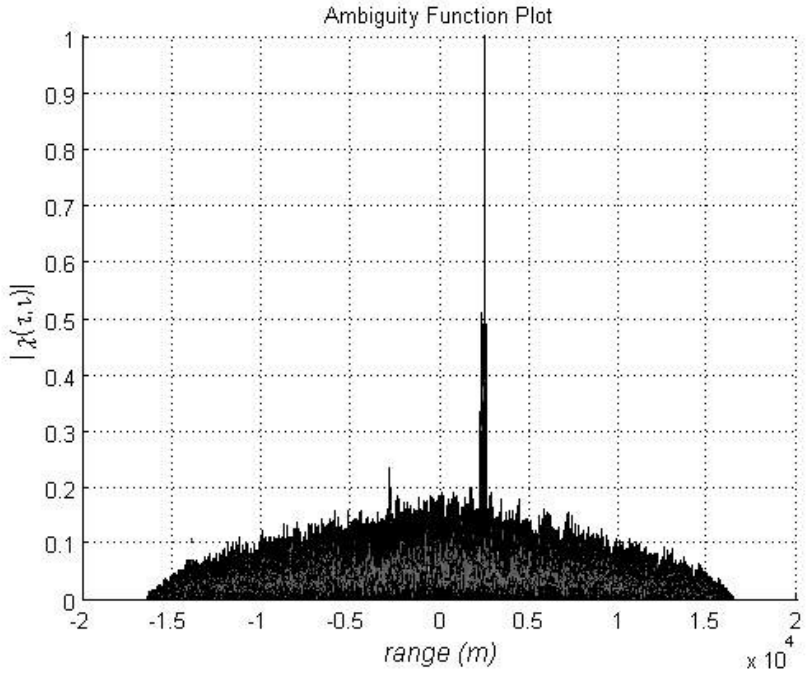

Figure 4.57: Cut along the range axis of Figure 4.56.

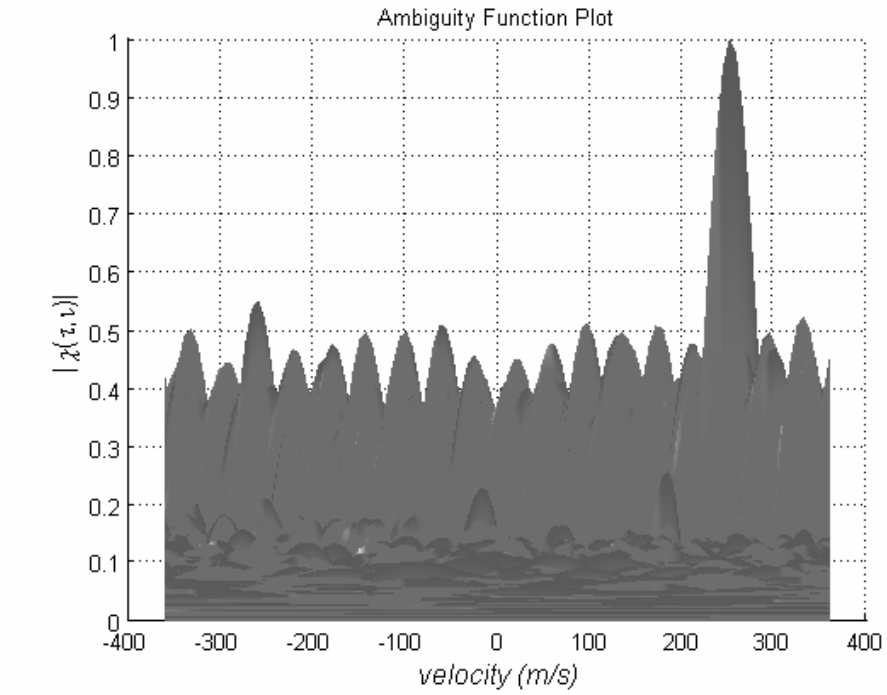

Figure 4.58: Cut along the velocity axis of Figure 4.56.

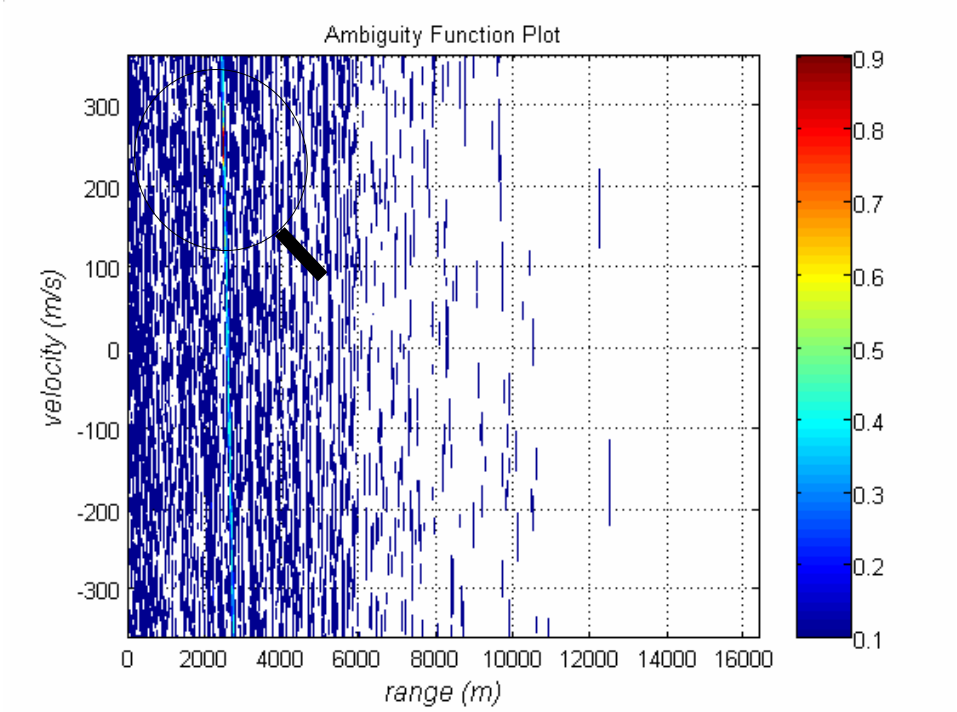

Figure 4.59: 2D Cross - Ambiguity Function plot of the transmitted and received signal for $M = 32$ $(N_c = 1024)$ P2 code with SNR = -20 dB ($R = 2{,}5$km, $v = 250 m/\sec.$).

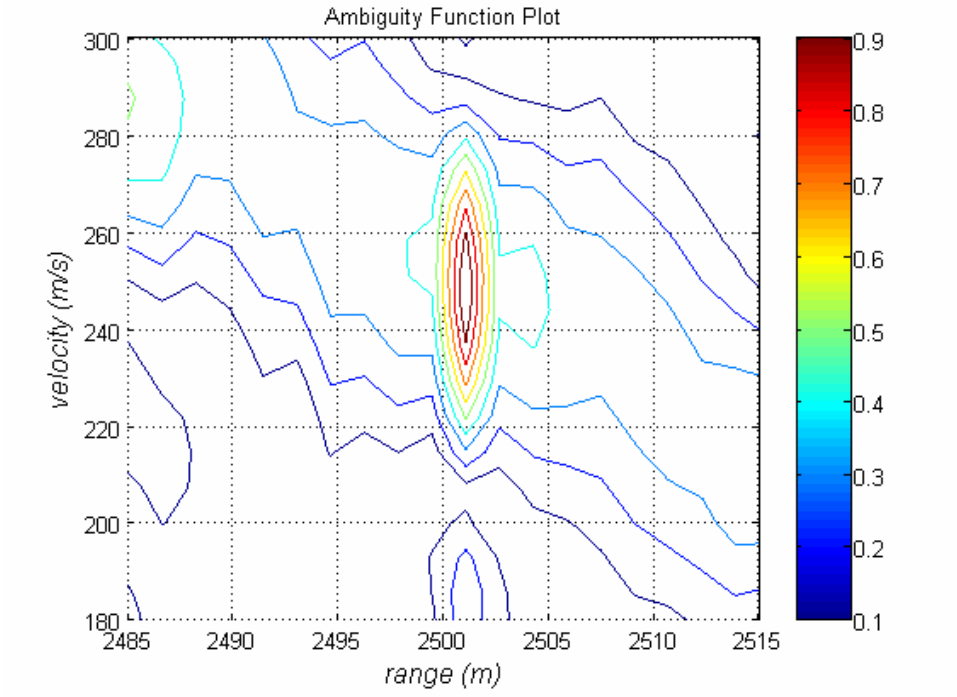

Figure 4.60: Close-up illustration of Figure 4.59.

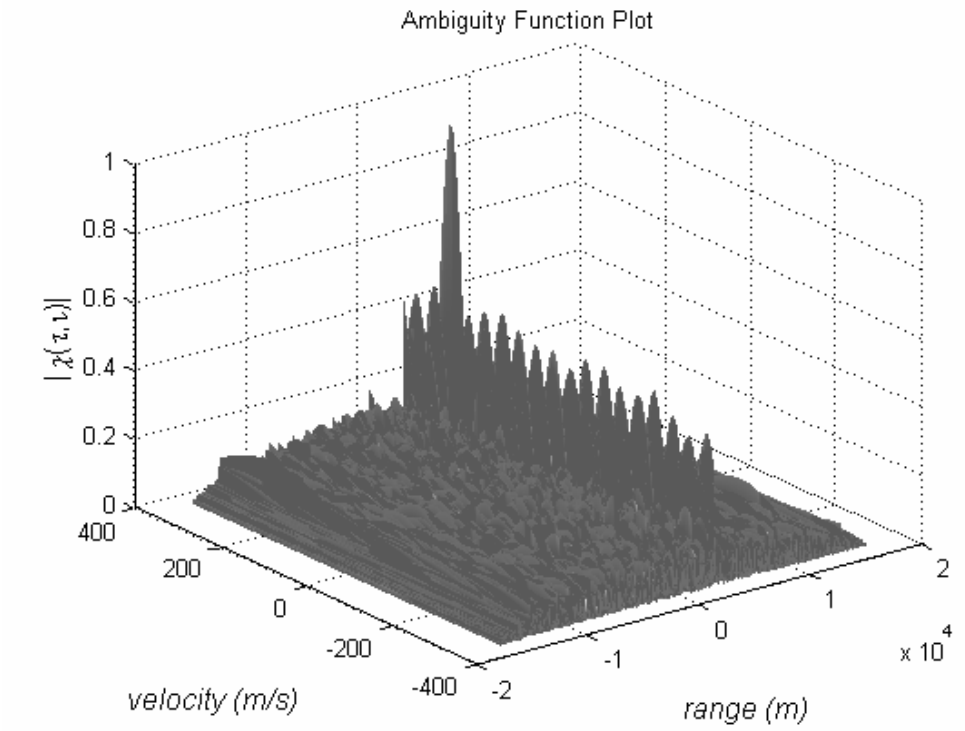

Figure 4.61: 3D Cross - Ambiguity Function plot of the transmitted and received signal for $M = 32$ $(N_c = 1024)$ P2 code with SNR = -20 dB
($R = 2,5$km, $\nu = 250 m/\sec.$)

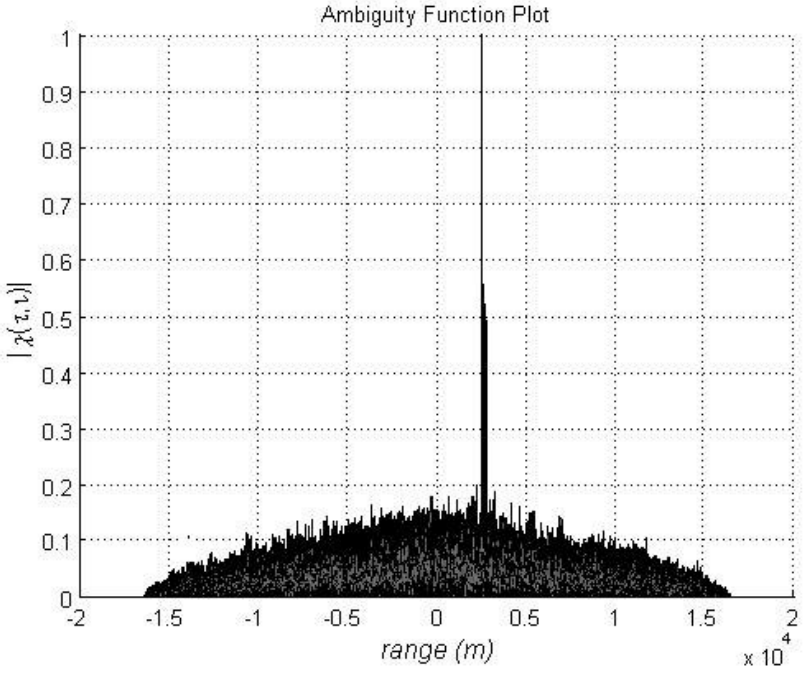

Figure 4.62: Cut along the range axis of Figure 4.61.

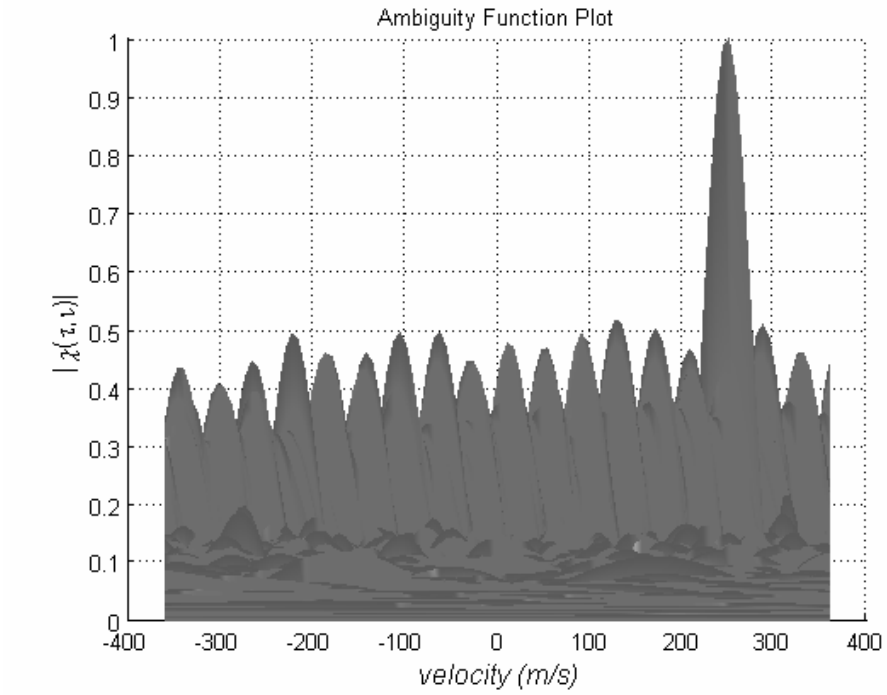

Figure 4.63: Cut along the Doppler axis of Figure 4.61.

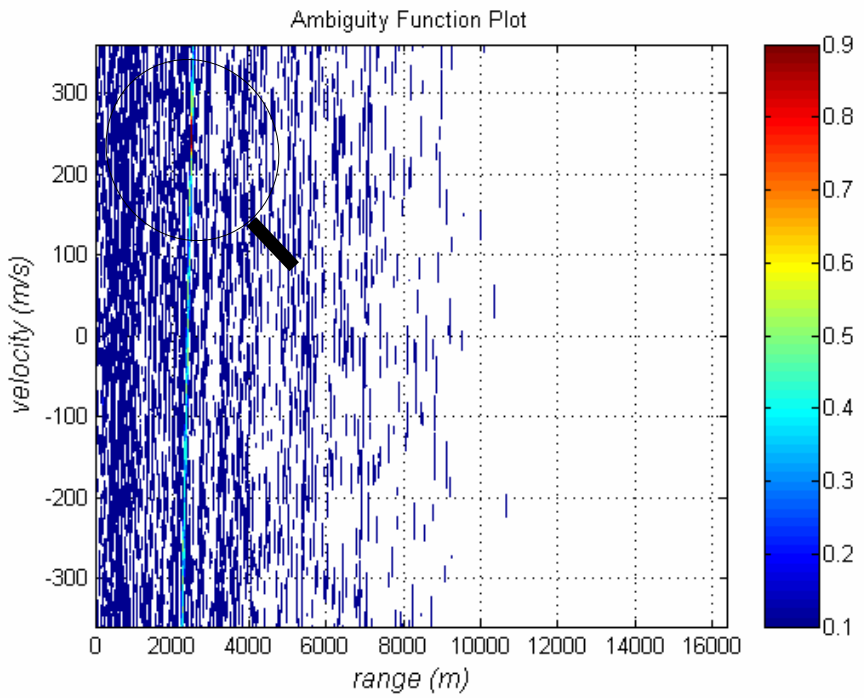

Figure 4.64: 2D Cross - Ambiguity Function plot of the transmitted and received signal for $M = 1024$ ($N_c = 1024$) P3 code with SNR = -20 dB ($R = 2,5\text{km},\ v = 250m/\sec.$)

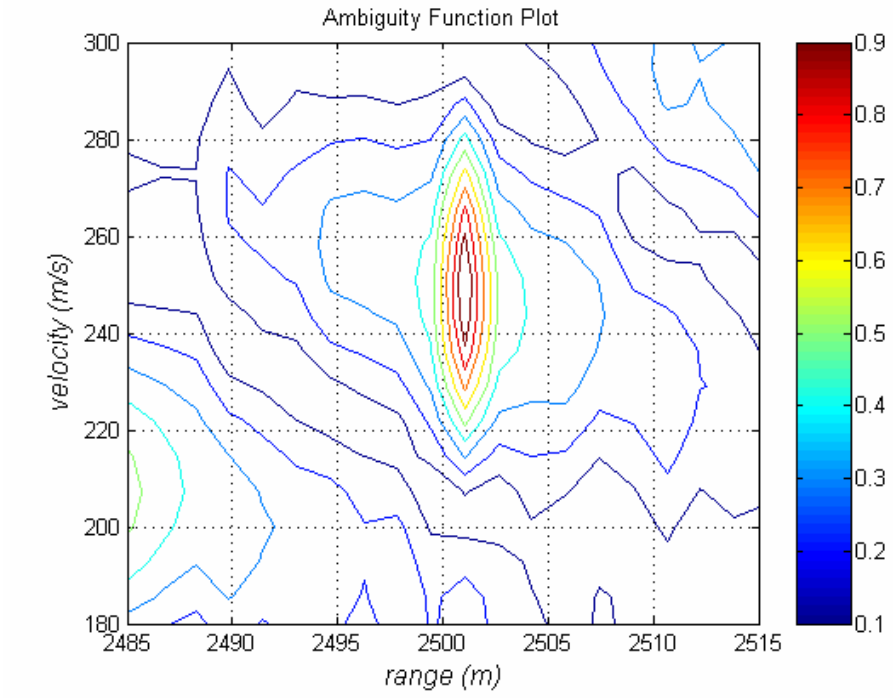

Figure 4.65: Close-up illustration of Figure 4.64.

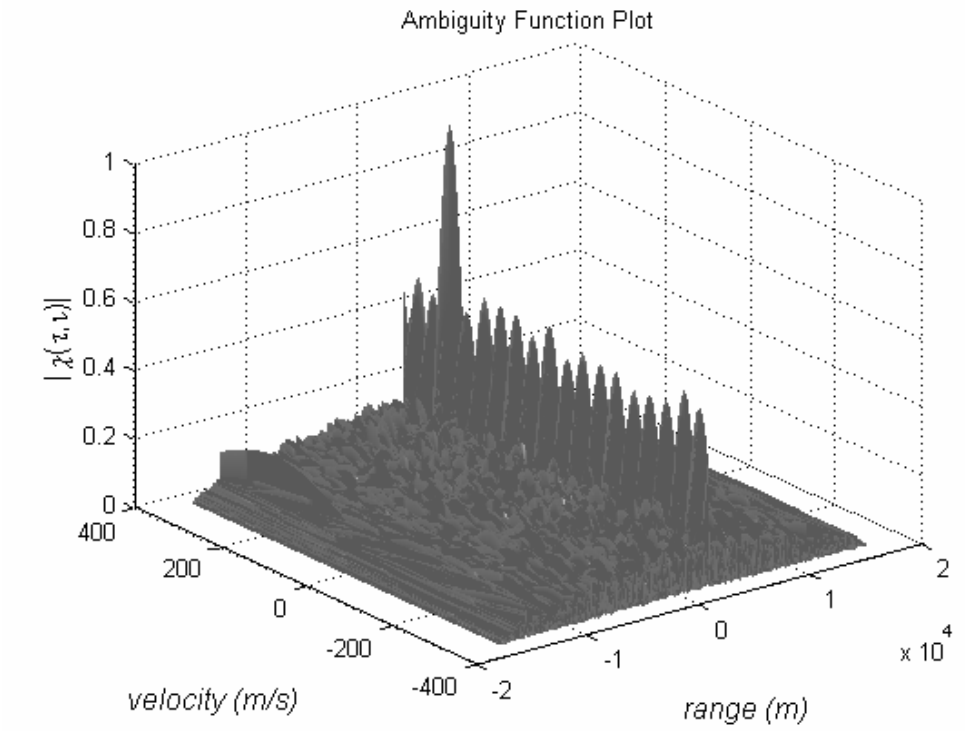

Figure 4.66: 3D Cross - Ambiguity Function plot of the transmitted and received signal for $M = 1024$ ($N_c = 1024$) P3 code with SNR = -20 dB ($R = 2{,}5\text{km}$, $v = 250 m/\sec.$).

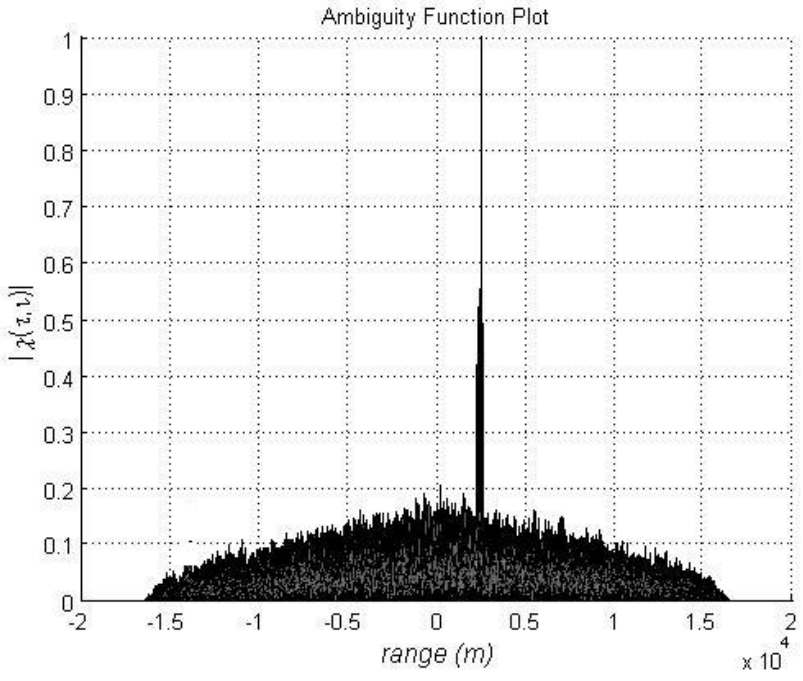

Figure 4.67: Cut along the range axis of Figure 4.66.

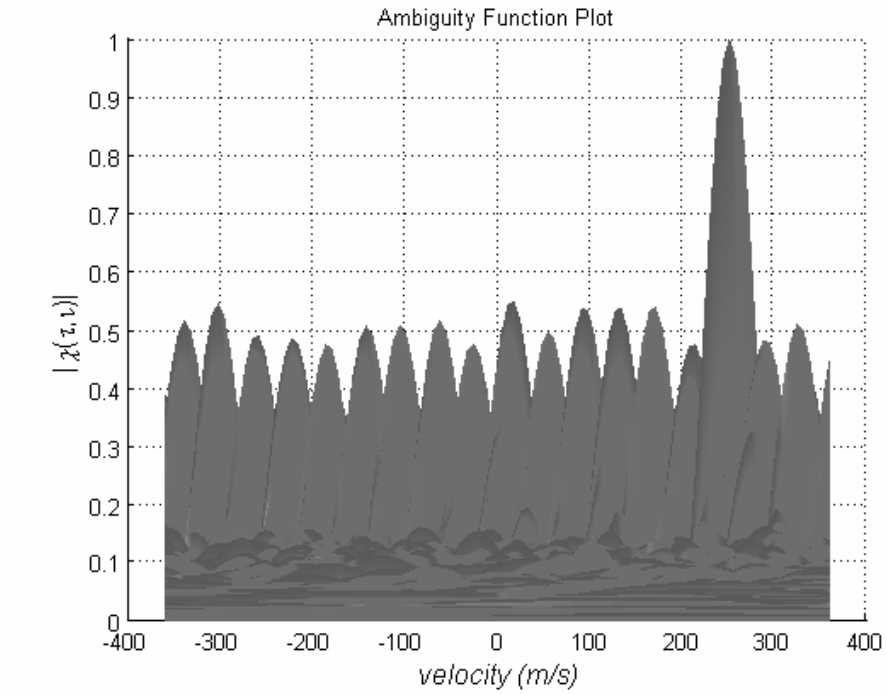

Figure 4.68: Cut along the Doppler axis of Figure 4.66.

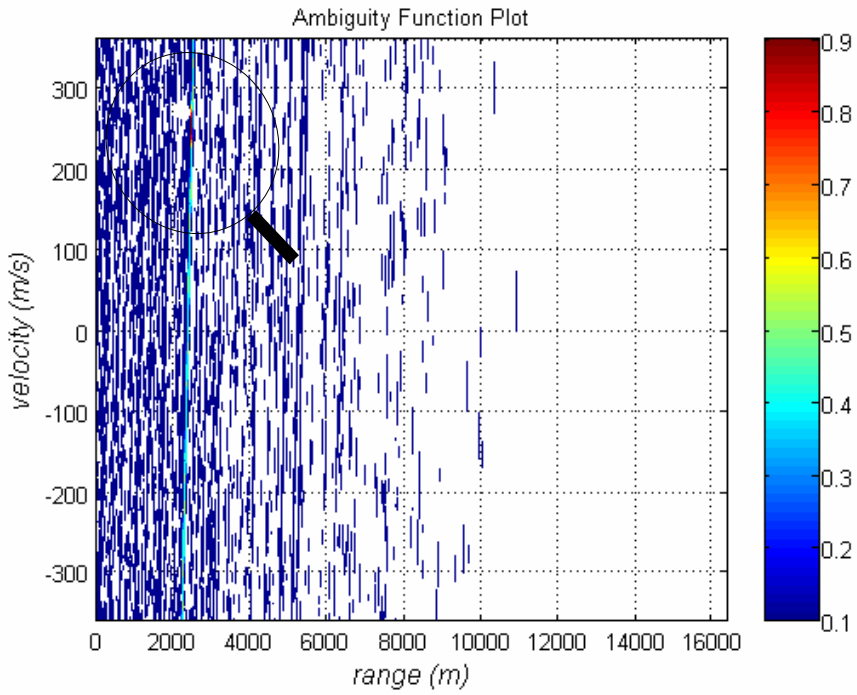

Figure 4.69: 2D Cross - Ambiguity Function plot of the transmitted and received signal for $M = 1024$ ($N_c = 1024$) P4 code with SNR = -20 dB ($R = 2{,}5\text{km}$, $v = 250 m/\text{sec}.$).

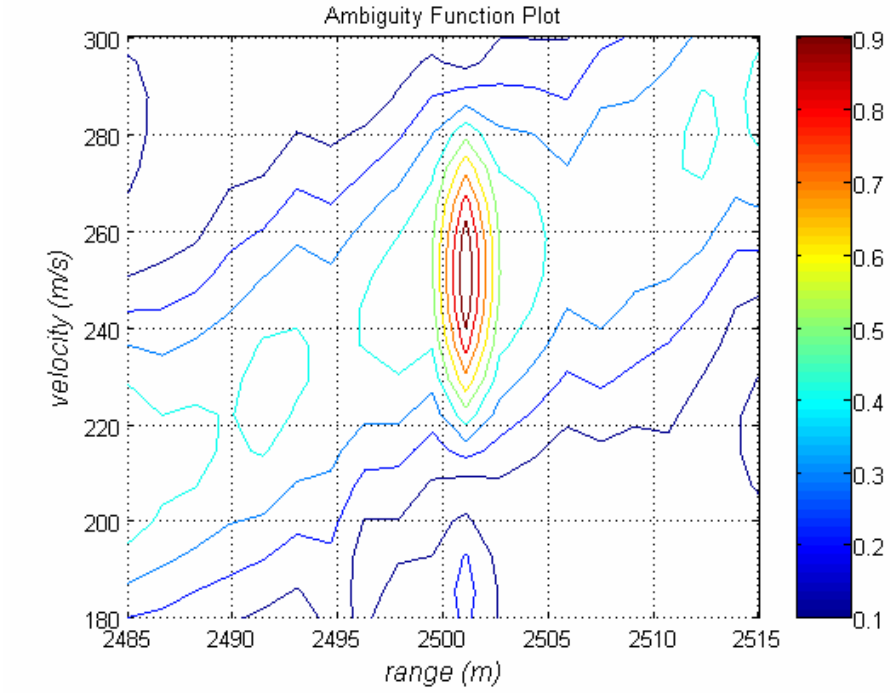

Figure 4.70: Close-up illustration of Figure 4.69.

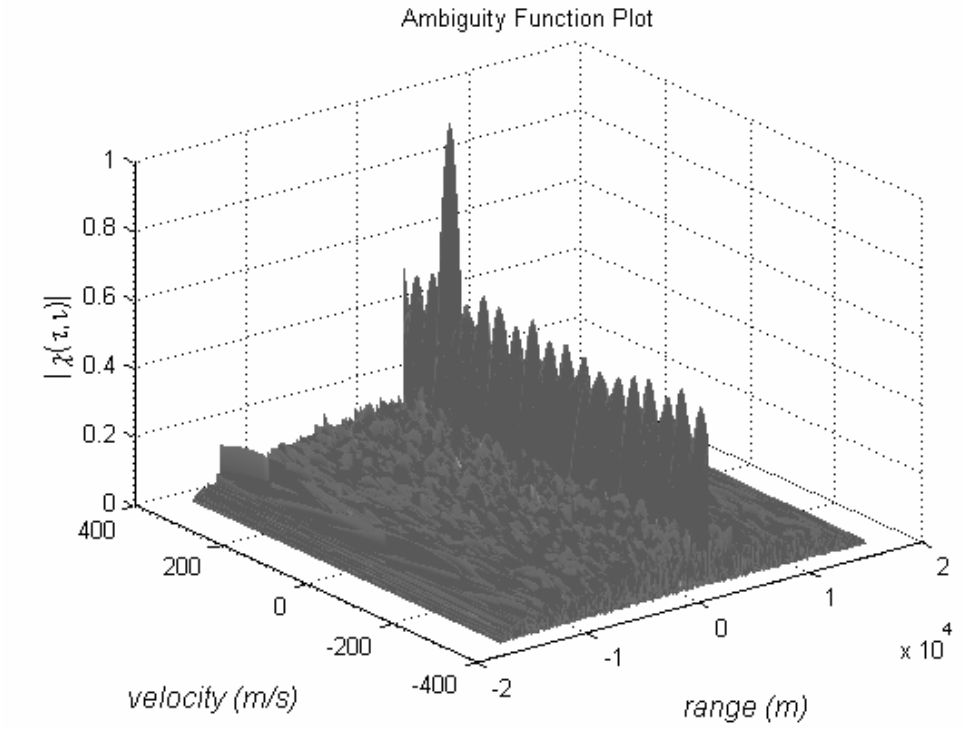

Figure 4.71: 3D Cross - Ambiguity Function plot of the transmitted and received signal for $M = 1024$ ($N_c = 1024$) P4 code with SNR = -20 dB ($R = 2{,}5$km, $v = 250 m/\sec.$).

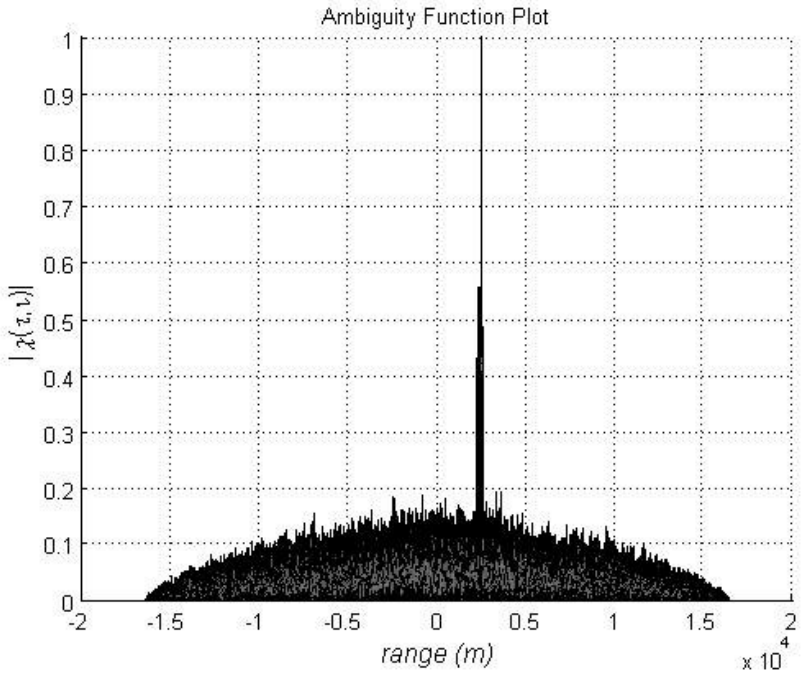

Figure 4.72: Cut along the range axis of Figure 4.71.

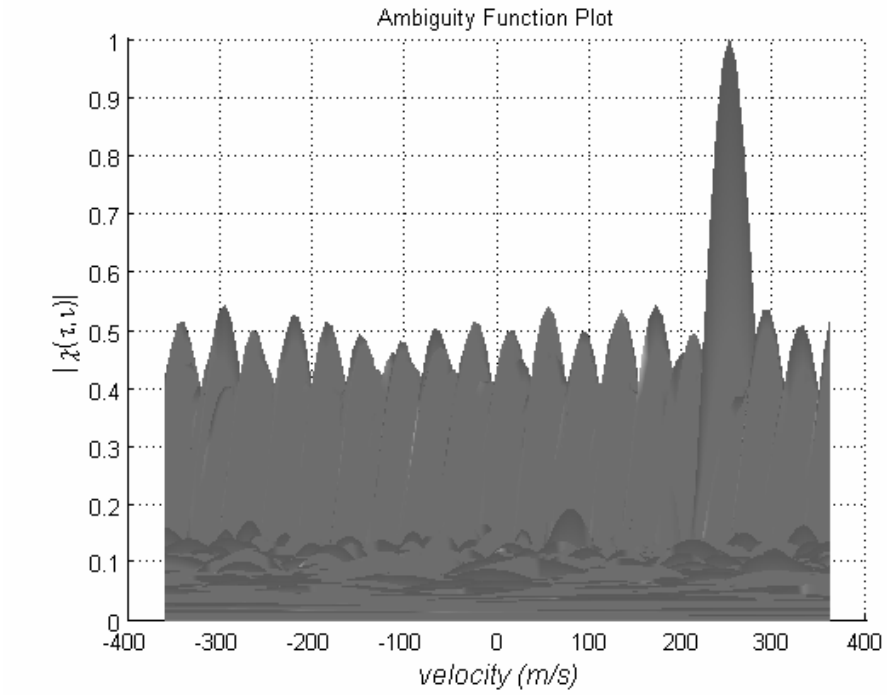

Figure 4.73: Cut along the Doppler axis of Figure 4.71.

4.5 Range Resolution

For phase-coded radars range resolution is given by eqn. 4.1. Along this thesis, codes are designed for $\Delta R = 16$ m. For this choice, various target detection are carried on observing range resolution effects. The results of these simulations are presented in Figures 4.74 through 4.93.

In Figures 4.74, 4.76, 4.78, 4.80, 4.82, 4.84, 4.86, 4.88, 4.90, and 4.92 one red point is observed. That is, at first glance to these figures, one target is observed. For detailed examination, these figures are enlarged. Close-up illustrations are given at Figures 4.75, 4.77, 4.79, 4.81, 4.83, 4.85, 4.87, 4.89, 4.91, and 4.93.

In the first target detection scenario of this section, we have two targets at 1000 meters and 1015 meters range values with both of them having the same radial velocity which is 200 m/sec. As the distance between these two targets is smaller than range resolution value of 16 meters, the targets are detected with incorrect velocities as seen in Figures 4.75, 4.79, 4.83, 4.87, and 4.91 for the Frank, P1, P2, P3, and P4 codes, respectively. The center of the target locations in these AF contour plots must be at 200 m/sec but the center of the target locations are not observed at these expected points. That is to say the range resolution limits also affect the extracted velocity values and eventually the targets can not be distinguished correctly.

In the next target detection scenario, we still have two targets with the same velocity of 200 m/sec., at the ranges are 1000 meters and 1017 meters. This time, the distance between targets is longer than the range resolution value so that targets are detected at correct velocities as seen Figures 4.77, 4.81, 4.85, 4.89, 4.93 for Frank, P1, P2, P3, and P4 codes, respectively. The center of target locations in these AF contour plots must be at 200 m/sec and also the centers of the target locations are roughly at the expected points.

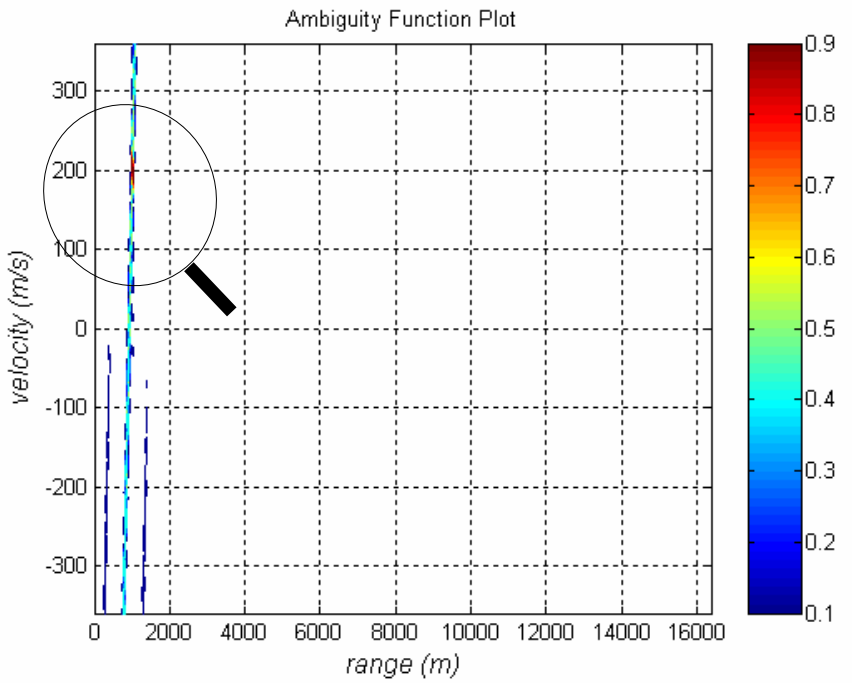

Figure 4.74: 2D Cross - Ambiguity Function plot of the transmitted and received signal for $M = 32$ $(N_c = 1024)$ Frank code

$\left(R_1 = 1000m, R_2 = 1015m, v_{1,2} = 200m/\sec., \Delta R = 16m.\right)$

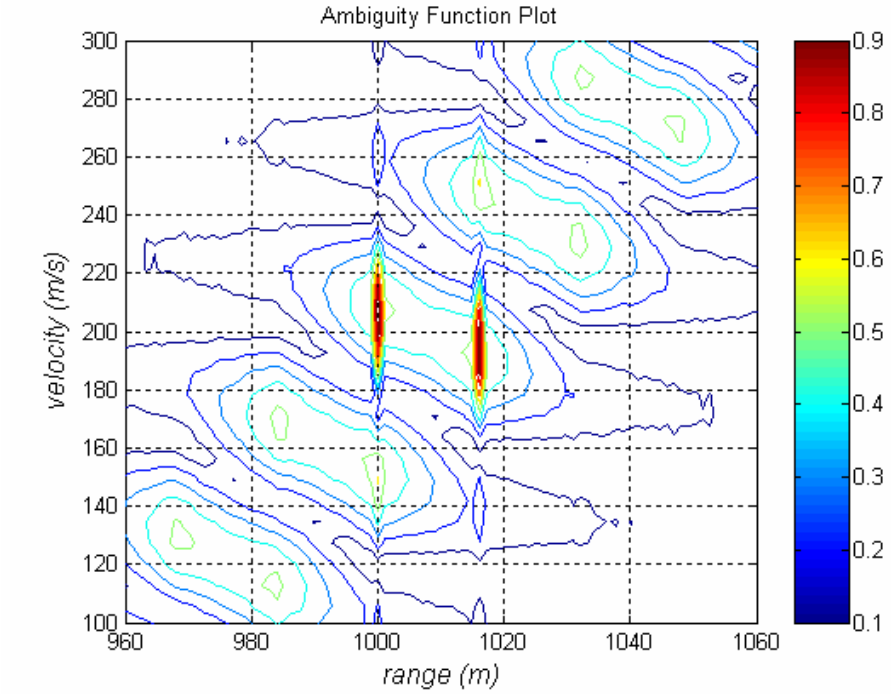

Figure 4.75: Close-up illustration of Figure 4.74.

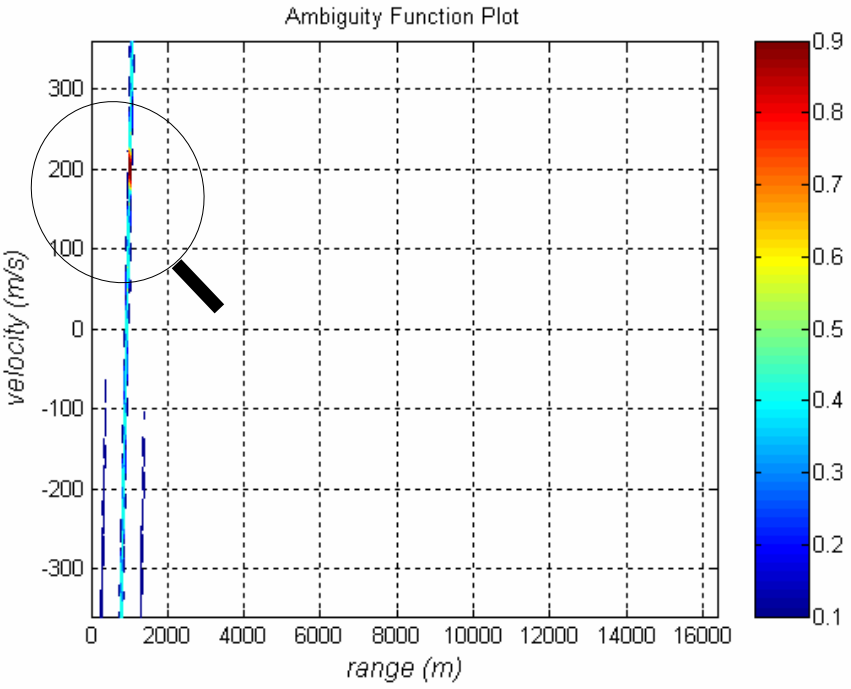

Figure 4.76: 2D Cross - Ambiguity Function plot of the transmitted and received signal for $M = 32$ $(N_c = 1024)$ Frank code $\left(R_1 = 1000m, R_2 = 1017m, v_{1,2} = 200m/\sec., \Delta R = 16m.\right)$.

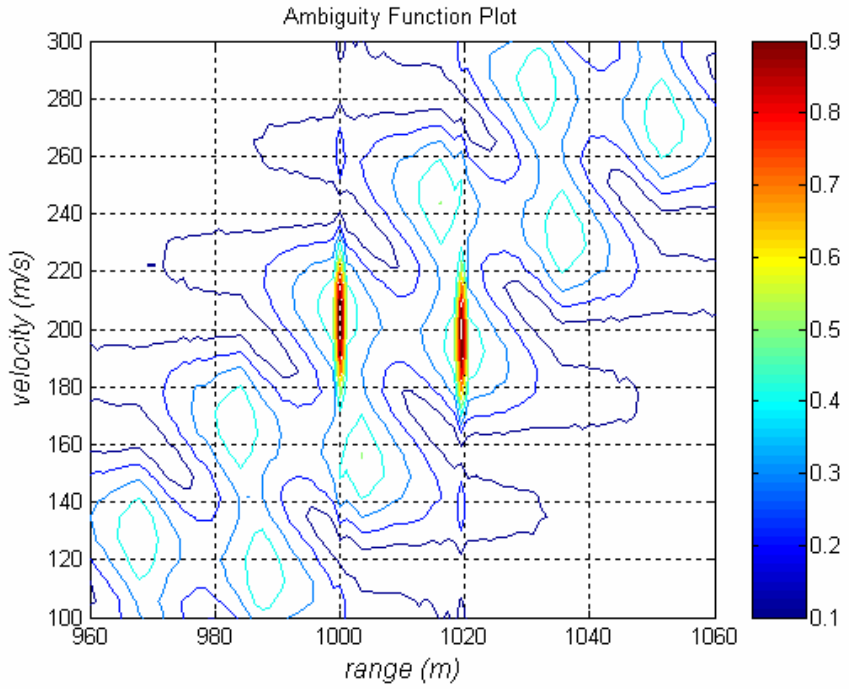

Figure 4.77: Close-up illustration of Figure 4.76.

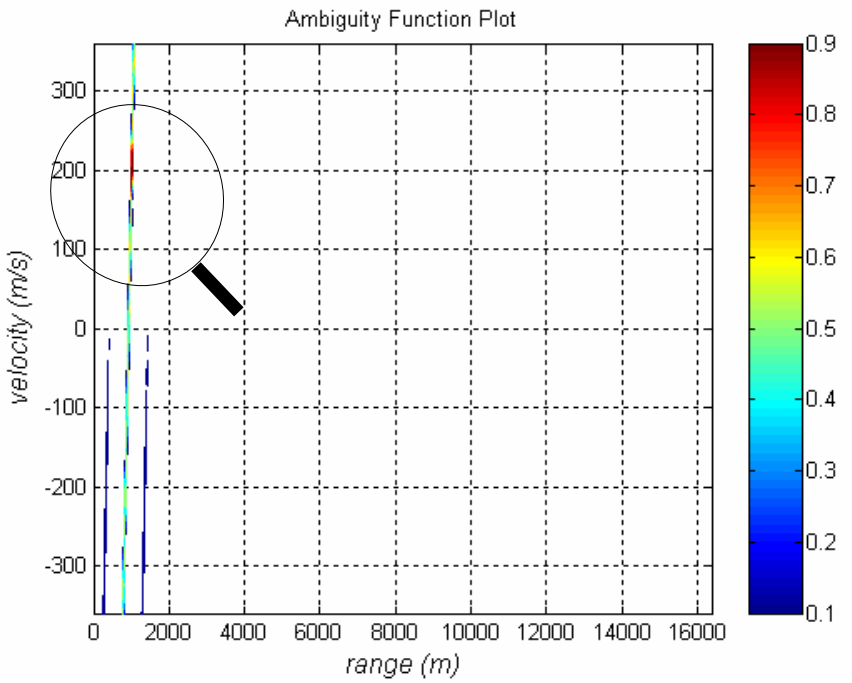

Figure 4.78: 2D Cross - Ambiguity Function plot of the transmitted and received signal for $M = 32$ $(N_c = 1024)$ P1 code $\left(R_1 = 1000m, R_2 = 1015m, v_{1,2} = 200m/\sec., \Delta R = 16m.\right)$.

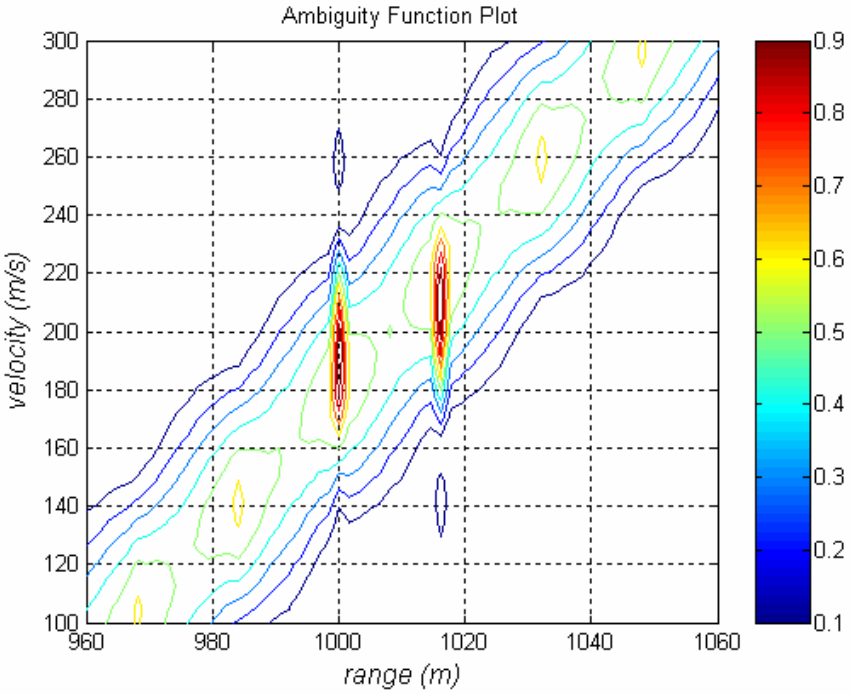

Figure 4.79: Close-up illustration of Figure 4.78.

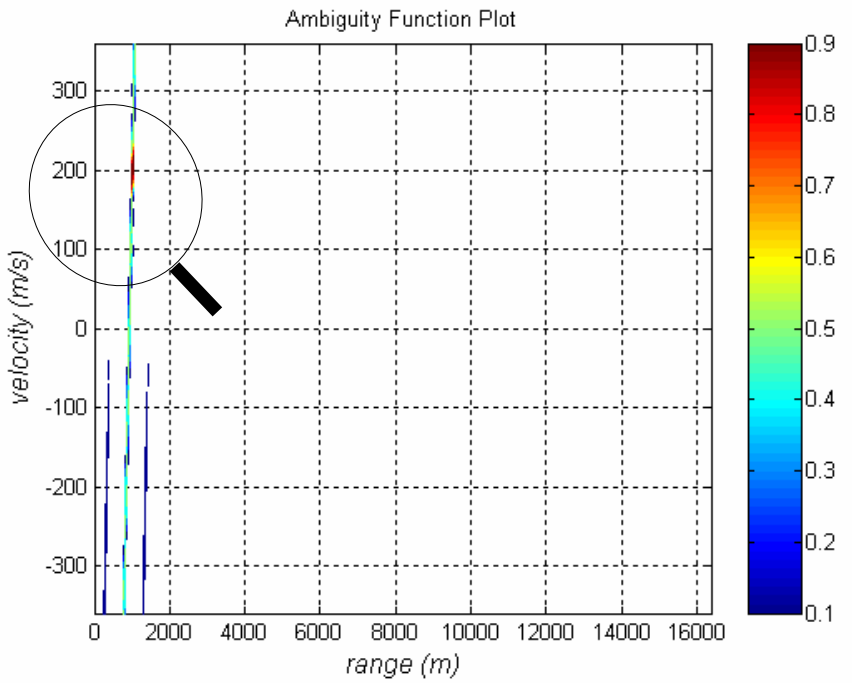

Figure 4.80: 2D Cross - Ambiguity Function plot of the transmitted and received signal for $M = 32$ $(N_c = 1024)$ P1 code $\left(R_1 = 1000m, R_2 = 1017m, v_{1,2} = 200m/\sec., \Delta R = 16m.\right)$.

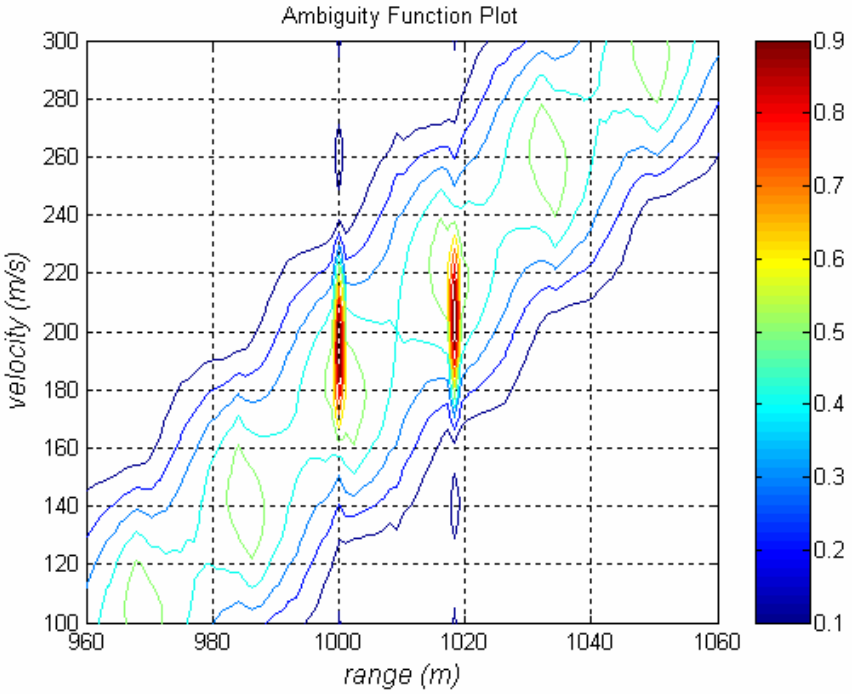

Figure 4.81: Close-up illustration of Figure 4.80.

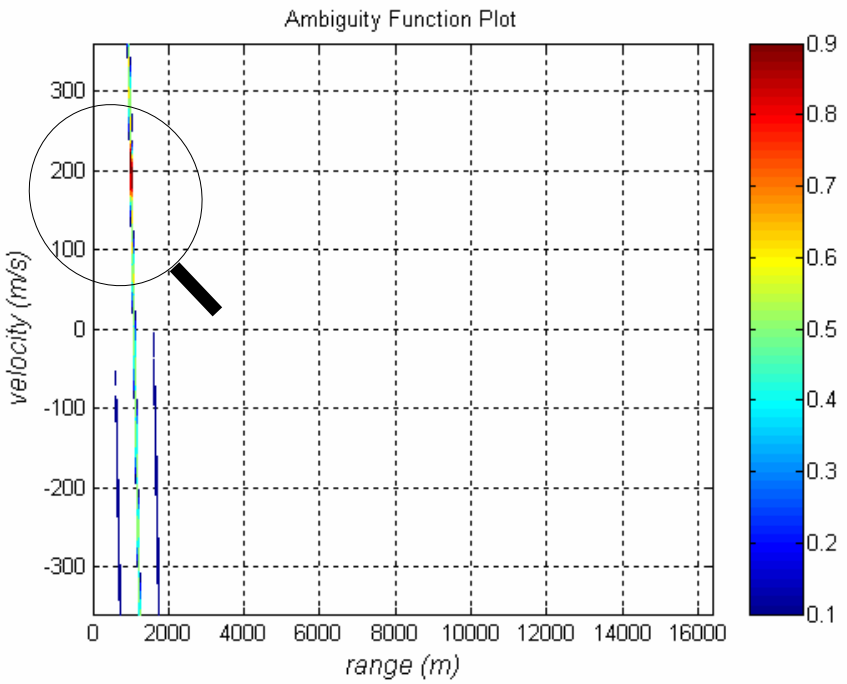

Figure 4.82: 2D Cross - Ambiguity Function plot of the transmitted and received signal for $M = 32$ $(N_c = 1024)$ P2 code $\left(R_1 = 1000m, R_2 = 1015m, v_{1,2} = 200m/\sec., \Delta R = 16m.\right)$.

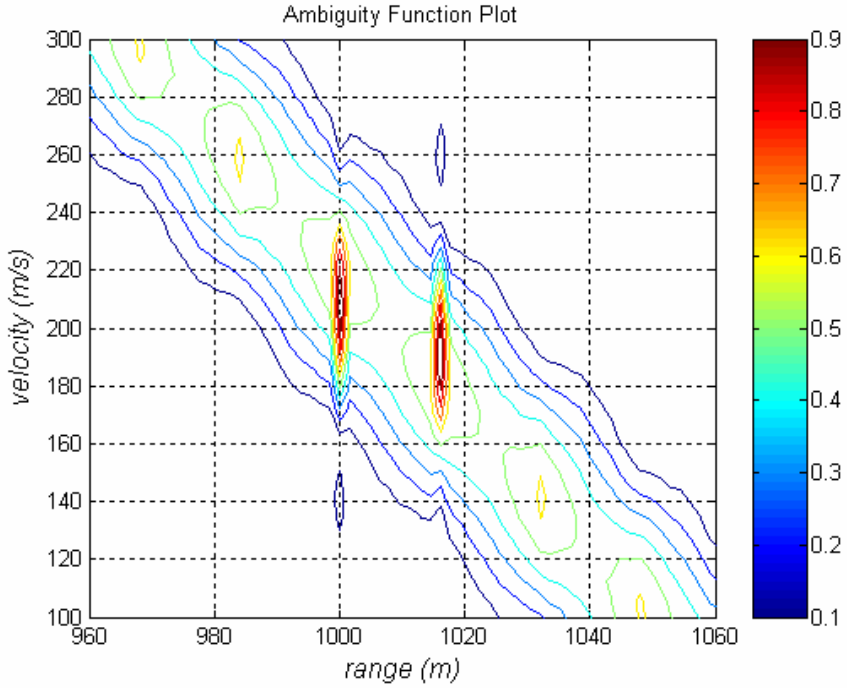

Figure 4.83: Close-up illustration of Figure 4.82.

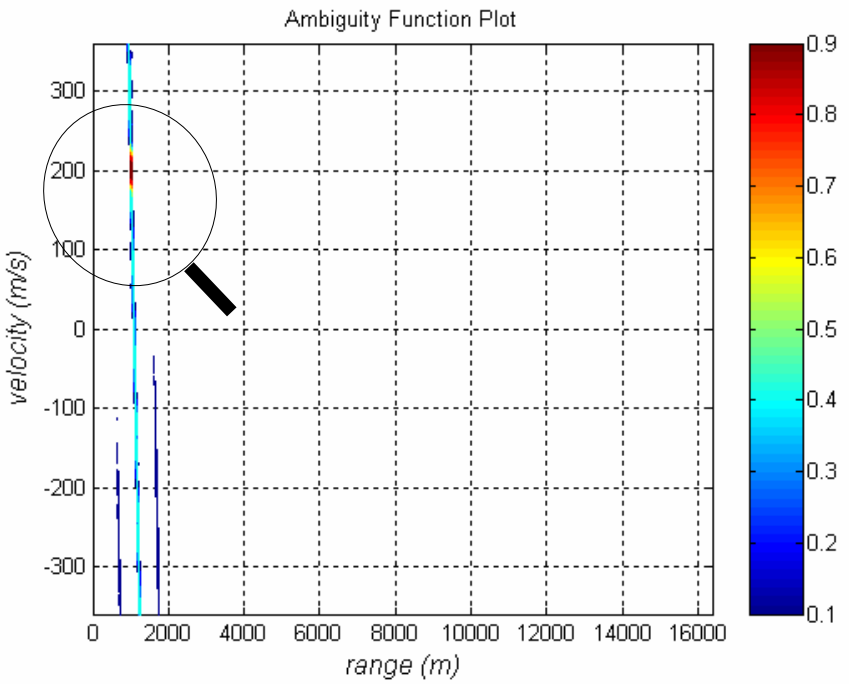

Figure 4.84: 2D Cross - Ambiguity Function plot of the transmitted and received signal for $M = 32$ $(N_c = 1024)$ P2 code $\left(R_1 = 1000m, R_2 = 1017m, v_{1,2} = 200m/\sec., \Delta R = 16m.\right)$.

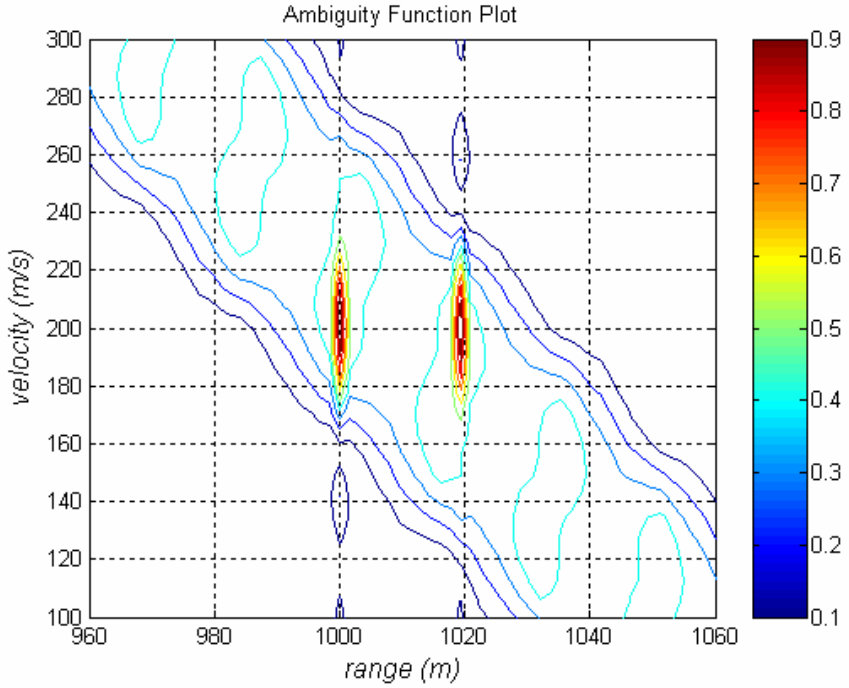

Figure 4.85: Close-up illustration of Figure 4.84.

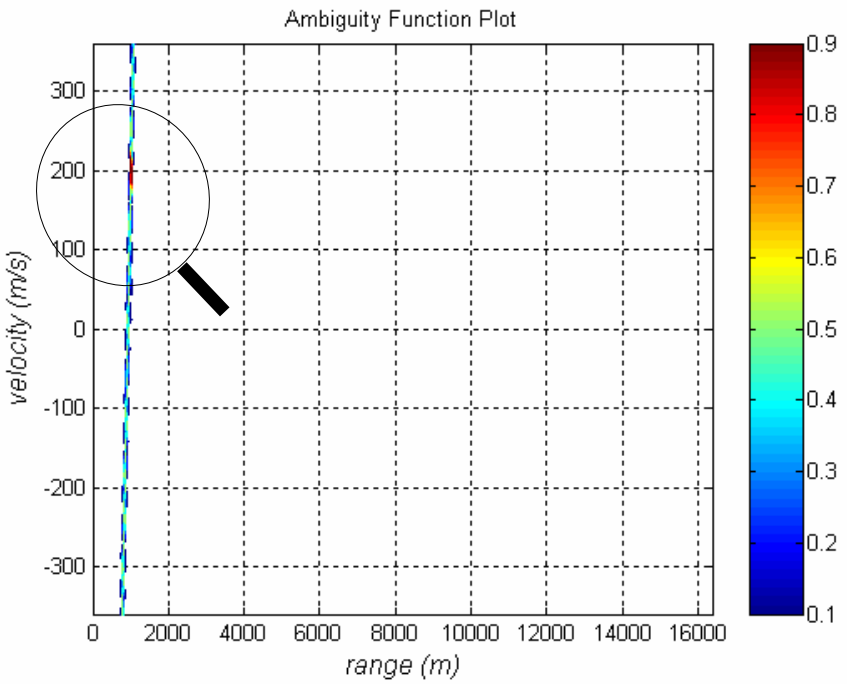

Figure 4.86: 2D Cross - Ambiguity Function plot of the transmitted and received signal for $M = 1024$ $(N_c = 1024)$ P3 code $\left(R_1 = 1000m, R_2 = 1015m, v_{1,2} = 200m/\sec., \Delta R = 16m.\right)$.

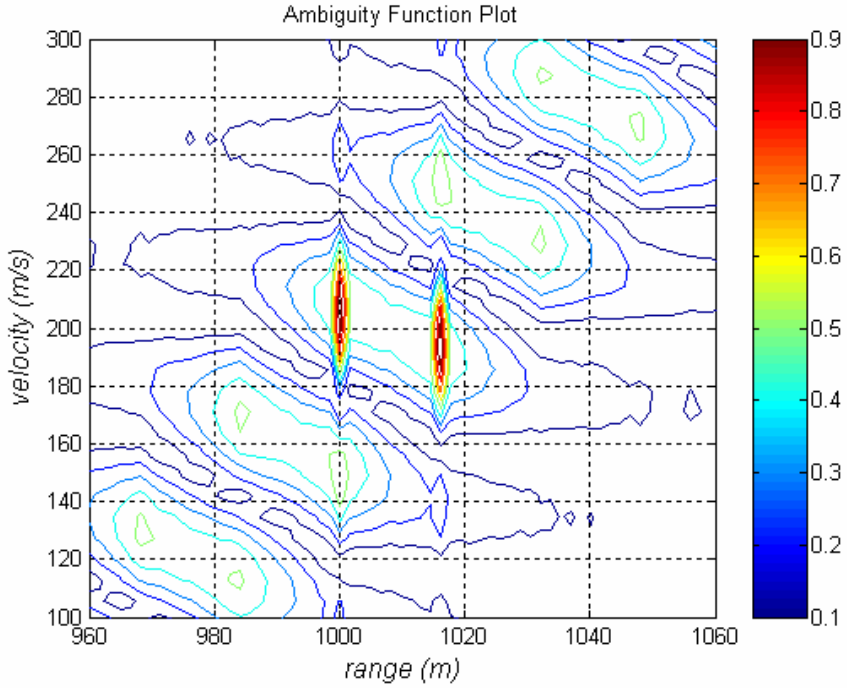

Figure 4.87: Close-up illustration of Figure 4.86.

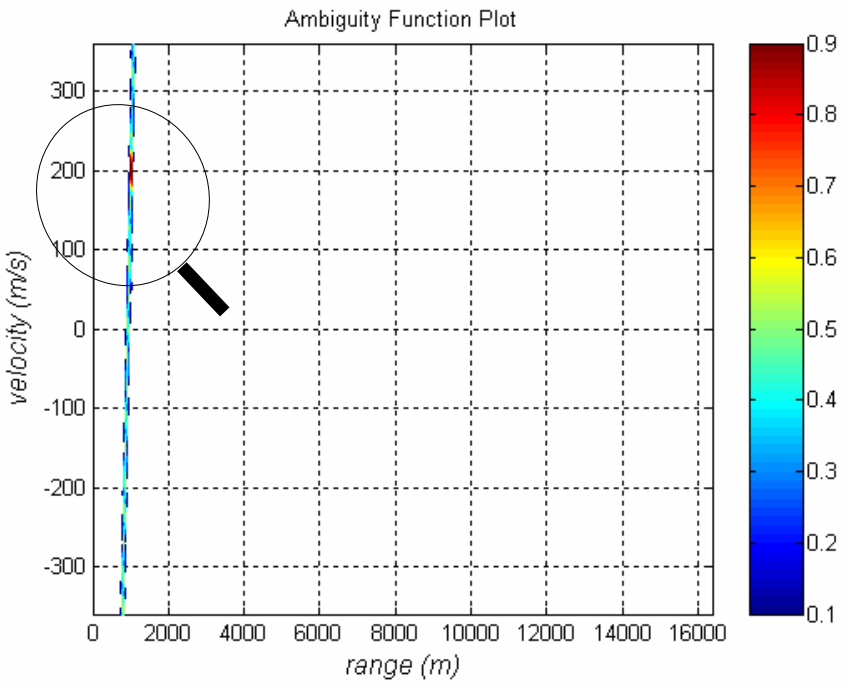

Figure 4.88: 2D Cross - Ambiguity Function plot of the transmitted and received signal for $M = 1024$ $(N_c = 1024)$ P3 code $\left(R_1 = 1000m, R_2 = 1017m, v_{1,2} = 200m/\sec., \Delta R = 16m.\right)$.

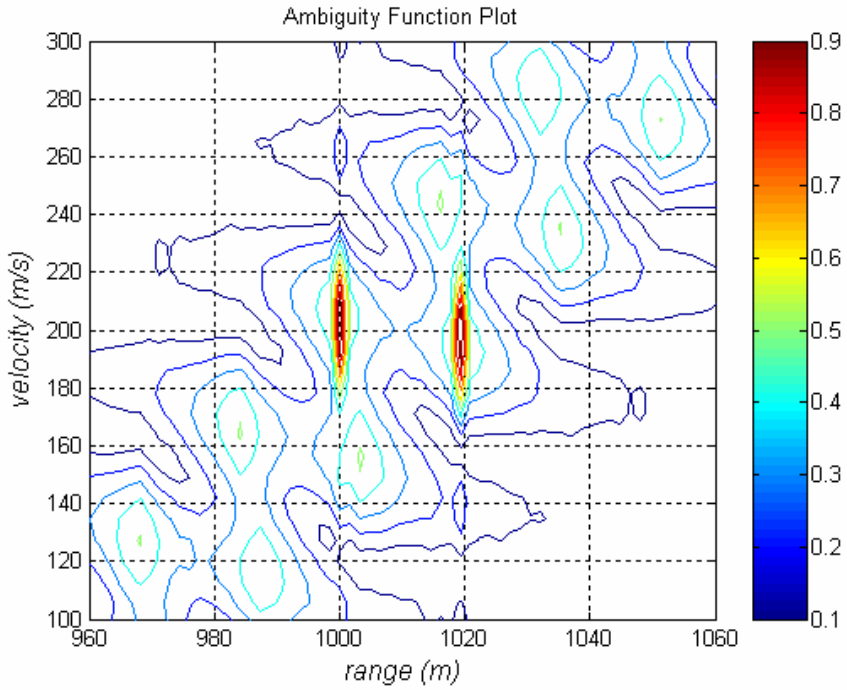

Figure 4.89: Close-up illustration of Figure 4.88.

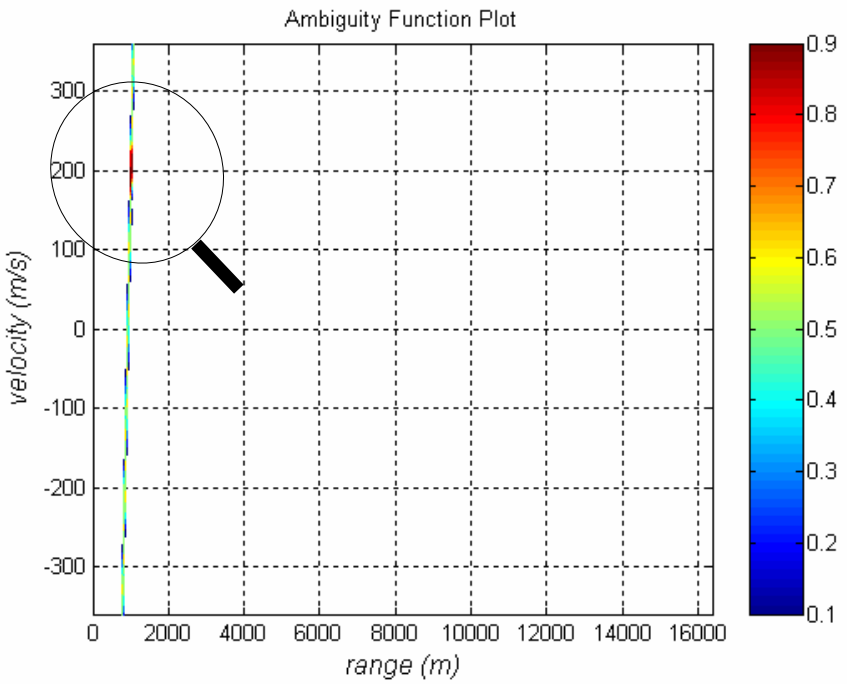

Figure 4.90: 2D Cross - Ambiguity Function plot of the transmitted and received signal for $M = 1024$ $(N_c = 1024)$ P4 code $\left(R_1 = 1000m, R_2 = 1015m, v_{1,2} = 200m/\sec., \Delta R = 16m.\right)$.

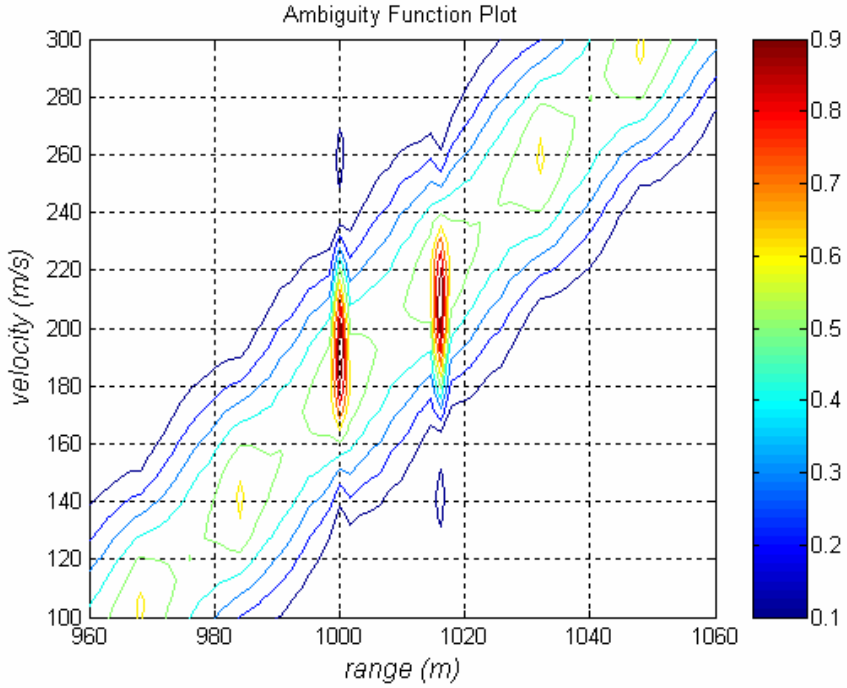

Figure 4.91: Close-up illustration of Figure 4.90.

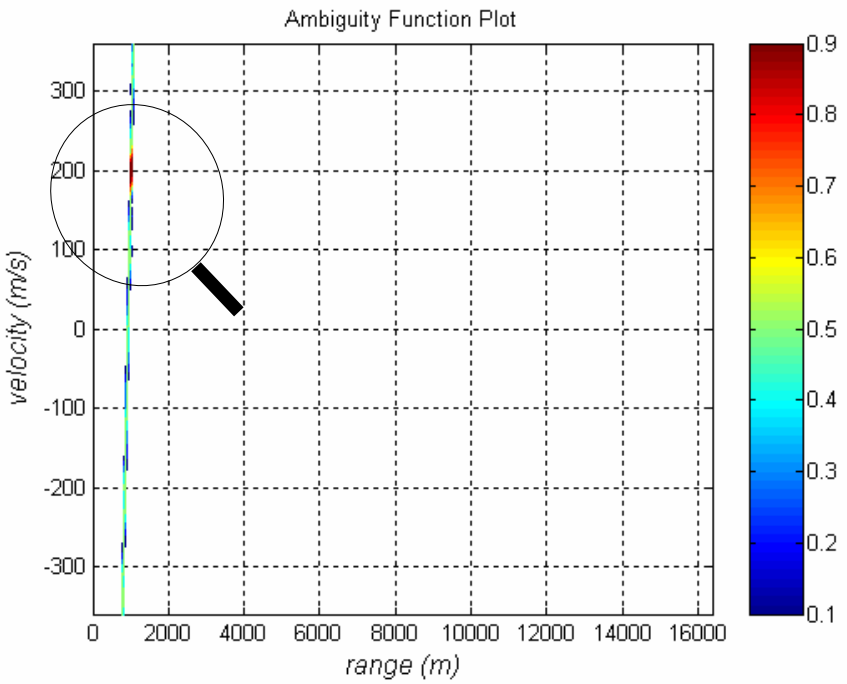

Figure 4.92: 2D Cross - Ambiguity Function plot of the transmitted and received signal for $M = 1024$ $(N_c = 1024)$ P4 code $\left(R_1 = 1000m, R_2 = 1017m, v_{1,2} = 200m/\sec., \Delta R = 16m.\right)$.

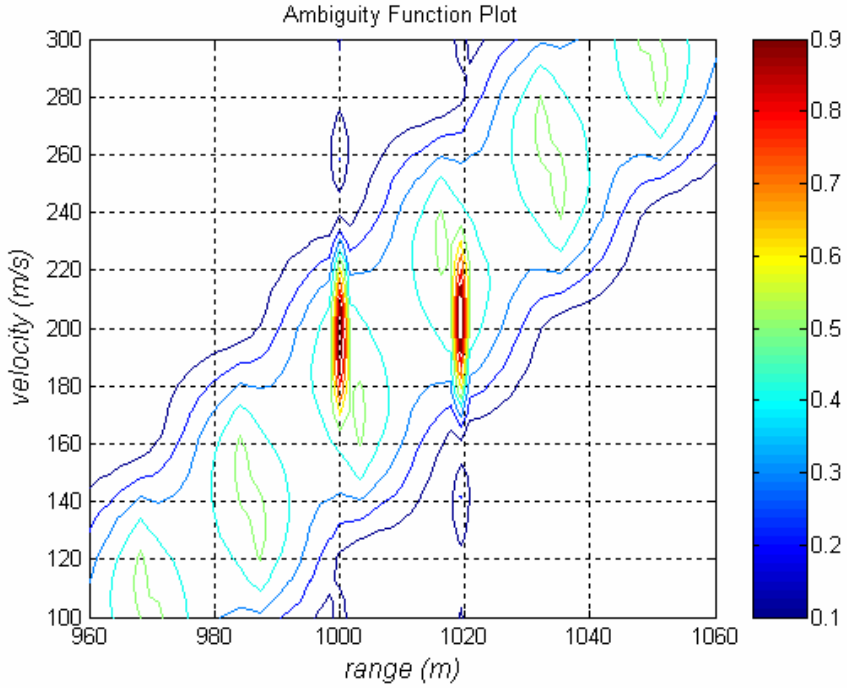

Figure 4.93: Close-up illustration of Figure 4.92.

4.6 Doppler Resolution Scenarios

In the first scenario there are two targets at 200 m/sec and 238 m/sec. Note that, the radial velocity difference between two targets is 38 m/sec. while the Doppler resolution is about 40 m/sec. That is to say, the radial velocity difference between two targets is smaller than Doppler resolution value. For better comparisons, ranges of the targets are chosen as the same value of 1000 m. The target detection results for this scenario are given in Figure 4.94, 4.95, 4.98, 4.99, 4.102, 4.103, 4.106, 4.107, 4.110, and 4.111. The targets can not be distinguished from each others. The individual velocity values can not be observed at expected values as seen in figures 4.95, 4.99, 4.103, 4.107, 4.111 for Frank, P1, P2, P3, and P4 codes respectively.

In the second scenario there are also two targets at a range of 1000m but with radial velocities of 200m/sec and 245 m/sec. Note that, the radial velocity difference between two targets is 45 m/sec. that is longer than the Doppler resolution value. The target detection results for this scenario are given in Figure 4.96, 4.97, 4.100, 4.101, 4.104, 4.105, 4.108, 4.109, 4.112, and 4.113. In this scenario case, the deviations from velocity values are much smaller than the deviation in the first scenario case. There is an improvement in velocity values with respect to velocity values in the first scenario.

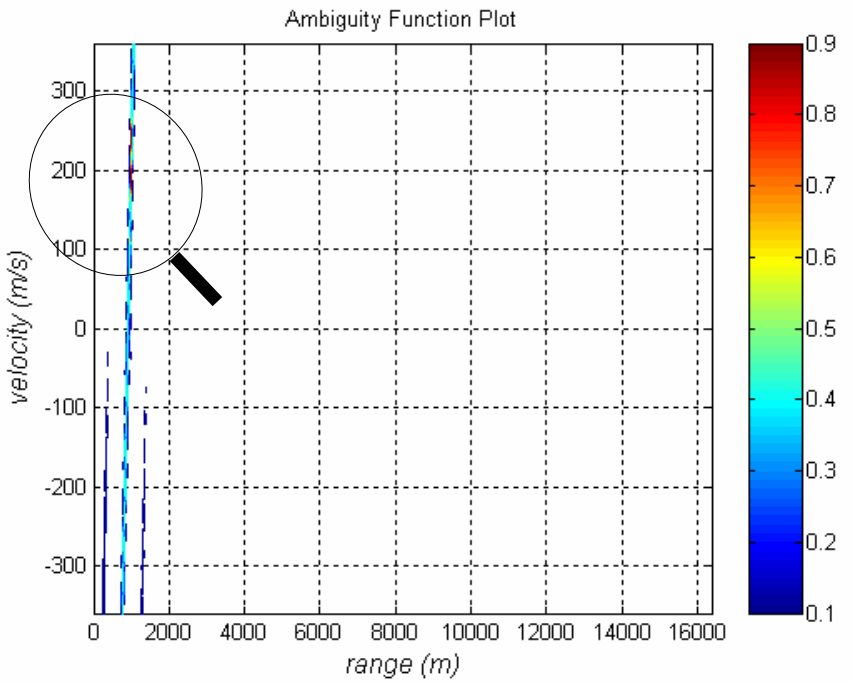

Figure 4.94: 2D Cross - Ambiguity Function plot of the transmitted and received signal for $M = 32$ $(N_c = 1024)$ Frank code $\left(R_{1,2} = 1000m, v_1 = 200m, v_2 = 238m/\sec., \Delta v \approx 40m.\right)$.

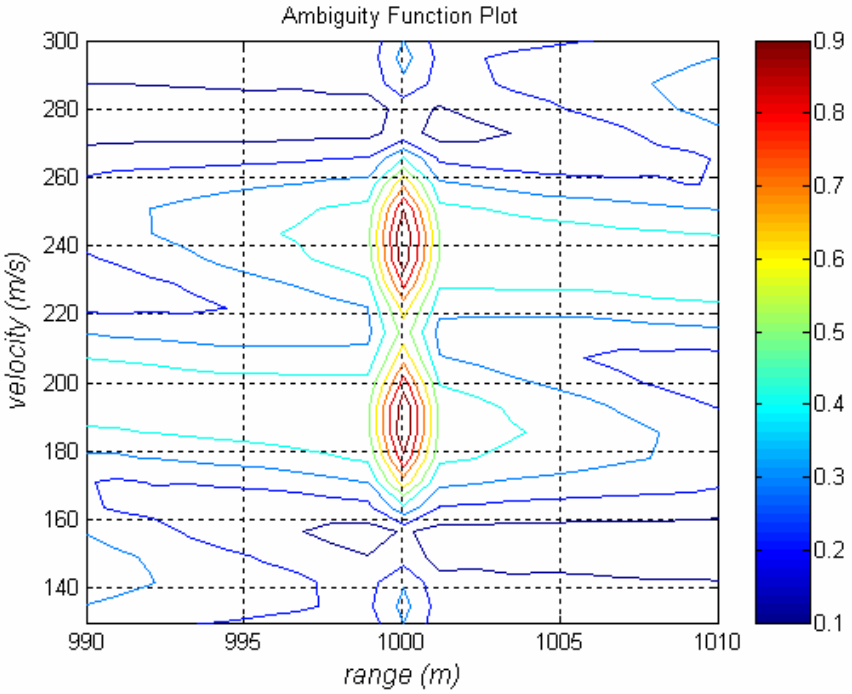

Figure 4.95: Close-up illustration of Figure 4.94.

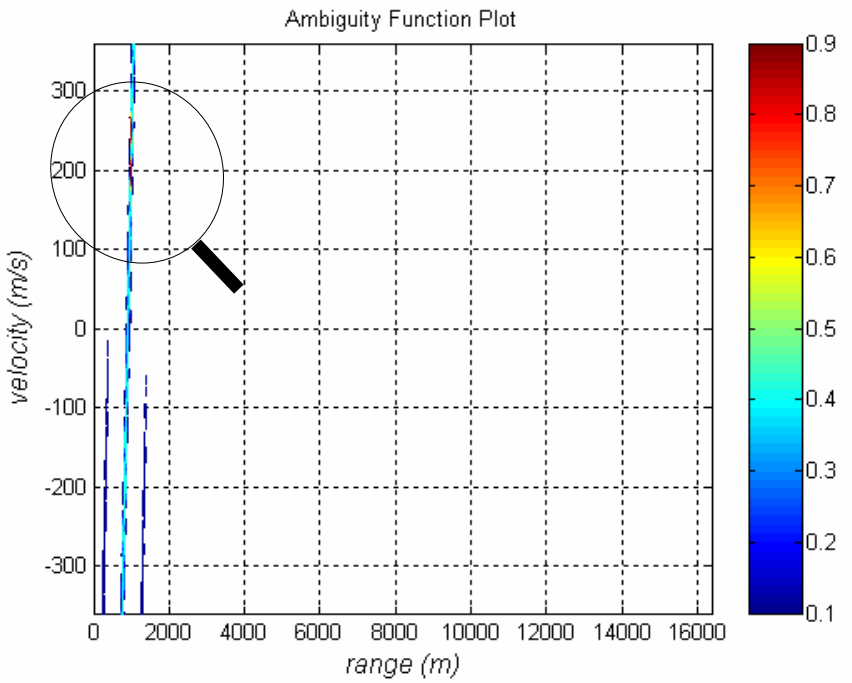

Figure 4.96: 2D Cross - Ambiguity Function plot of the transmitted and received signal for $M = 32$ $(N_c = 1024)$ Frank code $\left(R_{1,2} = 1000m, v_1 = 200m, v_2 = 245m/\sec., \Delta v \approx 40m.\right)$.

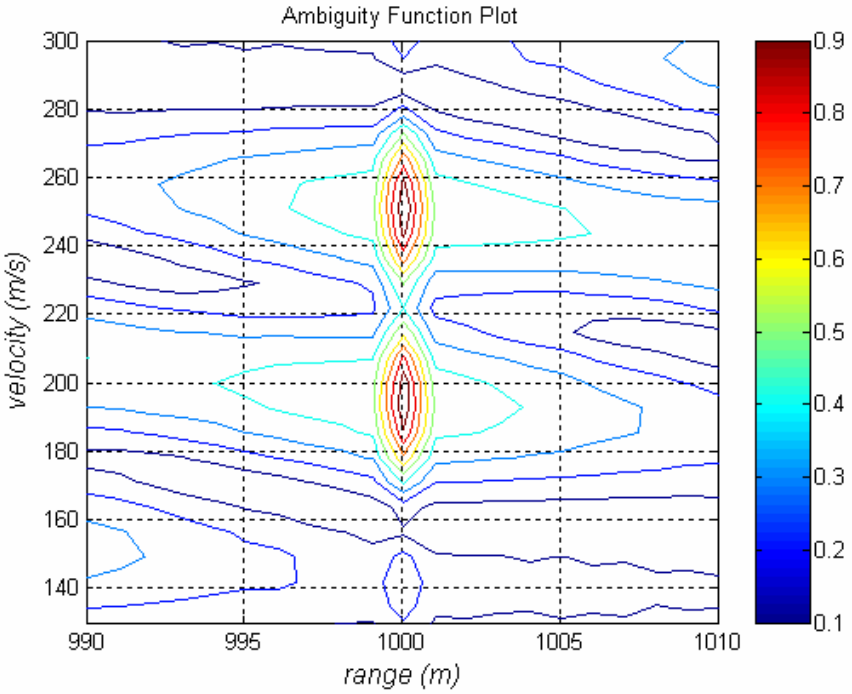

Figure 4.97: Close-up illustration of Figure 4.96.

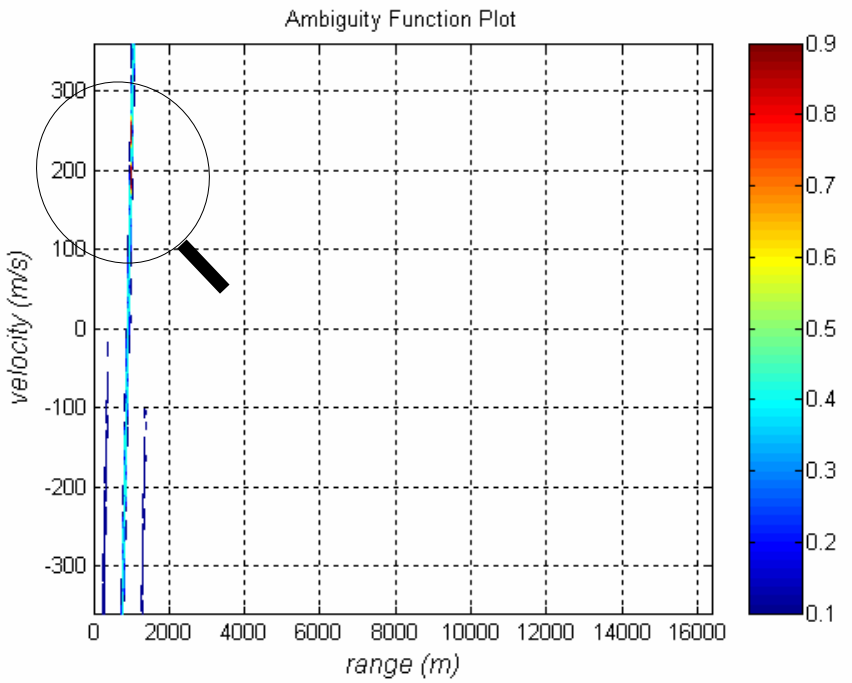

Figure 4.98: 2D Cross - Ambiguity Function plot of the transmitted and received signal for $M = 32$ $(N_c = 1024)$ P1 code

$\left(R_{1,2} = 1000m, v_1 = 200m, v_2 = 238m/\sec., \Delta v \approx 40m.\right)$.

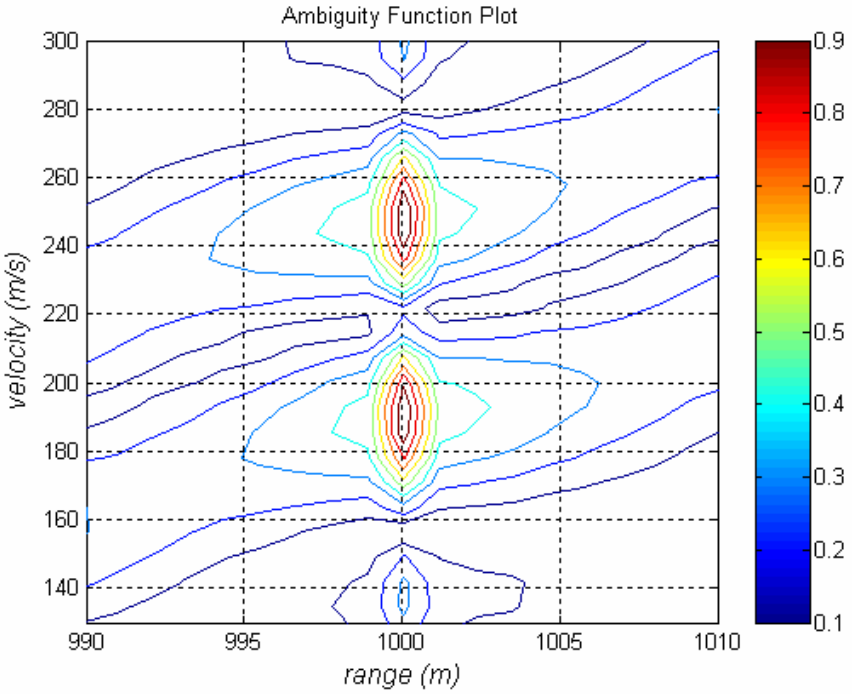

Figure 4.99: Close-up illustration of Figure 4.98.

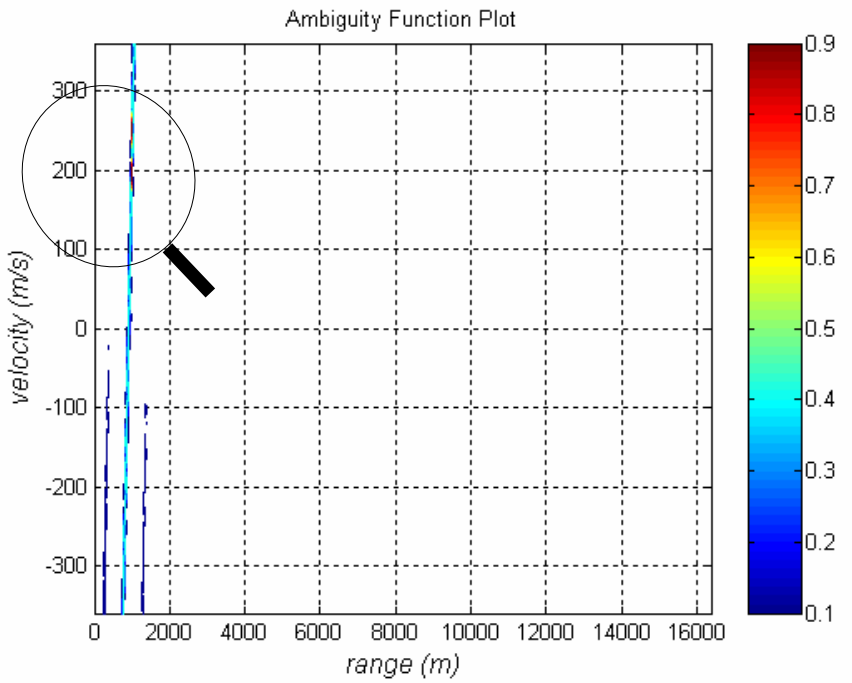

Figure 4.100: 2D Cross - Ambiguity Function plot of the transmitted and received signal for $M = 32$ $(N_c = 1024)$ P1 code

$\left(R_{1,2} = 1000m, v_1 = 200m, v_2 = 245m/\sec., \Delta v \approx 40m.\right)$

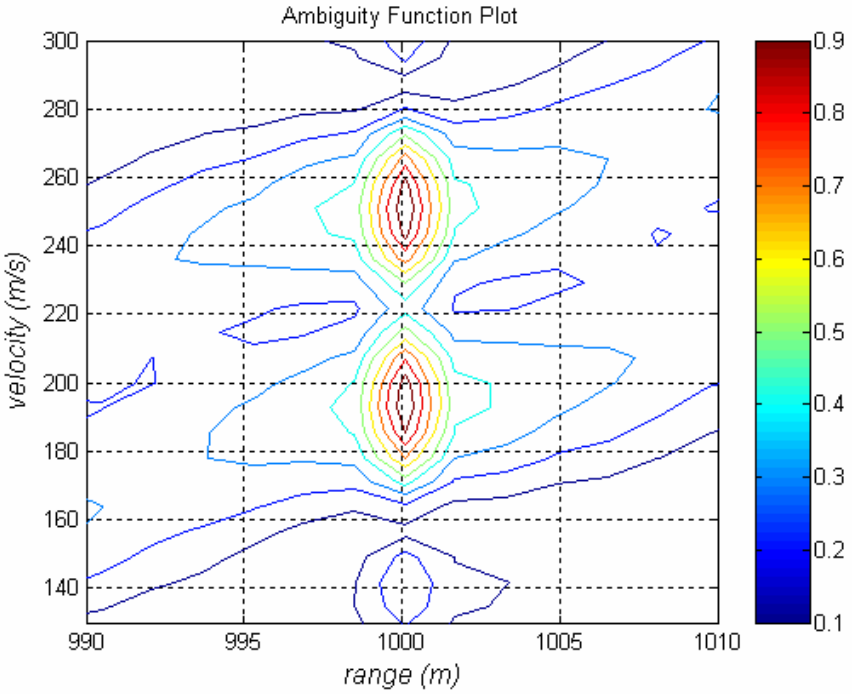

Figure 4.101: Close-up illustration of Figure 4.100.

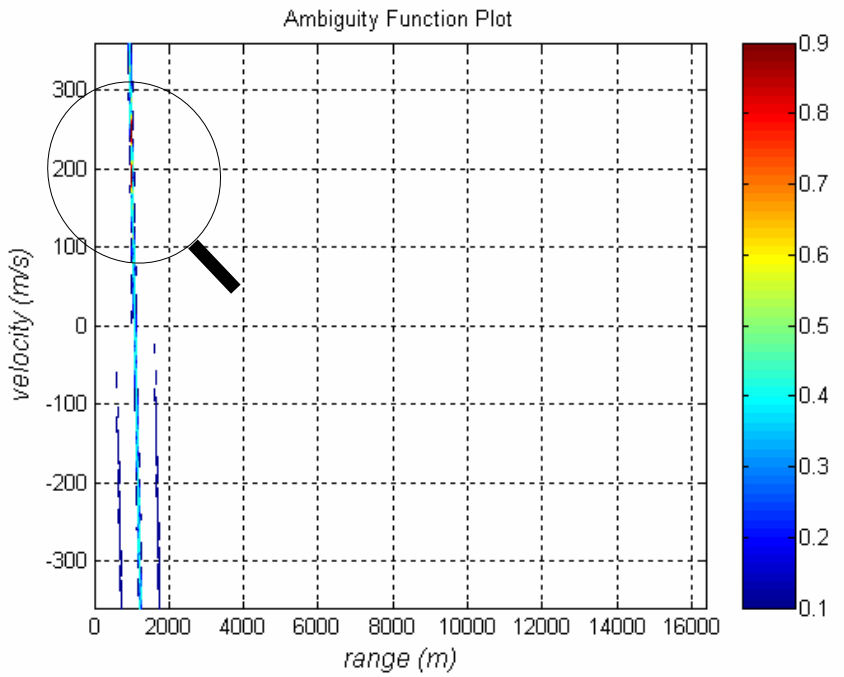

Figure 4.102: 2D Cross - Ambiguity Function plot of the transmitted and received signal for $M = 32$ $(N_c = 1024)$ P2 code $\left(R_{1,2} = 1000m, v_1 = 200m, v_2 = 238m/\sec., \Delta v \approx 40m.\right)$.

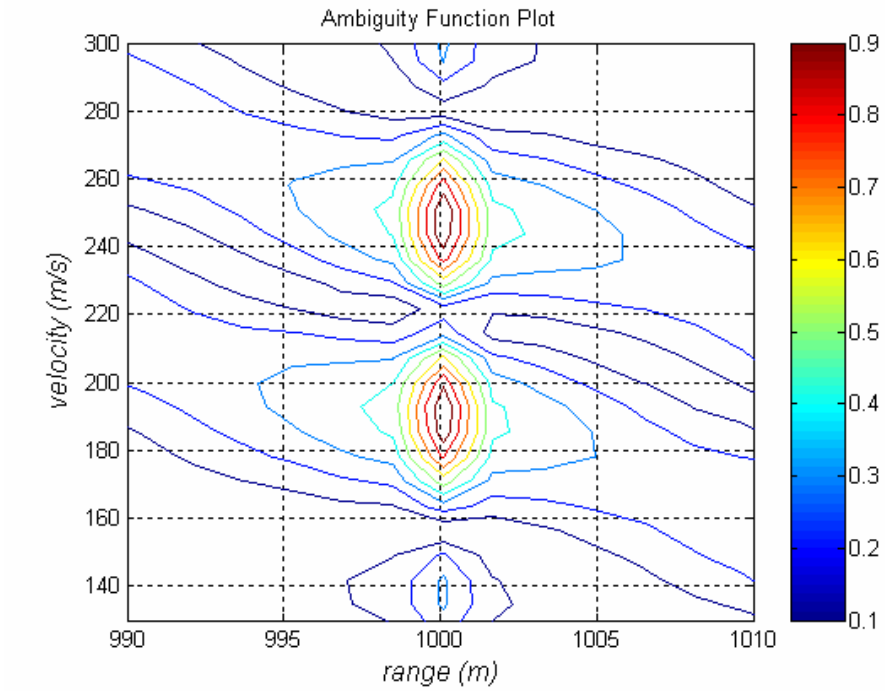

Figure 4.103: Close-up illustration of Figure 4.102.

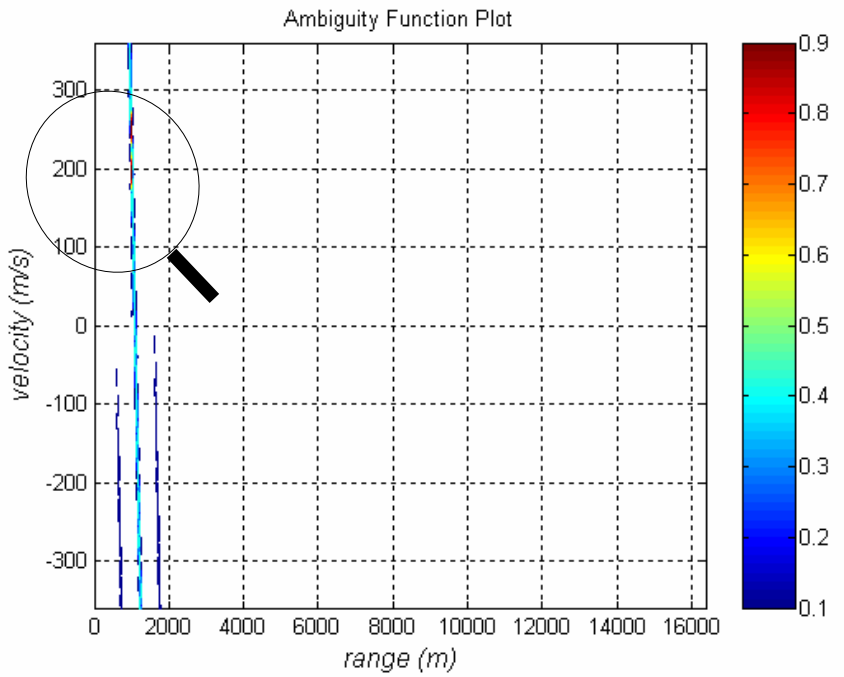

Figure 4.104: 2D Cross - Ambiguity Function plot of the transmitted and received signal for $M = 32$ $(N_c = 1024)$ P2 code $\left(R_{1,2} = 1000m, v_1 = 200m, v_2 = 245m/\sec., \Delta v \approx 40m.\right)$.

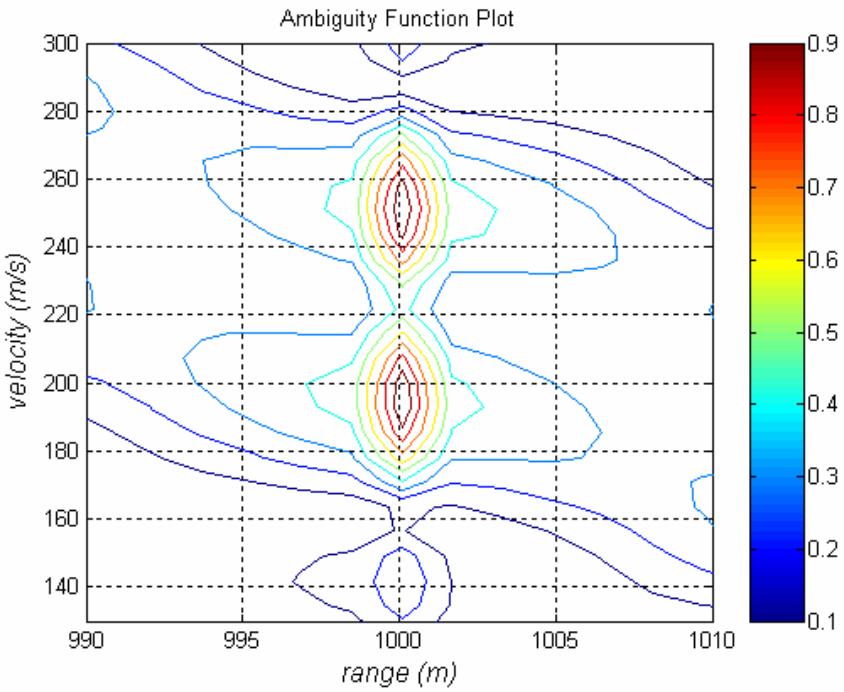

Figure 4.105: Close-up illustration of Figure 4.104.

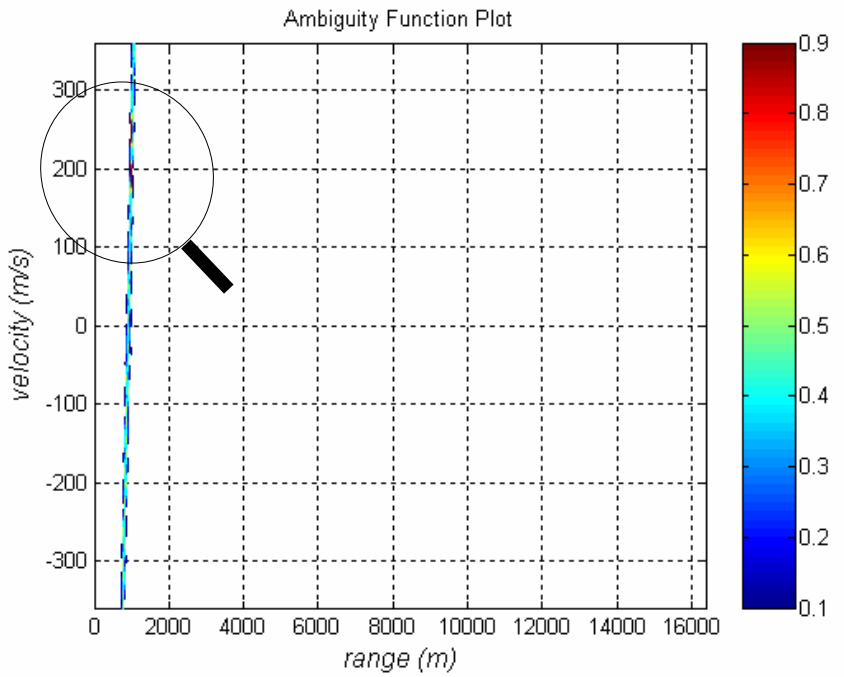

Figure 4.106: 2D Cross - Ambiguity Function plot of the transmitted and received signal for $M = 1024$ $(N_c = 1024)$ P3 code

$\left(R_{1,2} = 1000m, v_1 = 200m, v_2 = 238m/\sec., \Delta v \approx 40m.\right)$.

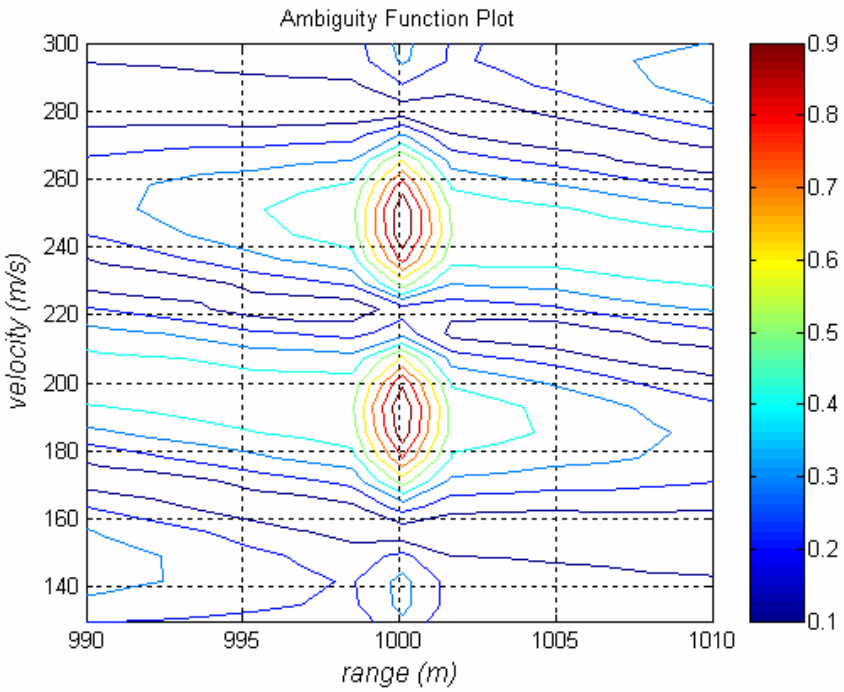

Figure 4.107 Close-up illustration of Figure 4.106.

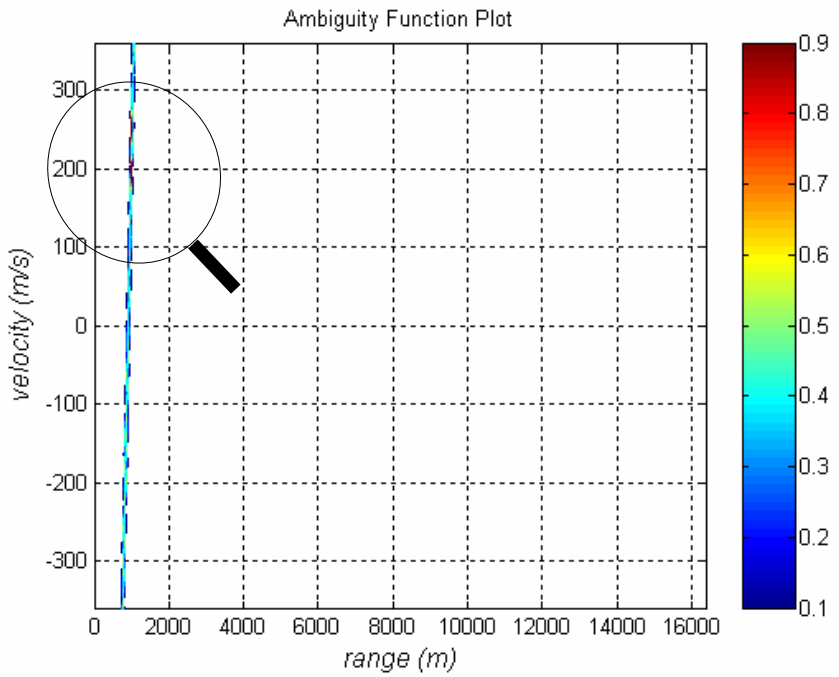

Figure 4.108: 2D Cross - Ambiguity Function plot of the transmitted and received signal for $M = 1024$ $(N_c = 1024)$ P3 code

$\left(R_{1,2} = 1000m, v_1 = 200m, v_2 = 245m/\sec., \Delta v \approx 40m.\right)$.

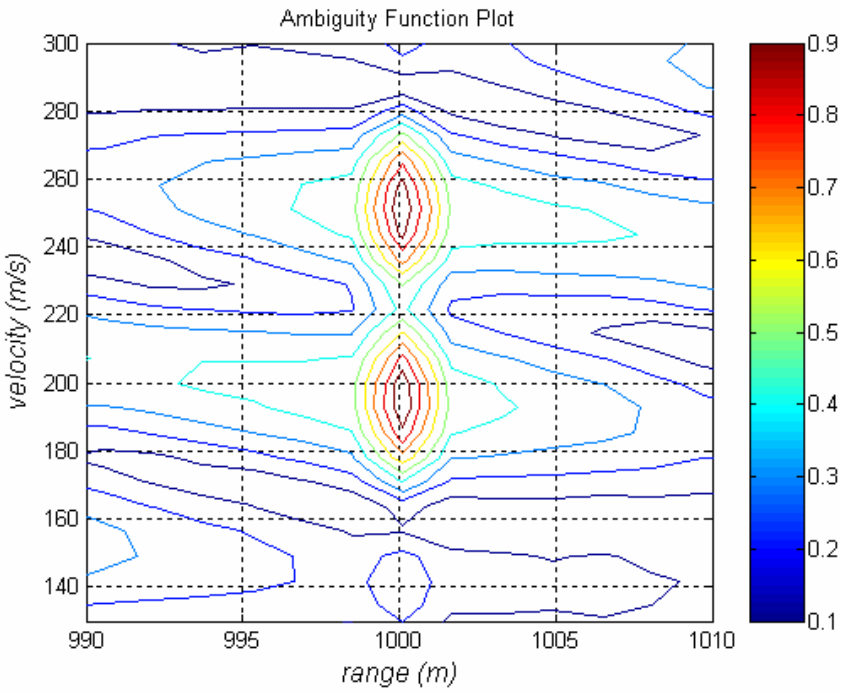

Figure 4.109 Close-up illustration of Figure 4.108.

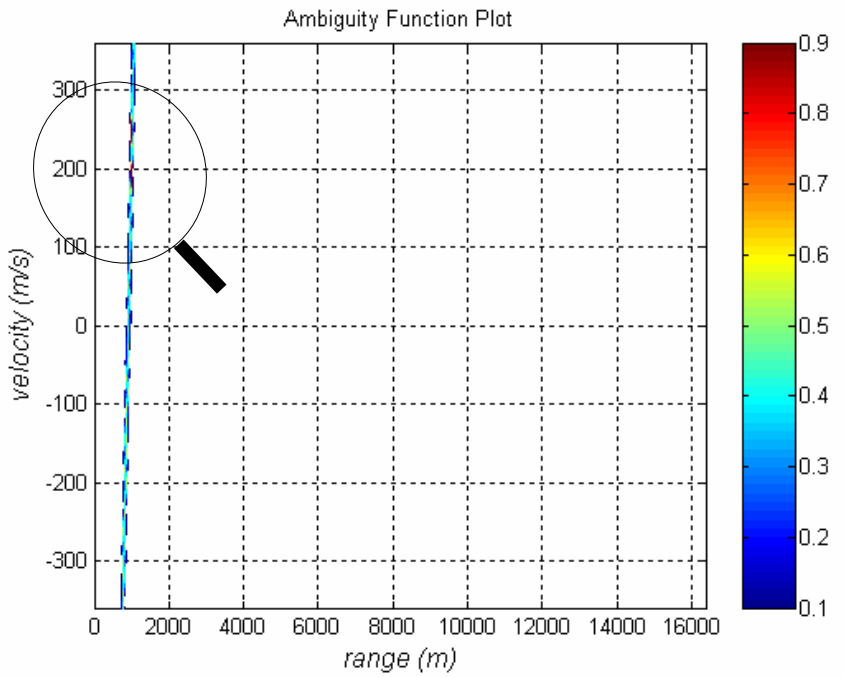

Figure 4.110: 2D Cross - Ambiguity Function plot of the transmitted and received signal for $M = 1024$ $(N_c = 1024)$ P4 code

$\left(R_{1,2} = 1000m, v_1 = 200m, v_2 = 238m/\sec., \Delta v \approx 40m.\right)$.

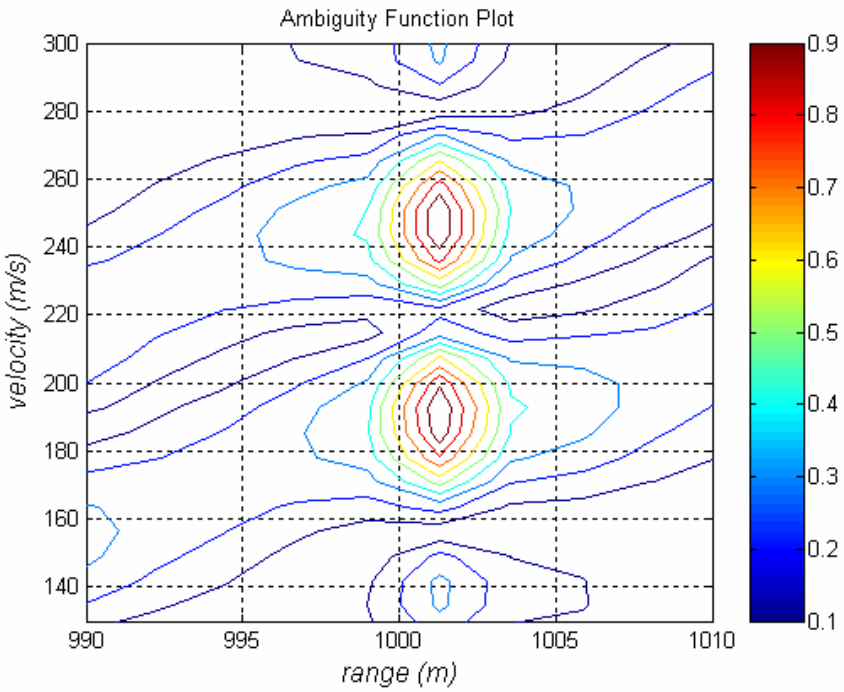

Figure 4.111 Close-up illustration of Figure 4.110.

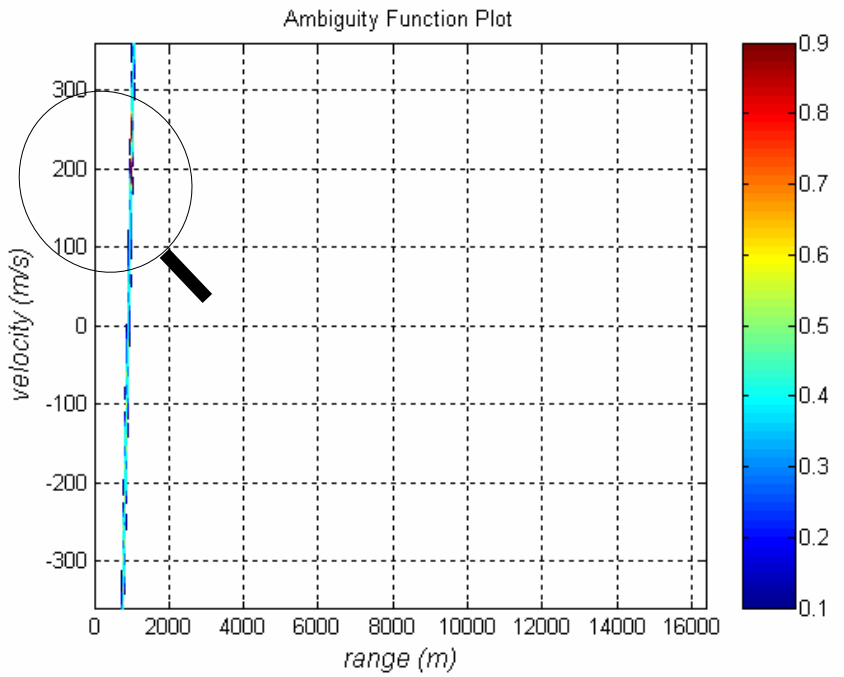

Figure 4.112: 2D Cross - Ambiguity Function plot of the transmitted and received signal for $M = 1024$ $(N_c = 1024)$ P4 code

$\left(R_{1,2} = 1000m, v_1 = 200m, v_2 = 245m/\sec., \Delta v \approx 40m.\right)$.

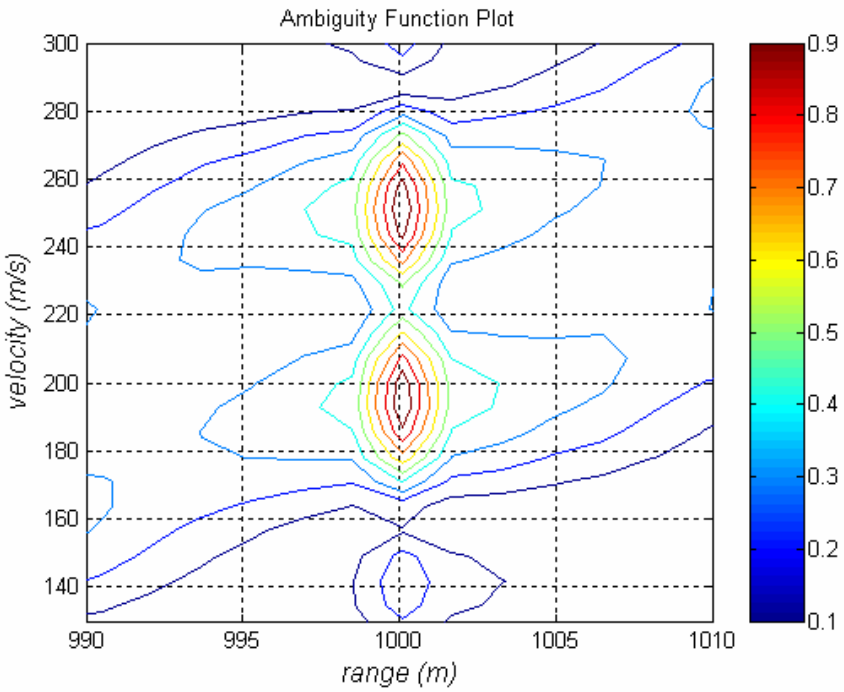

Figure 4.113 Close-up illustration of Figure 4.112.

4.7. Choosing Number of Subcodes N_c

In this section, the effect of code length on coding parameters is examined by the help of Frank code based simulations where the M parameter of the Frank code is chosen to be 16, 32 and 64, corresponding to code lengths of N_c = 256, 512 and 1024, and the simulation results for a single moving target detection for these cases are displaced at Figures 4.114 through 4.119.

Along this section, carrier frequency, subcode period, and number of code period are chosen as below, respectively:

$f_c = 35$ GHz, $t_b = 0{,}10667$ μsec., $N = 1$.

Using equations 4.1 through 4.5, Frank code parameters are obtained. These parameters are given at Table 4.1.

Table 4.1. Frank Code parameters for different M parameters

M	N_c	T (μsec.)	$R_{\text{unambiguous}}$ (m)	Δv ($m/\text{sec.}$)	ΔR (m.)
16	256	27,307	4096	156.9475	16
32	1024	109,23	16384	39.2369	16
64	4096	436,91	65536	9.8092	16

Theoretically, if code length is increased $R_{\text{unambiguous}}$ is increased, Δv is decreased that is, Doppler resolution is improved, ΔR is not changed as seen in Table 4.1 Finally, the quality of the code is increased when code length is increased.

It can be extracted from figures 4.114, 4.116, and 4.118 that unambiguous range is increased when the code length is increased ($R_{u3} \rangle R_{u2} \rangle R_{u1} = 65536 \rangle 16384 \rangle 4096$). It is clearly observed in figures 4.115, 4.117 and 4.119 that as the code length is increased further, the velocity resolution is improved. Note that, $\Delta v1$, $\Delta v2$, and $\Delta v3$ are not absolute Doppler resolution. Doppler resolutions are only proportional with $\Delta v1$, $\Delta v2$ and $\Delta v3$. If figures 4.115, 4.117, 4.119 are examined carefully, it can be seen that the accuracy level in range and velocity of the target are improved when the code length is increased.

It should be remembered that besides the unambiguous range and velocity resolution figures; the computational complexity brought by larger code lengths should also be considered as an important factor in choosing the N_c value. The optimum case seems to be the $M = 32$ case, corresponding to $N_c = 1024$ code length.

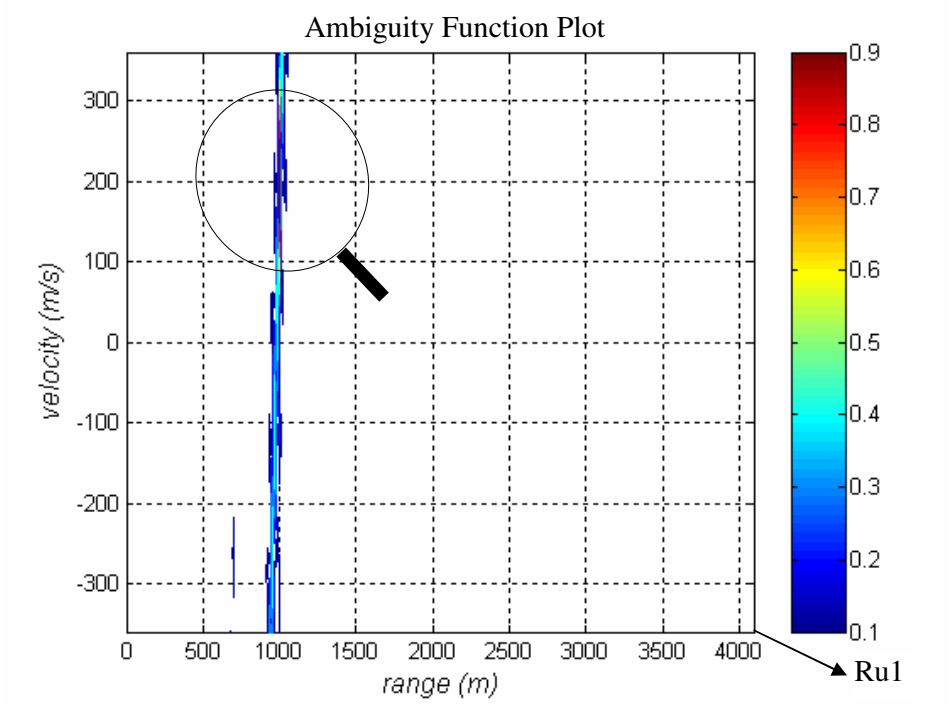

Figure 4.114: 2D Cross - Ambiguity Surface of the transmitted and received signal for $M = 16$ $(N_c = 256)$ Frank code.

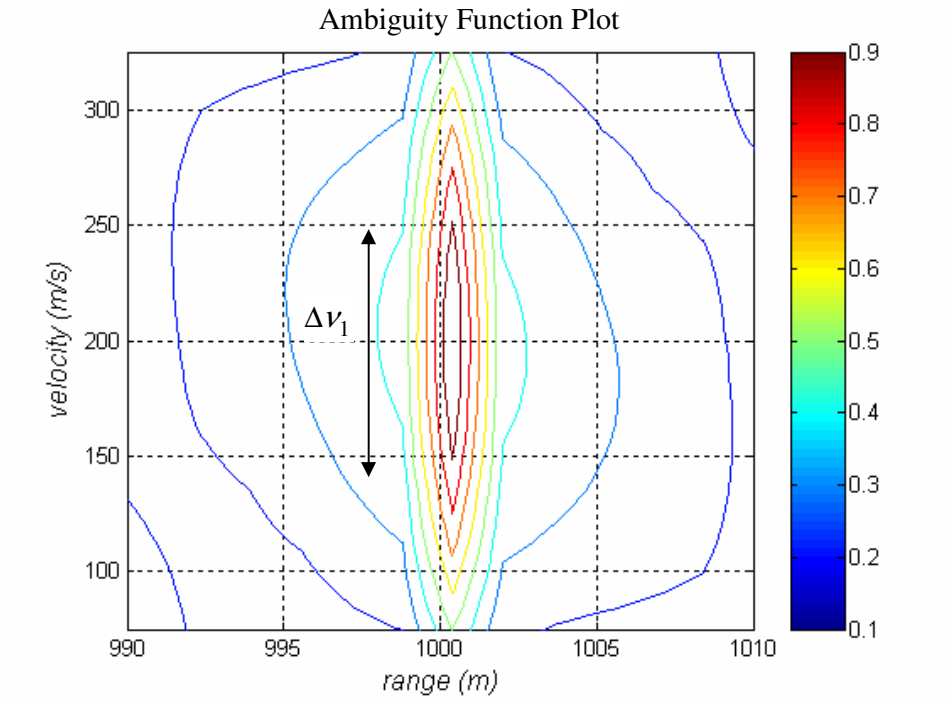

Figure 4.115 Close-up illustration of Figure 4.114.

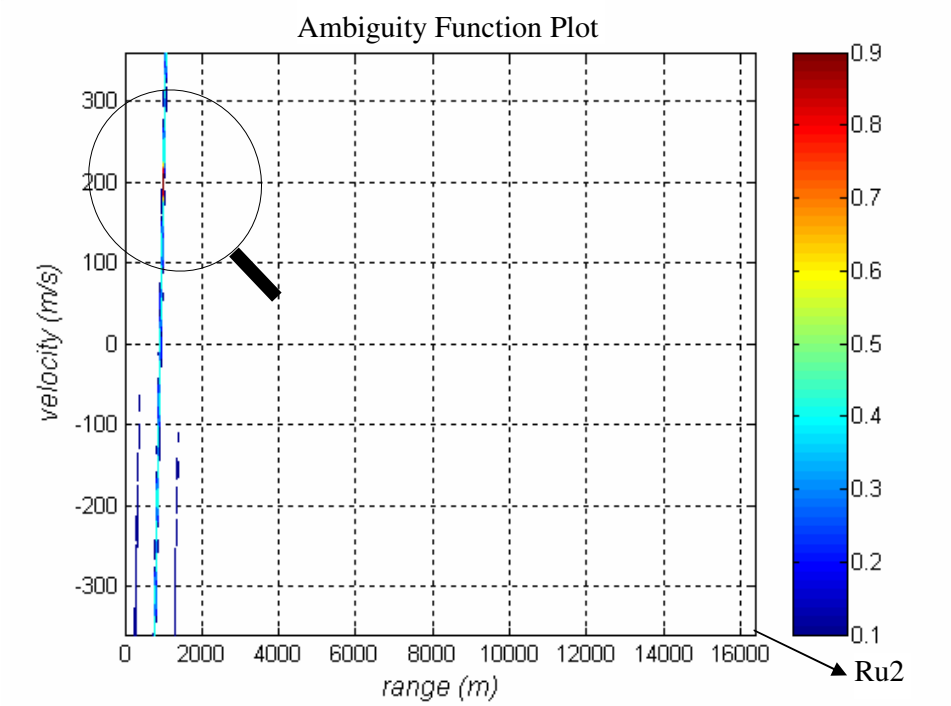

Figure 4.116: 2D Cross - Ambiguity Surface of the transmitted and received signal for $M = 32$ $(N_c = 1024)$ Frank code.

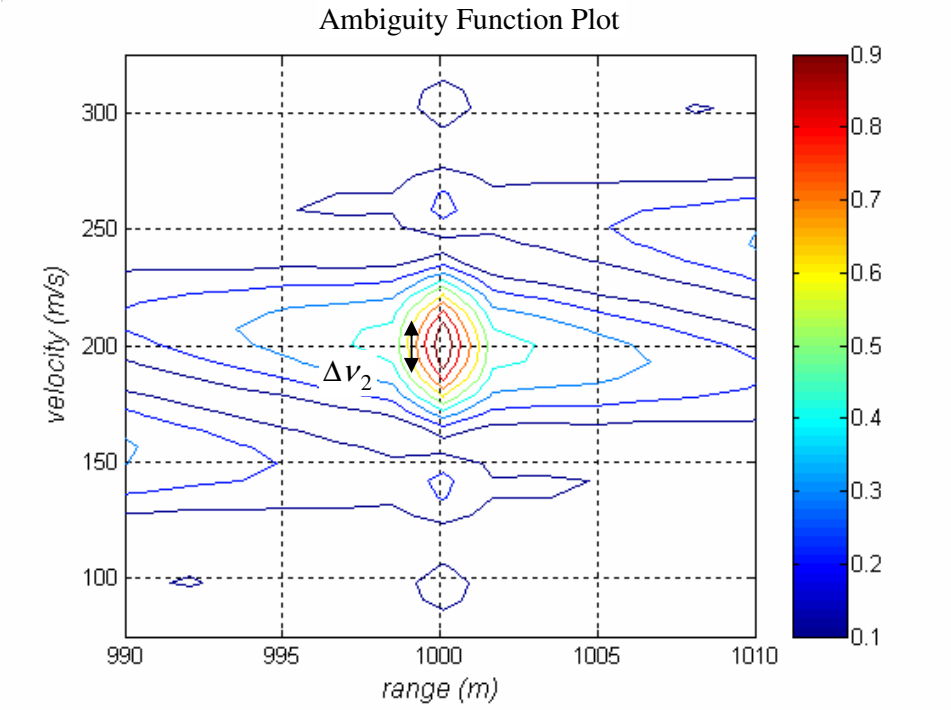

Figure 4.117 Close-up illustration of Figure 4.116.

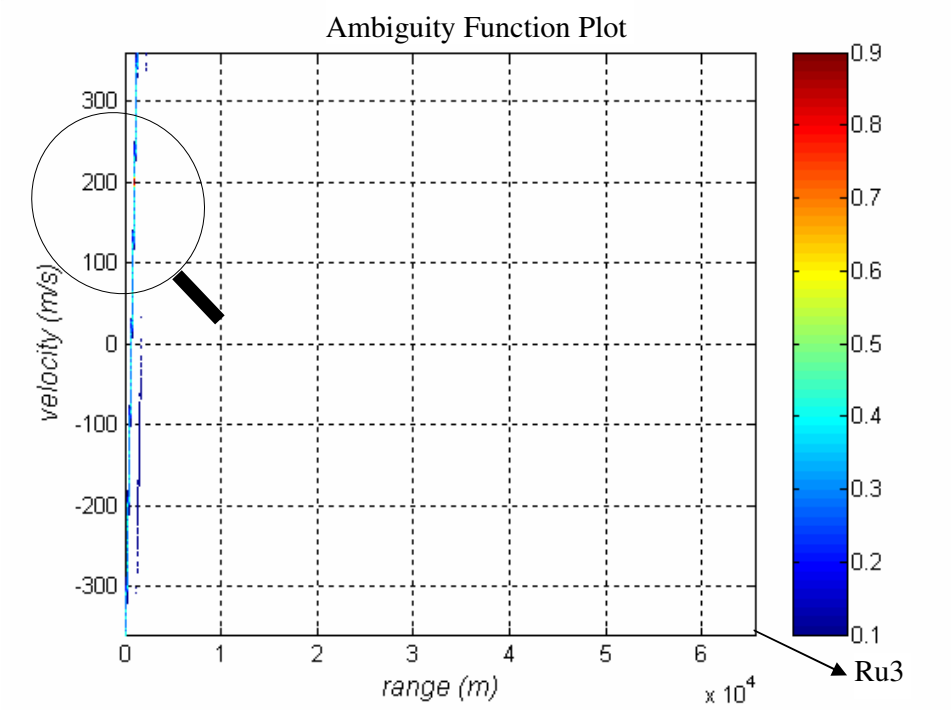

Figure 4.118: 2D Cross - Ambiguity Surface of the transmitted and received signal for $M = 64$ $(N_c = 4096)$ Frank code.

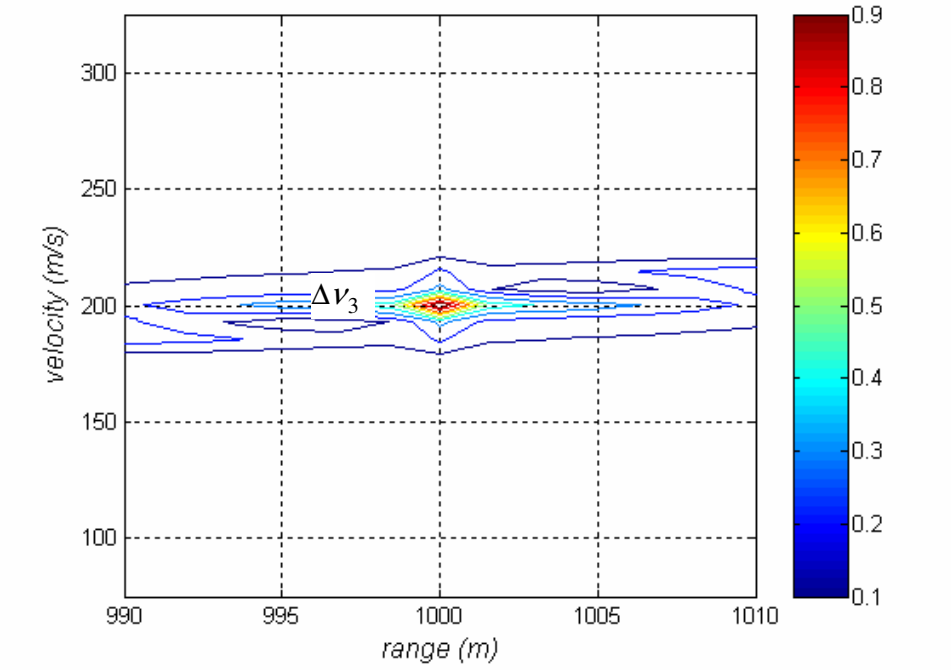

Figure 4.119 Close-up illustration of Figure 4.118.

CHAPTER V

CONCLUSION

In this thesis, phase coding techniques and use of ambiguity function for target detection in CW radars are investigated and also simulation results are presented. In order to carry out simulations, a MATLAB code is developed. Using this code several Phase Shift Keying techniques (PSK), which are the Frank, P1, P2, P3, and P4 coding techniques, are tested under different radar design parameters and target scenarios.

Phase Shift Keying (PSK) techniques are introduced with many aspects. Using MATLAB Programming Language these techniques are implemented and compared to each other. Advantages and disadvantages of the codes are discussed and explained.

Polyphase Shift Keying method is being studied as a modern concept in radar technology. However, satisfactory information about PSK techniques for target detection is not found in the literature. In general, spread spectrum signals carry mass amount of information due to their wide band nature. The more information carried by the signal the more detail the radar signal processor obtains. This means that more accurate range and velocity information can be gathered by the wide band signals in radar systems. Digital techniques are utilized to generate and decode polyphase signals so the code structure and corresponding matched filter can be altered easily and rapidly. Former versions of spread spectrum radars have been utilizing FMCW technique which is an analog approach to pulse compression applications. Polyphase codes are usually generated by the approach of

approximating the phase progression to the quadratic phase of FMCW waveform, in a digital manner. Also, coded radar waveforms which are wideband-long duration signals, introduce a high processing gain due to their high time-bandwidth product. Therefore such signals can be transmitted with a very low peak power and become less vulnerable to interception and jamming. Such radars are called Low Probability of Intercept (LPI) radars.

In the simulations of this thesis, range and Doppler information of the targets can be extracted successfully for various scenarios. Due to the simulation results, targets are localized precisely on the range-radial velocity plane through cross ambiguity analysis for all used polyphase codes (Frank, P1, P2, P3, and P4 codes). No significant performance difference is observed between these codes from conducted simulations except that the side lobe levels of the Frank, P1 and P2 codes are smaller than the side lobe levels of the P3 and P4 codes.

Auto ambiguity function is useful for analyzing a designed code structure in the range versus radial velocity plane in terms of side lobe levels, range resolution and Doppler resolution. In other words, auto ambiguity analysis quantizes the quality of the designed code. On the other hand, cross ambiguity function is utilized for target detection purposes. Cross ambiguity function is calculated by cross correlating the received signal by a collection of frequency and time shifted versions of the transmitted waveform. The result is a surface, lying above the range-radial velocity plane. This surface has peak values at the points which characterize the targets' range and Doppler profile.

In this thesis, target detection simulations are carried out in MATLAB platform for single and multiple target scenarios for different ranges and radial velocities. It is observed that the targets can be indeed located precisely on the range-radial velocity plane. Then, the range and velocity resolutions obtained as simulation outputs compared with theoretically expected values. Very good agreement is achieved in that respect also. These simulations are then repeated for noisy received signals to be more realistic. Our target detection simulations have shown that even at very low SNR values, such as SNR = -20 dB, the detection performance is still satisfactory. Since the noise energy is spread all over the range-radial velocity plane and

received signal energy is concentrated in a narrow region, the detection of the targets was quite successful.

Finally, the effect of a critical design parameter, the code length on the range and velocity resolutions, is investigated through simulations. The results are valid for all polyphase codes, so only the Frank code is examined for the sake of brevity. Any increase in the code length leads to improvement in the maximum unambiguous range, Doppler resolution and processing gain. In other word, $R_{unambiguous}$ increases, Δv decreases and the processing gain increases by increasing code length. Since the reciprocal of the signal duration is equal to Doppler resolution, longer codes can resolve the velocity better. Since the processing gain is increased, the robustness of the code against receiver noise is improved. However, increasing the code length, the computational complexity dramatically increases. In this thesis a code length of 1024 bits is selected to be the best choice. This is due to the limitations on the computational capacity of the computer used.

The cross ambiguity method is very demanding for computational power. Operations on large signal matrices make the cross ambiguity function hard to compute and require very large memory. For this technique to be practically applicable in tactical electronic warfare arena, very powerful digital signal processing hardware should be available. Cross ambiguity function is a rather raw representation of target range and velocity information. As a future work for autonomous target detection and tracking issues, the cross ambiguity diagram can be analyzed through pattern recognition and other feature extraction techniques.

REFERENCES

[1] Bassem R. Mahafza, Ph. D., *Radar Systems Analysis and Design Using MATLAB*, Chapman & Hall/Crc, 2000.

[2] Skolnik, M., *Introduction to Radar Systems, 3rd Edition*, McGraw Hill, Boston, 2001.

[3] Levanon, N., *Radar Principles*, John Wiley & Sons, New York, 1988.

[4] Phillip E. Pace, *Detecting and Classifying Low Probability of Intercept Radar*, 1.st Edition Artech House, 2004.

[5] Nadav Levanon, Eli Mozeson, "Radar Signals", 1.st Editon Wilet-Interscience, 2004.

[6] Victor C. Chen, Hao Ling, *Time-Frequency Transforms for Radar Imaging and Signal Analysis*, Artech House, 2002.

[7] Nathanson Fred E., *Radar Design Principles*, McGraw-Hill, 1990.

[8] Hlawatsch F., and Boudreaux-Bartels G.F. , "Linear and Quadratic Time-Frequency Signal Representations", IEEE Signal Processing Magazine, pp. 32-35, Apr. 1992.

[9] Levanon, N., and Freedman, A., "Periodic Ambiguity Function of CW Signals with Perfect Periodic Autocorrelation", IEEE Transactions on Aerospace and Electronic Systems, Vol. 28, No. 2, pp. 387-395, April 1992.

[10] Getz, B., and Levanon, N, "Weight Effects on the Periodic Ambiguity Function", IEEE Transactions on Aerospace and Electronic Systems, Vol. 31, No. 1, pp. 182-193, April 1995.

[11] Levanon, N., and Freedman, A., "Properties of the Periodic Ambiguity Function", IEEE Transactions on Aerospace and Electronic Systems, Vol. 30, No. 3, pp. 938-941, July 1994.

[12] Personal notes of Professor Gönül Turhan Sayan, April 2005.

[13] Barker, R. H., "Group synchronizing of binary digital systems in communications theory", Butterworth, London, pp. 273-287, 1953.

[14] Schleher D. Curtis, *Electronic Warfare in the Information Age*, Artech House, 1999.

[15] Frank, R. L, "Polyphase codes with good nonperiodic correlation properties", IEEE Trans. IT-9, pp. 43 – 45, 1963.

[16] Lewis, B.L., Kretschmer, F. F., and Shelton, W.W., *Aspects of Radar Signal Processing*, Artech House Inc., Norwood, MA, 1986.

[17] Lesnik, Cz.J., Brenner. T.W., Kocanda, W.J., and Pietrasinki, J.F., "Efficient Matched Filtering of Signal with Polyphase Frank Coded Sequences", IEEE 12th International Conference on Microwaves and Radar, MIKON '98, Krakow, Poland, Vol. 3, pp. 815-819, May 20-22, 1998.

[18] Lewis, B. L., "Range-Time-Sidelobe Reduction Technique for FM-Derived Polyphase PC Codes", IEEE Trans. On Aerospace and Electronic Systems, Vol. 29, No. 3, pp. 834-840, July 1993.

[19] Painchaud, G. R., et al., "An experimental adaptive digital pulse compression subsystem for multi-function radar applications", Record of the IEEE International Radar Conference, pp. 153-158, 1990.

[20] Golomb, S.W., "Two-valued sequences with perfect periodic autocorrelation", IEEE Transactions on Aerospace and Electronic Systems, Vol. 28, No. 2, pp. 383-386, Apr. 1992.

[21] Levanon, N., “CW alternatives to the coherent pulse train – signals and processors”, IEEE Trans. On Aerospace and Electronic Systems, Vol. 29, No 1, pp. 387 – 395, April 1992.

[22] Freedman, A. and Levanon, N., “Properties of the periodic ambiguity function”, IEEE Trans. on Aerospace and Electronic Systems, Vol. 30, No. 3, pp. 938-941, July 1994.